Fall 10-1-2021

# Unravelling the Intra-Cluster Medium with Numerical Simulations and Multi-Wavelength Observations

Urmila Chadayammuri
*Yale University Graduate School of Arts and Sciences*, urmila.chadayammuri@yale.edu

Abstract

Unravelling the Intra-Cluster Medium with Numerical Simulations and Multi-Wavelength Observations

Urmila Chadayammuri
2021

Galaxy clusters are the largest virialised structures in the Universe, with gravitational potential wells so deep that, to first order, they can be described using just dark matter and dark energy. Their number density as a function of mass, called the cluster mass function (CMF), measures the growth-of-structure in the Universe. This probes cosmology in a way that is almost orthogonal from the cosmic microwave background (CMB) and type Ia supernovae (SNIa), both of which measure the geometry of the Universe instead. Combining the different methods provides tighter constraints than any one method in isolation. As we enter the era of precision cosmology, cluster cosmology is limited by uncertainties in extracting total masses from the visible properties through optical, X-ray, and radio telescopes. The uncertainty comes from our poor understanding of baryonic processes, most notably feedback from supermassive black holes (SMBH) and the behaviour of the intracluster medium (ICM) during cluster mergers. The recently launched eROSITA X-ray telescope will detect $\sim$100,000 clusters out to z $\sim$ 2, adding to our existing sample objects that were so far too small or too distant to be seen before. At smaller masses, baryonic processes are more potent relative to the gravitational potential; at higher redshifts, mergers are more common. In this thesis, I use a variety of simulations - cosmological and idealised - to deepen our understanding of the ways that these two processes affect the intra-cluster medium in different wavelengths, with an emphasis on X-ray observations, where the ICM is the brightest. I also highlight systematic errors on gravitational lensing mass measurements in merging clusters, which are relevant for ongoing and upcoming surveys such as Rubin and Roman.

The way that SMBH jets and the bulk flows from cluster mergers move through the ICM depends on plasma properties such as viscosity and thermal conduction, which in turn are affected by the presence of magnetic fields. By describing carefully the behaviour of the ICM in the absence of viscosity, conduction and magnetic fields, as well as with magnetic fields, I show which features are sensitive to plasma physics, and which are hard to distinguish from the hydrodynamic case. This work helps set the groundwork for upcoming X-ray spectroscopy missions like XRISM and Athena, which will allow us to better measure transport processes with unprecedented information about the velocity structure of the ICM.

# Unravelling the Intra-Cluster Medium with Numerical Simulations and Multi-Wavelength Observations

A Dissertation
Presented to the Faculty of the Graduate School
of
Yale University
in Candidacy for the Degree of
Doctor of Philosophy

by
Urmila Chadayammuri

Dissertation Director: Daisuke Nagai

December 2021

# Acknowledgments

This took a village.

My mother Renuka Devi set the stage with her degree in mathematics, and by establishing when I was ten that she would not ask about marriage or kids until I was done with a PhD. My sister Shalini, crushing it as a corporate lawyer, reminded me of how good I have it, and brightened my space with her paintings and books. My late father, Prakash Chadayammuri, was my hero and my biggest fan, taking me to astronomy club on the coldest Moscow nights, getting me my first Dorling Kinderseley encyclopedia even though he was broke, and helping me choose universities right before he passed away. He will always be my guiding light and ultimate role model.

Priya Natarajan took a chance on me when I wanted to return to astronomy after a dark detour into the world of investments, and for that I am eternally grateful. Paul Nulsen was my primary advisor for half of this endeavour. Keeping up with his intellect has been a challenging and extremely helpful exercise. Susan Nulsen made our office a welcoming and joyful space. John ZuHone of competence, patience and focus, always making time for my coding questions even as he juggled multiple other science projects and family. This thesis would have been absolutely impossible without them. I owe a lot to Christine Crowley, director of the Pre-Doctoral Program at the Chandra X-ray Center, who enabled me to work with such excellent people in such a supportive environment.

I was very fortunate to find amazing academic big sibs Michael Tremmel, Camille Avestruz and Grant Tremblay. They invited me to conferences, introduced me to all the right people, made sure I maintained a healthy work-life balance, and encouraged me to spend time on the teaching and equity work that are so important to me. Thank you all for tramping a trail I would really love to follow.

Most people are lucky to have one loving family; I had at least two. Annie Stutzman, Kayleigh Ryherd, Nina Gumkowski, Berk Calli, Olivia Harold, Annalisa Boerner and Victor Mutai made New Haven my second home. They are the people I can always call or write to or visit or host for any or no reason at all. They are all incredibly inspiring in their own endeavours, and truly exceptional and loving human beings. They reminded me that there is more to life than astronomy, or academia, or work, but were nevertheless loudly cheered my every achievement. Lots of love also came from Maria Feofilova, Saima Akhtar, Aria Swarr, Rebecca Trupin, Kah Yangni and so many more.

And of course, Ian. Words will never do justice to all the things you knew to do without my asking - the endless stream of cheese puffs, teas and coffee, the massages, the guitar serenades, the walks in nature, the evenings by the fire working on our respective art projects to stay sane. I draw so much strength watching you.

So to everyone who was a part of this journey - thank you, thank you, thank you.

For my father, who took me to astronomy club on the coldest of Moscow evenings. And for my mother, who always let me go.

# Contents

# List of Figures

# List of Tables

# Chapter 1

# Introduction

Galaxy clusters are the largest virialized structures in the Universe today. With masses of over $10^{14} M_{\odot}$ and hundreds to thousands of member galaxies, they represent the highest-density peaks of the Universe, sitting at the intersection of large-scale filaments as nodes of the Cosmic Web. In a $\Lambda$CDM Universe, smaller structures collapse first, and form ever larger structures by merging with one another. The story of a galaxy cluster, then, is the story of the Universe - a story of the balance between gravitational collapse, Hubble expansion and, at later times, acceleration by dark energy. Most of a cluster's mass is dark, and most of the baryonic mass is in the diffuse intracluster medium (ICM); only about $3\%$ of the cluster mass lies in galaxies. Star formation and stellar feedback, whose energy can be comparable to the binding energy of an individual galaxy, are negligible compared to the gravitational potential of the cluster. Cluster cosmology until fairly recently has relied on the relative unimportance of baryonic processes, and treated the baryons simply as observable tracers of the total gravitational potential, dominated by the dark matter. Cluster cosmology and cluster astrophysics, therefore, have remained slightly distinct areas of research.

Over the course of my PhD, I have investigated several questions that complicate this simple model. In this introduction, I lay out a fuller exposition of the problems at hand, and the tools I used to address them. Section 1.1 introduces the standard model of cosmology today, $\Lambda$CDM, and how we understand the formation of cosmic structure. Section 1.3.1 describes how optical, sub-millimeter, radio, gravitational lensing and X-ray observations probe different components of galaxy clusters, and how these relate to each other. Section 1.2 explains the basic principles of numerical simulations, and the role of cosmological as well as idealised simulations in understanding galaxy clusters. Section 1.3 puts together our understanding of structure formation, observations, and simulations to summarise the role of galaxy clusters in studying cosmology and astrophysics. Having set this groundwork, I then outline the specific focus of this thesis in Section 1.4 - understanding the role of AGN, mergers, and magnetic fields in the evolution of galaxy clusters, and their implications for

cluster cosmology.

## 1.1 Structure formation in the ΛCDM Universe

The dominant cosmological paradigm is ΛCDM, where the energy budget of the Universe is dominated by dark energy, assumed to be a cosmological constant $\Lambda$, and cold dark matter. We know extremely little about the nature of dark energy, and only slightly more about dark matter. What we do know is that the dark energy is a repulsive force that has been accelerating the expansion of the Universe since $z \sim 0.2$, and that the dark matter interacts with standard model particles only via gravity. The "cold" refers to the fact that the dark matter particle must be quite massive, and have therefore have a low thermal velocity when it first decouples from the photon-baryon fluid in the early Universe. If it were warmer, i.e., composed of lighter particles like neutrinos, its thermal velocity in the early Universe would have been large enough to counter the gravitational potential in locally overdense regions. As a result, structure would have formed much more slowly, and today, we would see many fewer galaxies, groups and clusters. The cosmological constant is the energy density of a vacuum, added to Einstein's field equations:

$$G_{\mu\nu} = R_{\mu\nu} - \frac{1}{2}Rg_{\mu\nu} = \frac{8\pi G}{c^4}T_{\mu\nu} - \Lambda g_{\mu\nu} \tag{1.1}$$

where $R_{\mu\nu}$ is the Ricci curvature tensor, $R = g^{\mu\nu}R_{\mu\nu}$ the Ricci scalar, $g_{\mu\nu}$ the spacetime metric and $T_{\mu\nu}$ the stress-energy tensor, consisting of the mass and momenta in each of three orthogonal directions. This means that in an empty Universe, where the stress-energy tensor is 0, the cosmological constant means a negative curvature. All observations so far point to a flat Universe, i.e., curvature 0.

The theory of inflation predicts that by the end of the inflationary epoch, the Universe would be seeded with Gaussian density fluctuations with a mean *overdensity* of 0; this means that some regions would be more dense than average, and some less. The denser regions attract more matter towards them, while Hubble expansion, radiative pressure and, at late times, dark energy, all act to stretch the Universe out in all directions. Structure formation is therefore a competition between these attractive and repulsive forces. The formation of collapsed halos can be modeled analytically, as in the case of the Extended Press-Schechter (EPS) formalism (Press & Schechter, 1974; Bond et al., 1991; Lacey & Cole, 1993; Mo & White, 1996). While extremely powerful, these analytical models do make simplifying assumptions - such as the spherical symmetry of the initial perturbations - and the results are sensitive to the choice of the filter functions used to smooth the fluctuations (Schneider et al., 2013). Most notably, they are unable to incorporate the non-linear effects of baryons, which are ultimately the observable component that can be used to test any given cosmology. Advances in computing and algorithms have enabled us

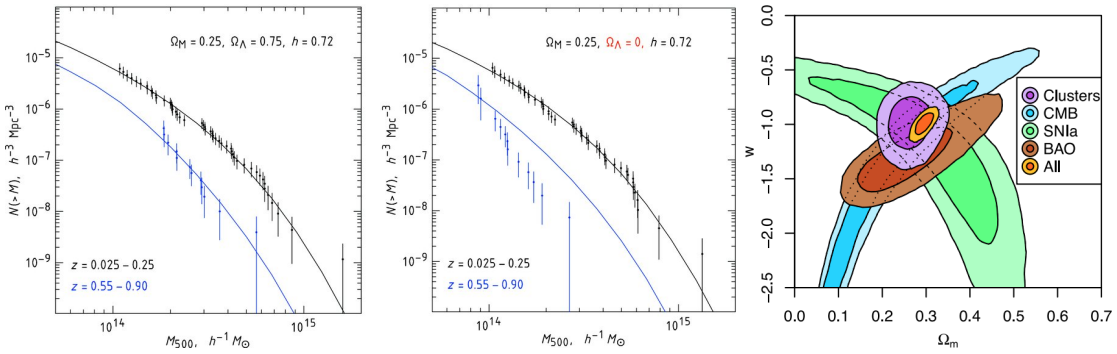


Figure 1.1: *Left:* The number density of galaxy clusters as a function of their $M_{500}$ at low (black) and high (blue) redshifts, as measured in Vikhlinin et al. (2009b). The lines in the left panel show the fit for the $\Lambda CDM$ cosmology, whereas the middle panel shows the fit for $\Omega_m = 1$. The latter is clearly ruled out by the high-redshift sample. *Right*: Joint constraints on the dark energy parameter of state $w$ and the dark matter density $\Omega_m$ from Mantz et al. (2015). CMB measures the Universe as it was at the surface of last scattering, z $\sim$ 1100. SNIa use the geometry of the Universe, by measuring the luminosity distance as a function of cosmic time. Galaxy clusters are growth-of-structure measurements, tracing the rate at which structure forms via gravitational collapse against the Hubble flow and dark energy acceleration. Using these complementary methods yields much tighter joint constraints.

to study the formation and evolution of galaxy clusters from first principles, starting with initial conditions from linear theory and evolving the system in time numerically. Such "cosmological simulations" have allowed to study structure formation self-consistently. Further, these form a backbone onto which we can add models for how baryons evolve in the Universe, from an almost uniform gas at very early times, to multiphase gas in galaxy-level halos, to stars and black holes and the energetic feedback from each of them.

## 1.2 Numerical simulations of large-scale structure

Astrophysical simulations all have the same basic ingredients - initial conditions, a gravity solver, a hydrodynamic solver, and sub-grid models for unresolved baryonic processes.

### 1.2.1 Initial conditions and gravity solvers

The simulation volume is initialised with pre-defined density distribution - in the case of a cosmological simulation, this is usually a Gaussian random field in the very early Universe, as described by the power spectrum in wavenumber-space:

$$P(k) =< \tilde{\delta_k}\tilde{\delta_k^*} >, \tag{1.2}$$

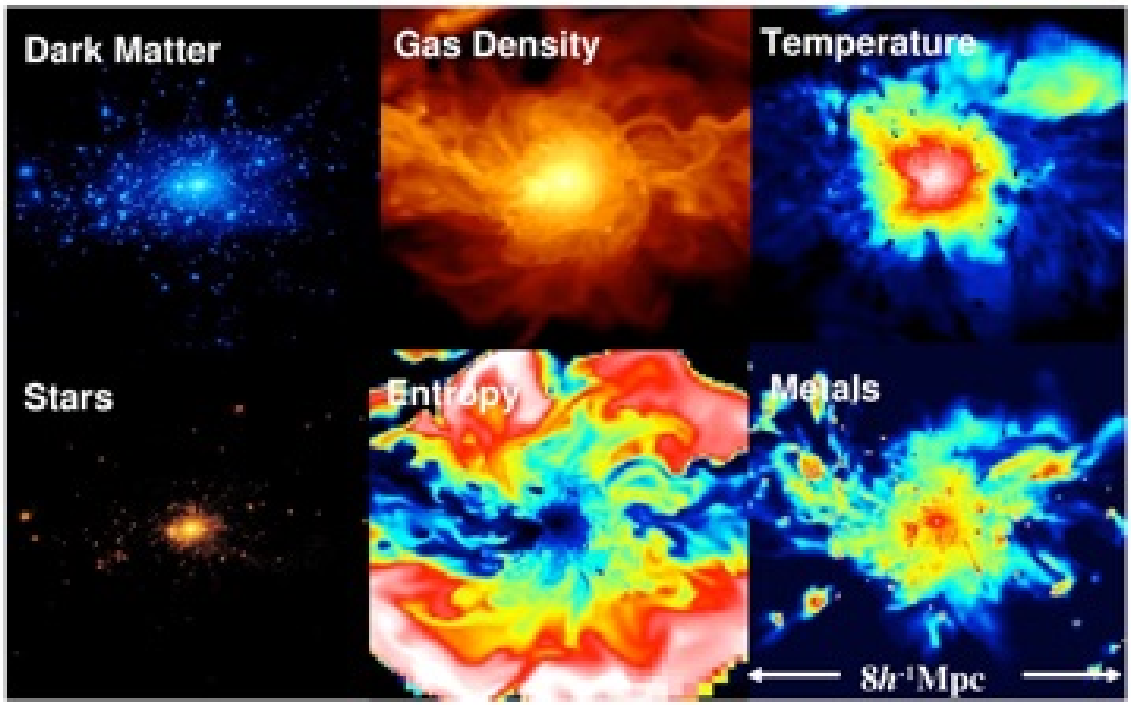


Figure 1.2: An example of the various properties that are evolved simultaneously in cosmological simulations performed using the ART hydodynamical cosmological simulation code (Nagai et al., 2007b). While the dark matter (top left) is not directly visible, it affects the distribution of gas (X-ray and SZ), stars (optical and IR) and metals (optical, UV and X-ray spectroscopy) which can be measured by a variety of telescopes.

where the tilde indicates that each $\delta$ is the Fourier transform of the overdensity in physical space $\vec{x}$. For mathematical convenience, the initial conditions are usually generated in k-space, then translated into physical space by inverse Fourier transform (Hahn & Abel, 2011), where $M$ is the total mass, and $a$ the scale radius.

The simulation box now has a density defined at every point. Next, we solve for gravity, which for a collisionless N-body system is described by the Vlasov-Poisson equations:

$$\frac{d\vec{x_i}}{dt} = \vec{v_i}; \tag{1.3}$$

$$\frac{d\vec{v_i}}{dt} = - \bigtriangledown_x \phi; \tag{1.4}$$

$$\Delta_x \phi = -4\pi G\rho \tag{1.5}$$

Numerical algorithms like the highly popular TreePM (Bagla, 2002) have made it much easier and faster to compute and integrate the total gravitational potential at every cell/particle, even for simulations with billions of resolution elements.

### 1.2.2 Modeling non-radiative gas

The evolution of fluids is described by the Euler-Lagrange equations, which state the conservation of mass, momentum and energy within a finite volume.

$$\frac{\partial \rho}{\partial t} + \bigtriangledown \cdot \rho \mathbf{v} = 0 \tag{1.6}$$

$$\frac{\partial \rho \mathbf{v}}{\partial t} + \bigtriangledown \cdot \rho \mathbf{v}\mathbf{v} + \bigtriangledown P = \rho g \tag{1.7}$$

$$\frac{\partial \rho E}{\partial t} + \bigtriangledown \cdot (\rho E + P)\, \mathbf{v} = \rho \mathbf{v} \cdot g \tag{1.8}$$

These equations can be written, and therefore solved, in two ways - one within a finite volume, and the other within a finite, moving element of mass. These are known as the Eulerian and Lagrangian approaches, respectively, and are often compared to looking at a stream from its banks versus observing it while flowing along with the current. Both describe the same system, but from different perspectives. Popular Eulerian or Adaptive Mesh Refinement (AMR) codes include FLASH (Fryxell et al., 2000), ENZO (Bryan & Enzo Collaboration, 2014), RAMSES (Teyssier, 2002) and ART (Kravtsov et al., 1997), while Lagrangian or Smoothed Particle Hydrodynamics (SPH) codes include GADGET (Springel et al., 2005), Gasoline (Wadsley et al., 2004) and GIZMO (Hopkins, 2015). Moving-mesh codes like AREPO (Springel, 2010) attempt to bridge the gap between the two, approaching the Eulerian formulation when an element is static and the Lagrangian one when it is moving at a high velocity. My idealised simulations use the AMR code GAMER-2 (Schive et al., 2017), while RomulusC uses the SPH code ChaNGa (Menon et al., 2015).

### 1.2.3 Sub-grid models

All the remaining physics is implemented in the form of "sub-grid" models. These account for radiative cooling, star formation, stellar feedback, and supermassive black hole (SMBH) formation and feedback. For example, the sub-grid models used in RomulusC are described in Paper II. Recent simulations have also started including the impact of cosmic rays, plasma viscosity and thermal conduction, and magnetic fields (e.g., Kunz et al., 2011; ZuHone et al., 2013; Kannan et al., 2016; Roberg-Clark et al., 2016). Our understanding of the last few phenomena, however, is still rapidly evolving and has not yet crystallised, and it is important to understand the basic mechanisms, such as ideal MHD, before adding further ingredients. To this end, Paper III takes a first step towards modeling the full microphysics of the ICM by focusing on modeling the well-defined ideal MHD problem in clusters.

These sub-grid models were crucial to testing cosmological theories against observations. Placing a luminous galaxy in every dark matter halo from an N-body simulation

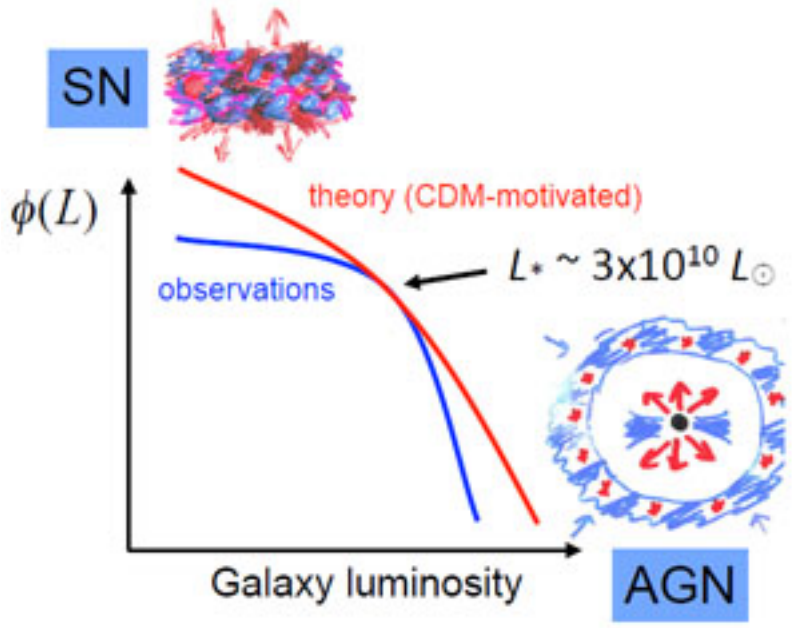


Figure 1.3: The need for feedback to reconcile the observed galaxy luminosity function with the halo mass functions from $\Lambda CDM$, as illustrated by Silk & Mamon (2012)

with a luminous galaxy predicted far too many galaxies in the Universe, including in the immediate vicinity of the Milky Way; this came to be described as the *missing satellite problem* (Kravtsov et al., 2004; Bullock & Boylan-Kolchin, 2017). Further, the mass-to-light ratio of galaxies seems to be lowest around the characteristic luminosity $L_*$ for a given redshift, where the Schechter luminosity function begins its exponential decay (Marinoni & Hudson, 2002; Treu & Koopmans, 2004; Vale & Ostriker, 2006). The explanation turned out to be that in small galaxies, stellar feedback blows out much of the gas early on in the halos history that not much is left for further star formation(Brooks et al., 2013; Wetzel et al., 2016). In high mass halos, a similar effect occurs due to feedback from SMBH, also known as Active Galactic Nuclei (AGN)(Dekel & Birnboim, 2006; Dutton & Treu, 2014). In the absence of feedback, radiative cooling produced runaway flows of cooling gas in the centres of halos, which led to star formation rates hundreds of times higher than observed, and galaxy cluster cores that were too cold and high in entropy (Croton et al., 2006; Fabian, 2012; Kormendy & Ho, 2013).

## 1.3 Cosmology with Galaxy Clusters

The primary test of cosmology with galaxy clusters is using cluster counts as a function of redshift (e.g., Vikhlinin et al., 2009a,b; Mantz et al., 2015). As mentioned in §1.1, the rate of formation of collapsed structures depends on the balance between attractive

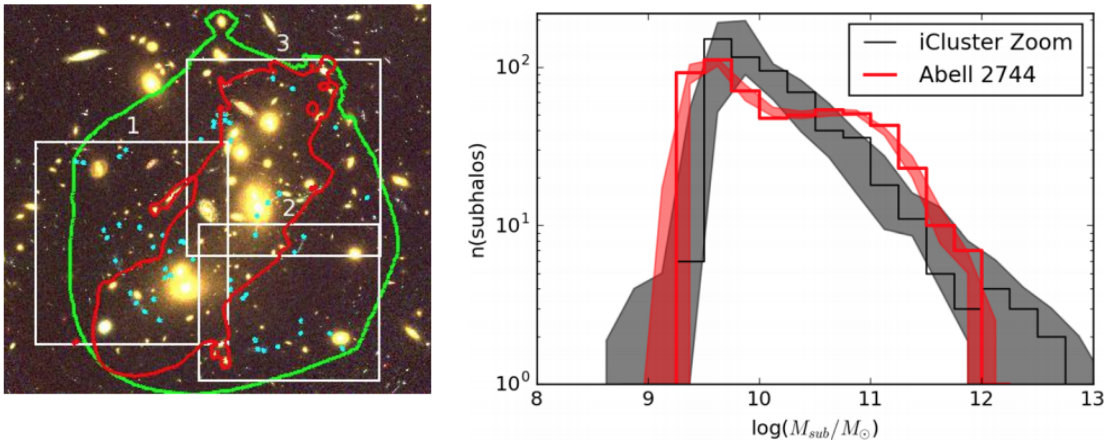


Figure 1.4: *Left:* The critical line for a source at z = 7 for the merging galaxy cluster Abell 2744 is shown in red (Richard et al., 2014). The mass model was built using strong and weak lensing observations as part of the *Hubble Frontier Fields* program. *Right:* The mass function of galaxy dark matter halos in the merging cluster Abell 2744 (red) vs that of subhalos in the full-physics cosmological simulation of a galaxy cluster of comparable mass using the moving-mesh code AREPO (Natarajan et al., 2017). The two distributions were count-matched, i.e., the simulation did produce more low-mass halos, but only the N brightest ones were used for this comparison, to match the fact that the faintest galaxies would not be observed. There is no renormalisation of the simulated subhalo mass function. The agreement between the two is excellent, with only a slight observed overdensity around $10^{11.5} M_\odot$. This is the halo mass where AGN feedback starts to become important, offering one potential explanation. The other could be contamination by other subclusters in Abell 2744 - which is known to be a highly complex merger with at least four distinct components, whereas the mass model in this paper modelled only two. The "virial" region considered in this study could well have contained galaxies from more minor subclusters, modifying the simple mass function predicted for simulations of a single virialised halo.

and repulsive forces. In the absence of dark energy, for example, structure would form more quickly, since the gravity would only have to fight a constant Hubble expansion. If the dark matter were made out of lighter particles, such as neutrinos or axions, their thermal velocity in the early Universe would be much larger for cold, heavy particles like the currently popular Weakly Interacting Massive Particles (WIMPs); these high velocities would make it easy for them to escape any potential wells rather than settle into them.

A second test comes from measurements of the gas fraction $f_{gas} = M_{\rm gas}/M_{\rm tot}$ within a certain $r_\Delta$. If the gas density profile $\rho(r)$ and temperature profile $T(r)$ can be measured, say, from X-ray observations, we can measure the gas fraction within the observed region. The conversion from observed flux to intrinsic luminosity, and therefore mass, requires a knowledge of the luminosity distance as well as angular diameter distance:

$$L_x = 4\pi D_L^2 B_x L_x(R) = L_x(\theta) \times D_A(z) \tag{1.9}$$

so that $f_{gas}$ itself is a measure of cosmology. Analytic theory and simulations predict $f_{gas}$ to be constant, approaching the cosmic baryon fraction, at the scale of galaxy clusters, so that we could hold it fixed and solve for the cosmological parameters. This argument was used to show the significance of dark energy in the cosmic energy budget (Allen et al., 2002, 2004).

Both these tests, then, rely on the knowledge of galaxy cluster masses. The following section describes how this is measured in different regimes - the X-ray, the sub-millimeter, and gravitational lensing.

### 1.3.1 Multi-wavelength observations

Galaxy clusters were first identified as overdensities of galaxies in optical surveys. The Abell catalog Abell (1958), for example, includes over 4073 systems from every part of the sky. Optical catalogs start with the richness, i.e., number of member galaxies, in a cluster. As observations get deeper, they can yield colors and magnitudes for the galaxies, which in turn can be used to compute photometric redshifts; even deeper observations can yield spectra, which provide much more precise redshifts. The redshifts tell us how far away the system is as a whole, and if this can be measured for a significant number of member galaxies, the velocity dispersion can translate to a measurement of the cluster mass. More coarsely, the cluster mass can be estimated through scaling relations with the cluster richness or optical luminosity.

The galaxies, however, are only a tiny fraction of the mass in clusters. The bulk of the baryonic mass lies in the intracluster gas. This gas, as it equilibriates with the deep gravitational potential of the cluster, heats up to average temperatures of $10^7 - 10^8$K. At these temperatures, the gas is almost fully ionised, and its dominant cooling channel is Bremsstrahlung or "braking radiation", wherein electrons decelerate and emit X-rays as they

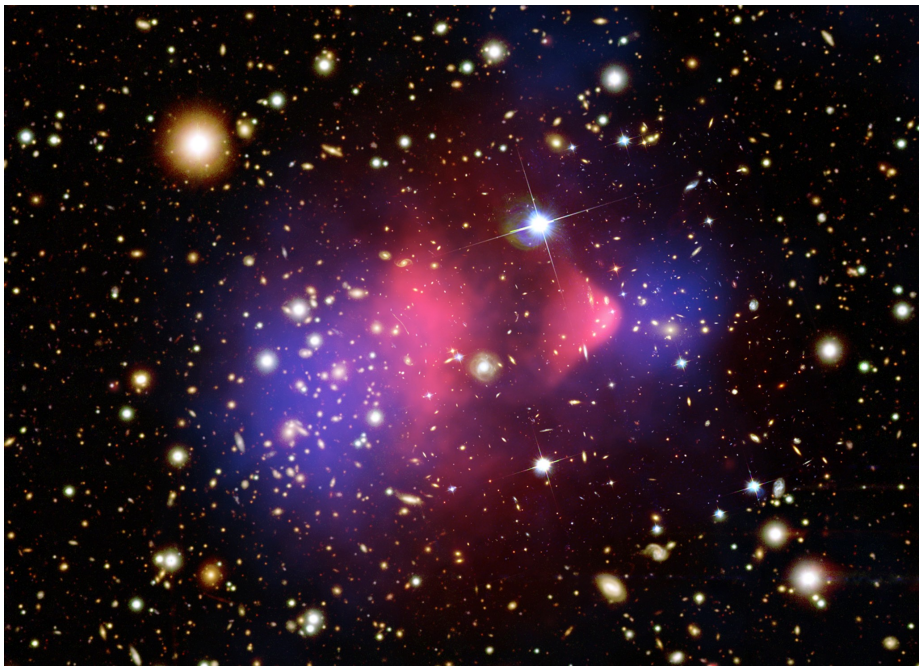

Figure 1.5: The Bullet Cluster (Markevitch & Vikhlinin, 2007) is considered one of the most compelling pieces of evidence for dark matter. The gas from the merging components is seen in the X-ray (pink), and does not overlap with the bulk of the mass from gravitationally lensing (purple). The separation between the gas, stars and dark matter has also been used to place constraints on the cross-section of self-interaction of dark matter. Systems like the Bullet Cluster, while very cosmologically insightful, are far from equilibrium and need to be understood with simulations.

pass by ions. X-ray telescopes are therefore extremely effective at finding galaxy clusters, especially if they are close enough to be spatially extended and therefore distinguished from point sources such as quasars and X-ray binaries. The temperature and X-ray luminosity of the gas also correlates to the dark matter mass, although with some scatter; the scatter is lower for temperature than for luminosity, and reduces if the central $0.15R_{500}$ is excised from the measurement. This is because baryonic process are particularly dominant in this central region.

The ICM can also be observed via the Sunyaev-Zel'dovich effect (SZE), wherein CMB photons undergo inverse Compton scattering by the hot ICM electrons. This is observed as an SZ decrement, i.e., a dark spot in the CMB. The power of the SZ effect is that, unlike X-ray or optical luminosity, it does not get fainter with distance. The CMB acts as a "backlight" at z $\sim$ 1100, and all clusters in the Universe lie in front of it. Therefore, as long as they are massive enough to cause a temperature dip that can be resolved by a sub-millimeter telescope, clusters will produce a detectable SZ signal. For this reason, SZ samples of galaxy clusters are called mass-selected. The SZ signal, quantified by the Compton Y parameter (which in turn is proportional to the gas thermal pressure), also scales with the total mass of the cluster, and has a lower scatter than other observables.

Last but certainly not least, the total mass of the cluster can be measured directly using gravitational lensing. The deep gravitational potential of galaxy clusters curves space-time around it, so that the straightest path, or geodesic, for light from sources behind it follows a curved path. Within the Einstein radius, which for galaxy clusters is of order 100s of kpc, the result is strong gravitational lensing, where a single background source produces multiple images. Multiple images can also occur outside the very core of a galaxy cluster if a member galaxy is in just the right place to boost the local surface density above the critical value required for strong lensing. Outside this region, there is weak gravitational lensing, where extended objects, like galaxies, become stretched out tangentially to the potential lines. In fact, one additional way that galaxy clusters help probe cosmology is that they magnify high-redshift galaxies and quasars, making it possible to compare their respective luminosity functions to theoretical models.

The advantage of gravitational lensing is that it measures the total mass, and doesn't rely on assumptions of equilibrium between the baryonic and dark matter. On the other hand, these measurements require really very deep observations to get a sufficient number of background galaxies. For example, the Hubble Frontier Fields (HFF) observed six clusters of galaxies for 630 hours, or 560 orbits. This depth is required to accurately measure the shape of the background galaxies, both individually and in a statistical sense. They do rely on the assumption - validated by observations of "blank", unlensed fields like as the Hubble Ultra-Deep Field, as well as unlensed fields observed in the HFF project - that the shape distribution of the background galaxies is well known and universal. Instead, the shape distribution could vary with such properties as redshift, galaxy mass/luminosity, and simply cosmic variance. This "shape noise" usually limits the signal-to-noise of lensing

measurements, so that non-parametric models that fit the projected mass in individual regions have large uncertainties. The uncertainties are reduced in parametric models, which assume some analytic form for the radial profiles of galaxy clusters, such as NFW or Einaasto. For all but the deepest observations, assumptions have to be made about the concentration of the halo, which is degenerate with the total mass. In summary, while lensing is a powerful measure of the total mass in a region, very few observations have sufficient signal-to-noise to fully harness this power. There is usually a trade-off between assuming parametric forms for the dark matter profile and larger error bars.

A multi-wavelength approach to cluster mass estimation promises to ensure robust and accurate cluster mass estimation by providing cross-checks on the systematics in different approaches. We learn about the galaxies from the optical and infra-red, about the ICM from the X-ray and SZE, and about the dark matter from gravitational lensing. Simulations allow us to connect all of these to each other.

### 1.3.2 Weighing galaxy clusters

As we now understand, cosmological models make predictions for the *halo mass function*, i.e., the number density of virialised structures of a given mass at a given redshift. To first order, these predictions can be made using dark matter models alone; however, incorporating stellar feedback suppresses the low-mass end of the mass function, while AGN feedback can hamper the high-mass end.

Of course, we cannot see the dark matter in the halos. Instead, we have to infer the total mass of galaxy clusters through observable effects. This section describes three of the most powerful ones - gravitational lensing, the X-ray emission of the intracluster gas, and the Sunyaev-Zel'dovich effect produced by cluster electrons on the cosmic microwave background (CMB).

#### Hydrostatic Mass Measurements

The intracluster medium (ICM), with its temperatures of $10^{6-8}K$, is almost fully ionised and therefore cools primarily through thermal Bremsstrahlung or "braking radiation". This is produced when electrons fly past ions, and curve towards them; the kinetic energy lost in this deceleration is emitted as X-ray radiation.

The direct measurements in the X-ray are photon lists, with the energy and position of each photon. The first thing compiled from these is a surface brightness map. While in principle the emissivity depends on both the gas density and temperature, $\epsilon = n_g^2 \Lambda(n, Z, T)$, in practice the temperature dependence is negligible. The density profile is therefore the square root of the surface brightness profile, upto a constant scaling factor.

$$\rho_g(r) \propto \sqrt{\Sigma_X(r)} \tag{1.10}$$

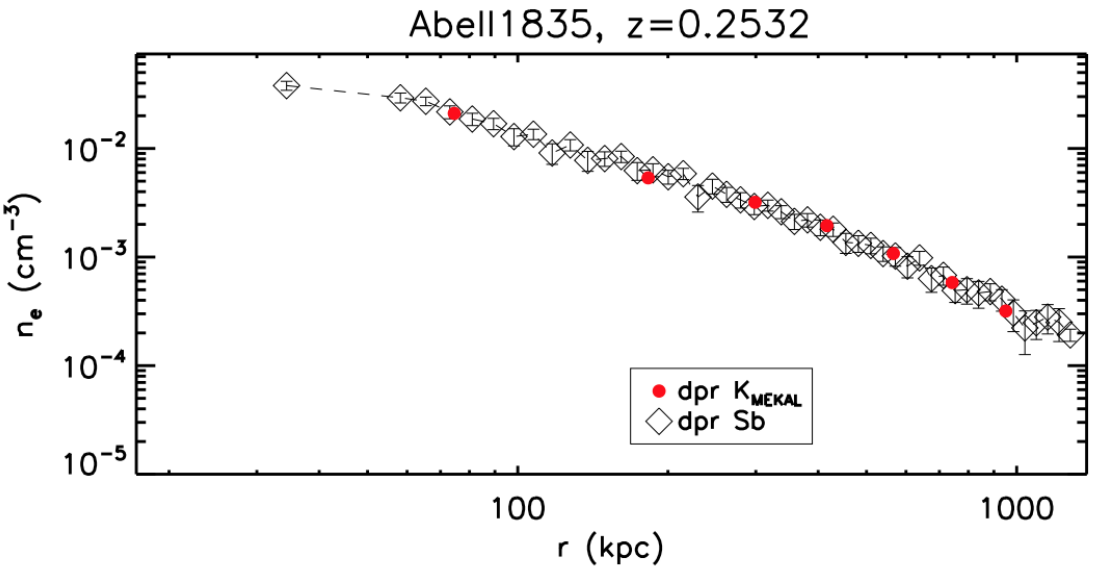


Figure 1.6: The gas density profile measured from X-ray observations of the galaxy cluster Abell 1835 (Ettori et al., 2013). The black diamonds and the line through them were measured by deprojecting the surface brightness profile. The red points show the best-fit normalisation of the temperature spectrum as fit by the MEKAL model of atomic emission, a simple consistency check.

To avoid biasing by clumpy gas, visible substructure is masked out by eye before extracting the radial profiles. The $T(r)$ measurement is harder, as it requires fitting a spectrum to each radial bin. In practice, the map is divided into regions such that each one has enough photons to individually have a spectrum fit.

Measurements of the total mass fundamentally rely on the assumption that the ICM is in hydrostatic equilibrium (HSE) with the total gravitational potential:

$$\frac{dP}{dr} = \frac{1}{\mu m_p}\left(\frac{d\rho}{dr} + \frac{dT}{dr}\right) = -\frac{GM(r)\rho(r)}{r^2} \tag{1.11}$$

where $P$ is the thermal pressure, $\mu$ the mean molecular weight, $m_p$ the mass of a proton, $T$ the gas temperature at $r$, $\rho$ the gas density, $G$ the gravitational constant and $M$ the total mass enclosed within $r$. The above equation holds for the 3D coordinate $r$, whereas we always observe the projected distance $R$. It is therefore necessary to first deproject the observed profiles. Alternatively, observers sometimes start with an analytic form for the density and/or temperature profiles, and fit the projected version to the data (Ettori et al., 2013). Either way, it is standard to assumed spherical symmetry; simulations have shown that deviations from spherical symmetry only bias the mass measured in this way by a few percent (Piffaretti et al., 2003).

Besides clumpy substructure, AGN are the major contaminant in X-ray mass measure-

ments. If the system is luminous enough, and the system is observed in at least two bands, the AGN can be modelled out because its X-ray emission is harder, i.e. peaks at higher energies, than that from the intracluster medium. The total energy can be inferred via scaling relations of the hard X-ray flux, and its contribution to the surface brightness profile is modelled as a point spread function. This gets harder to do as the galaxy cluster is further away; AGN contamination can bias temperature (luminosity) measurements by 24 (22)$\%$ at z $>$ 0.7 (Branchesi et al., 2007). Understanding the distribution of AGN, and their correlation with galaxy cluster properties, becomes particularly important in low-resolution, large-volume surveys like eROSITA.

Masking out substructure, modelling out AGN, and measuring density and temperature profiles in radial bins all requires a lot of photons, and is only feasible for relatively nearby (low-redshift) clusters. When compared with weak lensing masses from *Subaru*, X-ray masses from *XMM-Newton* for relaxed clusters were found to be biased low by $9\pm6\%$ while those of disturbed clusters were biased high by 6 $\pm12\%$ (Zhang et al., 2010). The former was attributed to the effect of non-thermal pressure, while the latter to adiabatic and/or shock heating during mergers. Once detailed measurements, with their biases, are measured for a sample of well-resolved clusters, they yield scaling relations with easier to measure properties such as the total X-ray luminosity $L_x$, the single-fit temperature $T_x$, and the X-ray Compton-like parameter $Y_x = T_x \times M_{gas}$. These are then used to infer the masses of systems observed with fewer photons.

Mass calibration using velocity dispersion are $16\%$ higher than those using the X-ray parameter $Y_x = T_x M_{\rm gas,500}$ (Bocquet, 2015); in other words, assuming the gas to be in hydrostatic equilibrium underestimates the mass by this amount. When compared with gravitational lensing masses from the CLASH survey, Planck masses were found to be $\sim 28 \pm 5\%$ lower, with the difference greater for low mass clusters (Penna-Lima et al., 2017); a similar bias was seen with the lensing masses from the Subaru Hyper Suprime Cam (HSC, Medezinski et al., (Medezinski et al.)).

### Gravitational lensing

Gravitational lensing is the most direct measure of the mass of a cluster. It makes use of the fact that a massive screen, like a lens, bends the path of light passing through it. Unlike a lens, where this happens due a higher refractive index, in a gravitational lens it is spacetime itself that is bent, following Einstein's rules of gravity. Light then takes the shortest possible path through this curved spacetime. For a comprehensive review of gravitational lensing in galaxy clusters, see Kneib & Natarajan (2011). Here, I present a summary to set the context for my work.

Cluster lensing uses the *thin lens approximation*, which notes that the thickness of a galaxy cluster is negligible compared to the distance between any background sources and us, the observers. The strength of the lensing effect, measured by the deflection angle $\alpha$ of

a background point source, then depends on the projected gravitational potential along the line of sight between the observer and the source:

$$\alpha = \frac{2}{c^2}\frac{D_{LS}}{D_{OS}}\vec{\nabla}\phi(\vec{\theta}) \tag{1.12}$$

where $D_{OS}$ is the angular diameter distance between the source and observer, and $D_{LS}$ the same between the source and the lens. The projected potential, in turn, depends on the projected surface density $\Sigma$. The source gets strongly lensed, or multiply imaged, if light from it passes through a region of projected density greater than the critical value $\Sigma_{\rm crit}$:

$$\Sigma_{\rm crit} = \frac{c^2}{4\pi G}\frac{D_{OS}}{D_{OL}D_{LS}} \tag{1.13}$$

where $D_{OL}$ is the angular diameter distance between the observer and the lens, $G$ the gravitational constant and $c$ the speed of light.

For the large-scale gravitational potential of a typical galaxy cluster, the critical density is only achieved in the central 100-200kpc. However, clusters are full of individual galaxies, whose potentials, when overlaid on that of the cluster, can locally push the projected density above the critical value. If a source happens to lie just behind those positions, it can get strongly lensed. The region of strong lensing is defined by "critical lines" and can look quite complicated; the left panel of Fig 1.4 shows this for the complex merging cluster Abell 2744.

Strong lensing is thus only possible in limited regions of galaxy clusters, but provides very robust constraints, since the crucial information is in the number, magnification, and position of the multiple images. In the rest of the cluster, we are in the regime of *weak gravitational lensing*, where the convergence $\kappa = \Sigma/\Sigma_{\rm crit} << 1$. This is indeed the dominant way of measuring cluster masses, especially in large surveys like DES and the upcoming LSST.

Weak lensing induces a *gravitational shear* $\gamma$, i.e., it increases the ellipticity of background galaxies. In terms of the reduced shear $g = \frac{\gamma}{1-\kappa}$, for the weak lensing approximation, the complex ellipticity in the image (observed) plane is modified as:

$$\epsilon_I = \epsilon_S + g \tag{1.14}$$

Of course, this requires a knowledge of the intrinsic shape of the source galaxy. Galaxies may be elliptical, lenticular or spiral, and in the latter two cases, their apparent shapes depend on their orientation with respect to the plane of the sky. Therefore, determining $\epsilon_S$ is only possible to do on a statistical level, by looking at blank, unlensed fields. Then, the reduced shear $g$ can be measured in any region where there are enough background galaxies to have sufficient signal-to-noise in the shape measurement.

For an individual cluster, the mass measurement is much more certain if there is also

strong lensing, which at least constrains the central region. Furthermore, lensing analyses usually assume a parametric form for the cluster profile, such as NFW (Navarro et al., 1996); this is defined by 2 parameters, the scale radius $r_s$ and the virial mass $M_{200}$ or, equivalently, the concentration $c_{200} = r_{200}/r_s$. As usual, $r_{200}$ is the radius within which the average density of the cluster is 200 times the critical density of the Universe $\rho_{crit}$, and $M_{200}$ is the mass within it. Typical scatters in weak lensing masses are 20-25$\%$ (c.f. Mantz et al., 2015). It is very rare to have enough S/N to independently constrain two parameters for the mass model; therefore, usually, the concentration is marginalised over. If it is not, the cluster mass can be significantly over/underestimated, as we see in the case of Abell 2146 in Chapter 3.

Even for the best case scenario, lensing measurements are not without their assumptions. They very often assume spherical symmetry, whereas simulations indicate that galaxy clusters tend to be triaxial (Jing & Suto, 2002; Becker & Kravtsov, 2011). Lensing is more likely to be detected in systems where the major axis is along the line of sight, so the error introduced is systematic, not random. Second, the NFW halo is assumed to be centered on the Brightest Cluster Galaxy (BCG). Even for relaxed clusters, the BCGs can be offset from the cluster potential minima by 10-100 kiloparsecs; the offset is even larger for merging clusters (Mann & Ebeling, 2012; Lopes et al., 2018). Line-of-sight structure further introduces errors, and is expected to increase the error bars by a factor of 2 (Hoekstra, 2003).

In summary, while weak lensing is a direct probe of the mass distribution of galaxy clusters, it is sensitive to the mass along the line-of-sight, instead of the mass enclosed within the virialized regions of the clusters, rendering the lensing mass to be prone to the projection effects. They are very useful in calibrating the masses from other techniques, such as those described below, which can have higher precision but be systematically offset from the "true" mass of the system.

### 1.3.3 Using simulations to interpret observations

Numerical simulations allow us to study the relationship between the dark and visible matter, since we know the "true" properties of both. They come in several flavours, most prominently idealised, cosmological, semi-analytic, and semi-empirical. In my thesis I focus on the first two.

Cosmological simulations start in the very early Universe, with a Gaussian random density field of dark matter and gas, which over time collapses into halos, with the gas forming stars and black holes and each of them eventually providing energetic feedback. These more realistically capture the complex formation histories and baryonic processes within galaxy clusters. Processes like the formation and feedback from stars and super-massive black holes are implemented as sub-grid models, which in turn are calibrated to match observations. Today, we are at a point where, at least as far as galaxy clusters are

concerned, cosmological simulations seem to do a good job reproducing observations. The right panel of Fig 1.4 shows the incredibly good agreement between the subhalo mass function measuring using gravitational lensing in the merging cluster Abell 2744, and a cosmological cluster simulation using the AREPO code Natarajan et al. (2017). Paper 1 uses the highest resolution cosmological simulation of a galaxy cluster to date, RomulusC, to compare the effects of AGN and a merger on the intracluster medium.

The downside of cosmological simulations is that they are very computationally expensive - state-of-the-art simulations run on thousands of cores for several months. This makes it prohibitively expensive to run suites of simulations to study the effect of varying any one of the numerous models, sub-grid or otherwise, involved. Idealised simulations are therefore a very helpful, complementary tool for studying roles of individual physical processes in shaping the formation and evolution of galaxy clusters. These start with galaxy clusters in equilibrium with certain analytic forms for the distribution of the dark matter and baryons. They then test out various prescriptions for AGN feedback, turbulence, or detailed gas physics; these clusters can also be made to collide with each other. Idealised simulations are, in other words, highly controlled experiments that test the specific impact of changing one parameter at a time, *under the assumption that all the analytic prescriptions hold*. The simulation volume is much smaller than that of cosmological simulations, allowing a much higher resolution for the same computational power, and/or allowing many simulations to be run in a reasonable amount of time. Papers II and III use suites of idealised simulations - the first hydrodynamic, the second including magnetic fields - to model the observed merging galaxy cluster Abell 2146. In the process, I also performed the most extensive study to date of the effect of various halo properties and geometry on the X-ray and lensing observations of cluster mergers.

## 1.4 Open Problems in Cluster Astrophysics

When galaxy clusters are relaxed, the dark matter is related to the observable properties of baryons via conditions of hydrostatic and virial equilibrium (e.g., Nagai et al., 2007a; Eckmiller et al., 2011; Mahdavi et al., 2013; Anderson et al., 2015). In $\Lambda$CDM, however, structure forms hierarchically through mergers, which take a system far out of equilibrium (Nagai et al., 2007b; Poole et al., 2007; Cassano et al., 2013). Nelson et al. (2012) and Biffi et al. (2016), among others, have shown that whether or not galaxy clusters are in hydrostatic equilibrium correlates neatly with whether they have recently undergone a merger.

AGN feedback can similarly affect the scaling relations (e.g., Sun, 2009; Battaglia et al., 2010; Battaglia et al., 2012; Fabian, 2012). While only gravitationally relevant out to tens of parsecs, AGN are observed to produce powerful outflows hundreds of kiloparsecs (kpc) in size. Across several orders in magnitude, the power of radio jets from AGN has been

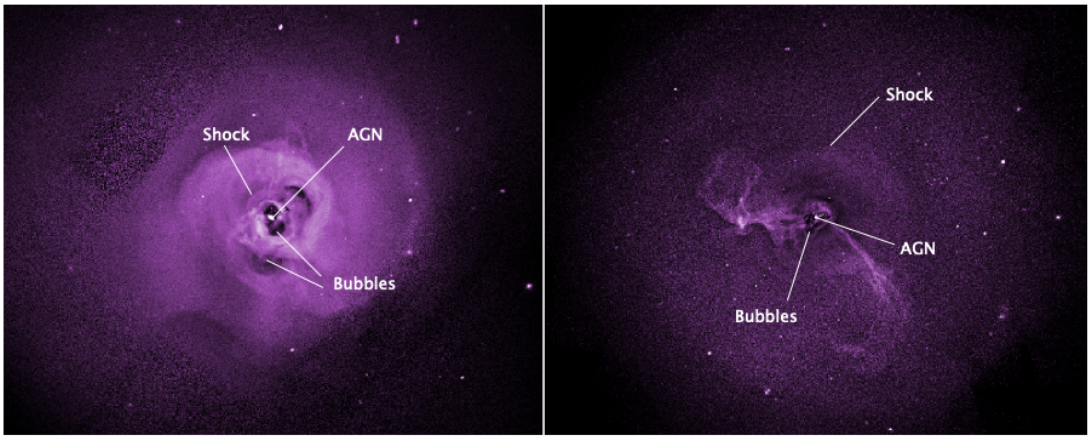


Figure 1.7: X-ray images of the Perseus and Virgo clusters (Simionescu et al., 2019). In both clusters, AGN show up as a bright central source. The outflows from the AGN expand in the ICM, leaving behind X-ray cavities which are instead filled with relativistic electrons and visible at radio wavelengths. The outflows heat the ICM through shocks, such as those seen here, are well as by generating and dissipating turbulence.

observed to correlate with the X-ray luminosity of their host clusters, which in turn quantify the cooling rate of the ICM (Fig 1.7). In simulations, AGN have been crucial to prevent runaway cooling flows. In their host galaxies, they prevent excessive star formation. As the jets entrain material on their way out from the galaxy/cluster core, they carry with them not only thermal energy but also metal-enriched gas, explaining the chemical enrichment of the ICM over cosmic time.

So far, X-ray cluster cosmology has been carried out with samples of 60-80 deeply-observed clusters, most of them at low-redshift and/or high masses. This ensures that we have enough X-ray photons to mask out substructures and central AGN, and remove the core region of $r = (0 - 0.15)R_{500}$ where the scatter in scaling relations is particularly large due to galaxy formation processes in the BCG. Meanwhile, the *eROSITA* X-ray survey telescope is finishing its second year of operation, and is on track to find 100,000 galaxy groups and clusters over its four-year lifetime. Many of these will have very few photons, not enough for core excision, temperature measurements, or removing or even identifying merging substructure. The Planck Collaboration (2020) did not use galaxy cluster counts to constrain cosmological parameters, even though clusters are very easy to detect in their data, because of the uncertainty in the calibration from SZ to the total masses. This calibration happens via X-ray observations under the assumption of hydrostatic equilibrium. To fully harness the power of galaxy clusters as laboratories for both cosmology and astrophysics, we need an understanding that includes AGN and mergers, rather than excludes them.

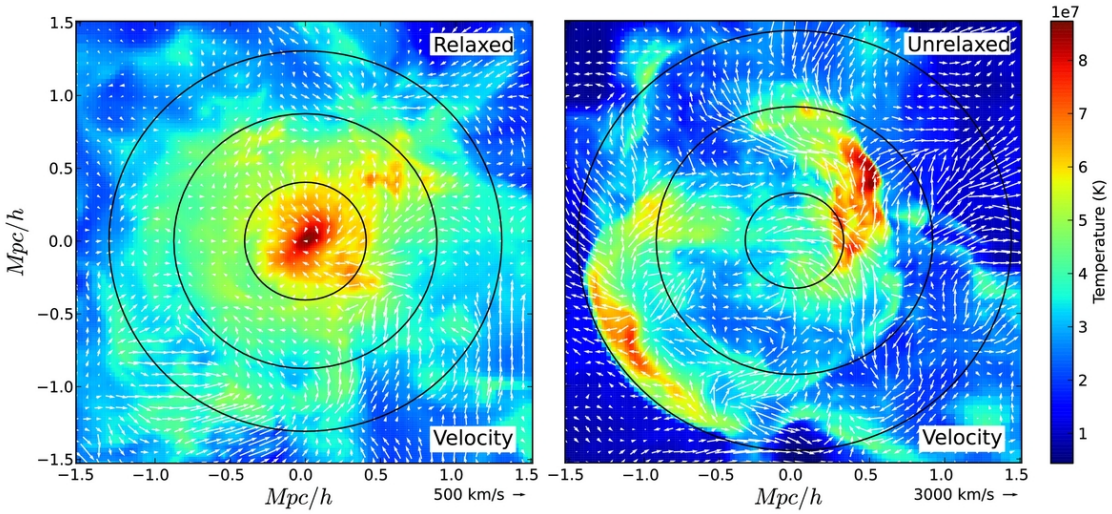


Figure 1.8: The temperature (colour map) and velocity field (vectors) in a relaxed (left) and merging (right) galaxy cluster, as seen in the $\Omega_{500}$ simulation. The former is well described as being a hydrostatic equilibrium (HSE), whereas the latter has significant non-thermal pressure from bulk flows and shocks (Nelson et al., 2014). A mass estimate for the merging system assuming HSE would significantly underestimate the total mass.

### 1.4.1 A cool-core/non-cool core dichotomy

X-ray observations of galaxy clusters have found a large diversity in the entropy of the gas in cluster cores, with some authors claiming a bimodality between cool- and non-cool cores. In cool cores, the entropy decreases monotonically all the way into the cluster centre, following the $K \propto r^{1.1}$ relation expected from gravitational collapse alone. These cluster cores also contain $H-\alpha$ emitting gas, which at $10^4$ $K$ is in a different phase from the diffuse, hot ICM. The entropy profiles of non-cool core clusters, on the other hand, flatten within $\sim 0.1R_{500}$, so that the central entropies are 10-100 times higher than in cool cores. No $H-\alpha$ emission is observed in these clusters.

Understanding this dichotomy has both astrophysical and cosmological consequences. Cool cores are more centrally concentrated, and since the X-ray luminosity $L_x \propto \rho_g^2$, where $\rho_g$ is the gas density, cool-cores are much brighter than non-cool cores for the same total mass. For one, this means that scaling relations between X-ray luminosity and total mass are different for cool- and non-cool cores. Second, it means that cool-core clusters are more likely to be detected in flux-limited surveys; if the selection is done on mass, for example using the SZ effect, this bias is removed and the fraction of non-cool cores increases. This directly affects the halo masses inferred from large samples of poorly resolved galaxy clusters, and therefore cosmology using cluster mass functions.

On the astrophysical side, the distribution of cluster core properties tells us about the balance between different heating and cooling processes in the intracluster medium.

Radiative cooling brings in gas from outskirts into the core; AGN recycle some of this gas into hot, relativistic outflows. Mergers generate entropy via strong shocks as well as turbulence. If there is no cold phase gas in the core, the galaxies therein have no fuel for star formation. If thermal conduction is efficient, large temperature gradients should be erased. If viscosity is important, a lot of heat would be dissipated close to where it is generated, whether via AGN outflows or merger shocks; on the other hand, very small fluctuations would be erased, and it is these small fluctuations that precipitate out of the diffuse hot phase into the cold phase that fuels star formation and AGN activity. The picture is highly complex and multi-scale.

In Paper I, I use the RomulusC cosmological zoom-in simulation of a $10^{14} M_{\odot}$ galaxy cluster to compare the ways that AGN and a major merger affect the multiphase structure of the ICM. I show that no matter how powerful the AGN, it is incapable of converting a cool-core into a non-cool one; it does, however, regulate star formation in the central galaxy. The merger, on the other hand, transfers over several orders of magnitude more energy to the ICM within one dynamical time via a major shock and subsequent sloshing, first "evaporating" the cold phase in the core and then raising the entropy of the hot phase by a factor of 5.

### 1.4.2 Weighing merging clusters

As noted above, most conversions of cluster observables into dark matter masses assume hydrostatic equilibrium; meanwhile, clusters form primarily through mergers, and are therefore often out of equilibrium. Shocks cause a temporary but dramatic increase the average luminosity and temperature, and the system is gravitationally compressed so that the effective concentration is much larger than for a relaxed system of the same mass. Especially in the age of large, lower-resolution X-ray surveys like eROSITA, we expect to find hundreds of thousands of galaxy clusters, many of which will be merging; converting these into total masses for tests of cosmology means we need to have a working model for merging clusters as well as isolated ones.

The outcome of a merger depends on many parameters - the mass and concentration of each subcluster, the infall velocity, angular momentum, and the viewing direction, among others. In Paper II, I perform a parameter search to identify the best-fit model for the merging galaxy cluster Abell 2146, which has been observed in the X-ray (Russell et al., 2010; Russell et al., 2012), radio (Hlavacek-Larrondo et al., 2018), SZ (AMI Consortium et al., 2011), optical (Canning et al., 2012; White et al., 2015) and gravitational lensing (King et al., 2016; Coleman et al., 2017). I show that the mass measurements from gravitational lensing were biased high 20-50$\%$, because they modelled two merging systems as a single NFW profile with a concentration reasonable for a relaxed halo of that mass but far too low for a system just post-pericenter passage, where mass in the centre is gravitationally compressed. This resolves an existing discrepancy between the mass estimated

from the X-ray and SZ on the one hand and lensing on the other. It also highlights the importance of correctly modelling the distribution function, including scatter, in the dark matter concentration of halos in weak lensing studies.

### 1.4.3 Magnetic fields and Transport Processes

At their core, the two problems above - the role of mergers and of AGN in shaping cluster observables - are questions about the transport of energy in the weakly collisional ICM. Paper II addressed this from a hydrodynamical standpoint, but we know that clusters are in fact also permeated by weak magnetic fields. These are understood to have been amplified from primoridial seeds by turbulence associated with accretion and mergers (Subramanian et al., 2006; Vazza et al., 2014), potentially producing dynamically significant pressures (Iapichino & Brüggen, 2012; Donnert et al., 2018; Stasyszyn & de los Rios, 2019). Even when weak, magnetic fields can significantly affect the viscosity and thermal conductivity of the cluster plasma (Spitzer, 1952; Sarazin, 1986). Nulsen (1982) showed that these two properties affect the rate at which gas is stripped from substructures into the intracluster medium, affecting the course of mergers. Beyond ICM physics, this has implications for the star formation and metallicity distribution in cluster galaxies. In Paper III, we study the effects of turbulent magnetic fields on the intracluster medium using the framework of ideal magnetohydrodynamics (MHD).

The primary method of observing magnetic fields is using radio observations. On small scales, we can use Faraday rotation, wherein the fields polarise light from background sources; this polarisation is most easily measured with radio telescopes (Clarke, 2004; Beck et al., 2012). Diffuse emission from radio mini-halos and relics yields magnetic field measurements on larger scales (e.g. Böhringer et al., 2016). Brunetti et al. (2009) show that merging and relaxed clusters are well-separated in the plane of $L_x$ vs $P_{1.4}$, where the former quantity traces the thermal and the latter non-thermal emission. This means synchrotron emission is temporarily amplified during the merger process, before decreasing again as the system relaxes.

Brzycki & ZuHone (2019) explained these observations with simulations of field strength $\beta = \frac{P_{\rm therm}}{P_B} = 200$ and a variety of mass ratios and impact parameters for merging clusters. They find that the fields are amplified by the merger via turbulence. Magnetic energy increases temporarily after pericenter passage, by $25\%$ greater than the initial value for all three impact parameters considered. The mergers also heat and expand the cluster core, however, so that, given sufficient time to relax, the system could end up with a smaller magnetic field than before the merger. The magnetic fields end up slightly isotropic, oriented more radially in the central $200 - 300\ kpc$ and more tangentially outside.

Paper III expanded on these results by considering several strengths of the magnetic field, isolating the role of turbulence, and deriving observable consequences for X-ray and radio observations. We challenge common assumptions in the interpretation of magnetic

field strengths from X-ray observations, and suggest new alternatives. This sets the stage for more detailed simulations, which add viscosity and thermal conduction on top of magnetic fields.

# Chapter 2

# Fountains and storms: the effects of AGN feedback and mergers on the evolution of the intracluster medium in the RomulusC simulation

*U. Chadayammuri, M. Tremmel, D. Nagai, A. Babul, T. Quinn*

[1]Department of Astronomy, Yale University, New Haven, CT, 06511, USA
[2]Chandra X-Ray Center, 60 Garden Street, Cambridge, MA, 02138, USA
[3]Department of Physics, Yale University, New Haven, CT, 06511, USA
[4]Yale Center for Astronomy and Astrophysics, New Haven, CT, 06511, USA
[5]Department of Physics and Astronomy, University of Victoria, Victoria, BC V8W 2Y2, Canada
[6]Department of Astronomy, University of Washington, Seattle, WA, 98195, USA

**Accepted to MNRAS April 7, 2021**

## Abstract

The intracluster medium (ICM) is a multi-phase environment, dynamically regulated by active galactic nuclei (AGN), the motions of cluster galaxies, and mergers with other clusters or groups. AGN provide a central heating source capable of preventing runaway cooling flows and quenching star formation, but how they achieve this is still poorly understood. We investigate the effects of AGN feedback and mergers on the ICM using the high-resolution RomulusC cosmological simulation of a $10^{14}$ $M_\odot$ galaxy cluster. We demonstrate that AGN feedback regulates and quenches star formation in the brightest cluster galaxy gently,

without any explosive episodes, and co-exists with a low entropy core with sub-Gyr cooling times. In contrast, the merger disrupts the ICM structure, heating the core and cutting off the supply of low-entropy, infalling gas that until then fuelled the AGN. We find that this removal of the low-entropy phase correlates with the ratio $t_{cool}$ / $t_{ff}$ increasing above 30 in the core, matching observations that cooling gas is only found in clusters where this ratio is 5-30. Importantly, we find that evolution in the inner entropy profile and the ratio of cooling to free-fall timescale are directly connected to the quenching of star formation in the BCG. This is in line with previous results from idealized simulations and confirmed here within a fully cosmological simulation for the first time.

## 2.1 Introduction

Galaxy clusters are the largest and most recently formed structures in the Universe, serving as a powerful laboratory for astrophysics and cosmology. One of the outstanding questions for cluster formation is understanding the cooling and heating balance that shapes the properties and evolution of cluster cores (De Grandi & Molendi, 2002; McCarthy et al., 2004, 2008; Edwards et al., 2007; Bildfell et al., 2008; Sun, 2009; Cavagnolo et al., 2010; Voit & Donahue, 2014; McDonald et al., 2018, 2019). The entropy of the cluster core is a simple metric that captures the net effect of heating and cooling processes. Its distribution has been observed to be slightly bimodal (e.g., Cavagnolo et al., 2009; Pratt et al., 2009; Sanderson et al., 2009), with the lower entropy clusters called cool-cores (CC) and the higher-entropy ones non-cool cores (NCC). Specifically, the entropy profiles of CCs decline monotonously into the central few kiloparsecs, while the NCCs have a flat, high-entropy core at the center. In CC clusters, the cores have remained relatively unchanged since $z \gtrsim 1.3$ (Santos et al., 2010; McDonald et al., 2017; Sanders et al., 2018), suggesting that a cluster's core state is set early in its evolutionary history.

The central regions of these CC clusters are typically observed to have cooling times much shorter than a Hubble time. The ICM is also a dynamic environment in which the gas is heated by the central AGN activities and stirred by mergers and galaxy motions at the same time.

Early simulations without feedback from active galactic nuclei (AGN) produced cooling flows, bulk flows of high-entropy gas from the outskirts towards the core, raising the core entropy over time (Lewis et al., 2000; Voit et al., 2002). Including AGN feedback suppressed these cooling flows and formed more realistic profiles, at least for the cool core category of clusters (Voit & Donahue, 2005; Sijacki et al., 2007; McCarthy et al., 2008; Guo & Mathews, 2010). However, reproducing the observed distribution of cluster core entropies has been elusive. Dubois et al. (2011), for example, find that in a cosmological simulation with AGN feedback, including metal line cooling produces only clusters with NCC; Planelles et al. (2014) also produce a cosmological suite with AGN feedback where

all the clusters resemble NCC. C-Eagle (Barnes et al., 2017) and Illustris-TNG (Barnes et al., 2018) include both AGN feedback and metal cooling, and do produce cool cores, although less frequently than observed. The C-Eagle study attributes the excess core entropy to heating by the AGN. Rasia et al. (2015) reproduced a realistic population of cluster cores using an improved SPH scheme along with a two-mode AGN feedback model corresponding to the quasar- and radio-modes with different efficiencies (Steinborn et al., 2014), but attribute this success primarily to improvements in the hydrodynamic solver that better capture gas mixing.

The other major heating source are cluster mergers - the most energetic events in the Universe since the Big Bang. With as much as $10^{64}$ ergs of initial kinetic energy, they are more than capable of significantly modifying the structure of a cluster core through shocks and mixing. Based on a joint X-ray and weak lensing analysis of observed systems, Mahdavi et al. (2013) find that cool-core clusters are more likely to be in hydrostatic equilibrium than their non-cool core counterparts, in contention with some recent simulation results (Barnes et al., 2018). Poole et al. (2006) and Hahn et al. (2017) find that low angular momentum mergers do not always disrupt CCs and even when they do, the central cooling time often does not increase to over $0.1t_H$. Overall, the emerging picture is that while mergers can heat cluster cores, the parameters of a merger, such as merger mass ratios and impact parameters, likely play a critical role. Even so, studies have found that in the presence of radiative cooling, the net heating lasts only 3-4 Gyrs, after which the core returns to its pre-merger entropy.

Recent observations of H-$\alpha$, infrared and molecular line emission have emphasised the multi-phase nature of the ICM, and the role of cold gas in mediating the interaction between AGN and the ICM (Salomé et al., 2006; Peterson, 2006; Risaliti et al., 2010; Grier et al., 2012; Tremblay et al., 2016). It should be noted that the key phases of the ICM are different from that of the interstellar medium, with the cool phase usually referring to gas at or below the H-$\alpha$ emitting threshold of $10^4$K (e.g., Gaspari et al., 2012; McCourt et al., 2012). This H$-\alpha$ emission has only been observed in clusters with central entropies below 30 keV cm$^2$ and correspondingly low central cooling times (Crawford et al., 2005; Salomé et al., 2006; Cavagnolo et al., 2008; Mittal et al., 2009; Hlavacek-Larrondo et al., 2012; Voit et al., 2015). Clusters with higher core entropies, on the other hand, had longer cooling times that flattened in the central regions and no detectable cold gas, and were much less likely to host an AGN, indicating that the AGN-ICM regulation is disrupted, or non-existent, in these systems.

Since the cold gas has a very low volume filling factor, capturing the formation of the multi-phase ICM requires resolution that has so far remained in the domain of idealised simulations. These have shown that the warm-hot ICM in the cluster core is in approximate global thermal balance, and becomes susceptible to local thermal instabilities when the ratio of the cooling time ($t_{\rm cool} \equiv E_{\rm therm}/[n^2\Lambda(T,Z)]$, where $\Lambda$ is the gas temperature and metallicity-dependant radiative cooling function) and the gravitational free-fall time

($t_{\rm ff} \equiv \sqrt{2r/g}$, where $g = GM(<r)/r^2$), drops below a threshold typically in the range 5-30 (e.g., McCourt et al., 2012; Sharma et al., 2012; Prasad et al., 2015; Voit et al., 2017). At this point, cold dense clouds start to condense out of the warm-hot ICM, fall towards the cluster centre, and eventually accrete onto the central black hole (e.g., Gaspari et al., 2013; Voit et al., 2015; Li et al., 2015; Lakhchaura et al., 2018). In this model, black hole accretion is set by the rate at which gas is able to 'precipitate' out of the hot/warm ICM, which in turn feeds the central SMBH; the resulting feedback regulates the cooling in the cluster core (Gaspari & Sądowski, 2017; Prasad et al., 2017, 2018).

Idealised simulations allow controlled experiments and high resolution, but crucially lack cosmological context. The amount of cold gas fueling the AGN activity is strongly boosted by the presence of turbulence (Gaspari et al., 2013; Prasad et al., 2017), but the bulk and turbulent motions generated by the cosmic accretion process are either left out or must be introduced by hand in an idealized way.

In cosmological environments, bulk and turbulent gas motions arise naturally from mergers and interactions of galaxies and galaxy groups within the cluster (Lau et al., 2009; Vazza et al., 2011; Nagai et al., 2013; Nelson et al., 2014) and penetrating streams from the cosmic web (Zinger et al., 2016). It is therefore useful to study the effects of AGN feedback and mergers on the evolution of cluster cores by using a fully cosmological simulation capable of capturing the roles of AGN feedback in a realistic cosmological context while resolving rich structure within the cool-warm ICM down to 100s pc scales.

In this paper, we use the high-resolution, cosmological, hydrodynamic, zoom-in galaxy cluster simulation RomulusC (Tremmel et al., 2019) to study in detail the effects of AGN feedback and mergers on the thermodynamics of the ICM. RomulusC simulates a low mass galaxy cluster with $M_{200} = 1.4 \times 10^{14} M_{\odot}$ and emission-weighted $kT_{500} = 1.4$keV at $z = 0$. With spatial and mass resolution of 250 pc and $10^5 M_{\odot}$, respectively, RomulusC approaches resolutions previously only attainable in idealized simulations of isolated clusters. At this resolution, RomulusC produces rich structures of gas with $T \gtrsim 10^4$ K (Butsky et al., 2019). For the purposes of this paper, we define "cooler gas" as that with $T < 10^5 K$. This resolution also makes it one of the highest resolution cosmological simulations of a halo of this mass to date, comparable only to the most massive halo from the TNG50 simulation (Pillepich et al., 2018; Nelson et al., 2019). As discussed in Tremmel et al. (2019), the ICM core in RomulusC remains at low entropy with sub-Gyr cooling times until the onset of a 1:8 mass ratio merger at z$\sim$0.14. Prior to this merger, star formation quenches due to AGN feedback. This simulation therefore offers a unique case study of the effects of AGN feedback and mergers on the ICM.

We describe the RomulusC simulation and its key baryonic physics prescriptions in §2.2. §4.3 presents the evolution of thermodynamic profiles, cooling time and precipitation rate, connects this to the behaviour of cooling, multi-phase gas at all radii. We discuss our results in light of previous work and important caveats in §3.5. Conclusions are summarized in §4.6.

## 2.2 The RomulusC Simulation

RomulusC (Tremmel et al., 2019) is a zoom-in cosmological simulation of a galaxy cluster with initial conditions extracted from a 50 Mpc-per-side dark matter-only simulation using the standard volume re-normalization technique of Katz & White (1993) and re-run with higher resolution and full hydrodynamic treatment using the Tree+SPH code, ChaNGa (Menon et al., 2015). The Romulus simulations use a spline kernel force softening of 350 pc (corresponding to a Plummer softening of 250 pc) and a minimum SPH smoothing kernel of 70pc. With dark matter and gas mass resolutions of $3.4 \times 10^5 \mathrm{M}_\odot$ and $2.12 \times 10^5 \mathrm{M}_\odot$ respectively, RomulusC resolves substructure down to $3 \times 10^9 \mathrm{M}_\odot$ with over $10^4$ particles, naturally including interactions between the ISM of in-falling galaxies with the ICM of the cluster environment. The cluster reaches $\mathrm{M}_{200}$ of $1.15 \times 10^{14} M_\odot$ by $z = 0$. ChaNGa uses prescriptions for gas cooling, star formation and feedback, and UV background from Gasoline (Governato et al., 2010), turbulent dissipation (Wadsley et al., 2017) and introduces a new model for supermassive black hole (SMBH) accretion, feedback, and dynamical evolution. All the free parameters for sub-grid models related to SMBH or stellar physics were tuned to reproduce a series of scaling relations for galaxies of Milky Way mass or smaller (Tremmel et al., 2017), so that results on the cluster scale are purely predictions of the model. The simulation assumes Planck cosmology: $\Omega_m$ = 0.3086, $\Omega_\Lambda$ = 0.6914, h= 0.67, $\sigma_8$= 0.82 (Planck Collaboration, 2015).

### 2.2.1 Star formation and gas physics

Star formation occurs in gas particles with density greater than $0.2 m_p\, cm^{-3}$ and temperature below $10^4$K. A star particle of mass $m_*$ forms out of a gas particle of mass $\mathrm{m}_{gas}$ with the probability:

$$p = \frac{m_{\mathrm{gas}}}{m_*} \left(1 - \exp(-c_* \Delta t / t_{\mathrm{dyn}})\right), \tag{2.1}$$

where the local dynamical time is $t_{\mathrm{dyn}} = \sqrt{3\pi/(32G\rho)}$, the characteristic timescale is taken as $\Delta t = 10^6$yr for star formation, and the star formation efficiency $c_*$ = 0.15. The latter is a free parameter tuned in Tremmel et al. (2017) to reproduce a series of scaling relations for MW-sized and dwarf galaxies. Star particles are assumed to follow a Kroupa IMF (Kroupa, 2001) to compute metal enrichment and supernova rates. Supernova feedback is implemented as a thermal injection with 75% coupling efficiency accompanied by a cooling shutoff in the surrounding gas, following the 'Blastwave' formalism from Stinson et al. (2006).

ChaNGa includes an updated SPH implementation that uses a geometric mean density in the SPH force expression, allowing for the accurate simulation of shearing flows with Kelvin-Helmholtz instabilities (Ritchie & Thomas, 2001; Governato et al., 2015;

Menon et al., 2015). The most recent update to the hydrodynamic solver is the improved implementation of turbulent diffusion (Wadsley et al., 2017), which does not occur on sub-resolution scales in traditional SPH codes (see Rennehan et al. 2019 and references therein). In the presence of gravity, where buoyancy and conduction lead to the separation of low and high-entropy gas, traditional SPH codes produce unphysically low-entropy cores (Wadsley et al., 2008; Mitchell et al., 2009) and fail to distribute metals over large radii (Shen et al., 2010; Rennehan et al., 2019). The combination of a gradient-based shock detector,time-dependent artificial viscosity, and an on-the-fly time-step adjustment system allows for a more realistic treatment of both weak and strong shocks (Wadsley et al., 2017). The CHaNGa solver is thus better numerically equipped to study the thermodynamics of turbulent environments, such as the ICM with frequent merger activity and AGN outflows.

As discussed in Tremmel et al. (2019), an important limitation of RomulusC is the lack of high temperature metal line cooling, a major coolant for gas in high mass halos such as the one we examine here. While the lack of metal line cooling certainly can affect the accretion of gas onto central galaxies, feedback processes, particularly from AGN, are also important (van de Voort et al., 2011a). This choice was made because the resolution of RomulusC, while unprecedented, is insufficient to resolve molecular hydrogen. Christensen et al. (2014) find that the inclusion of metal line cooling without a star formation prescription that accounts for molecular hydrogen results in overcooling. One possible solution to the overcooling problem would be to boost feedback efficiency (e.g., Shen et al., 2012; Dalla Vecchia & Schaye, 2012; Schaye et al., 2015; Sokołowska et al., 2016, 2018), but this will not necessarily provide a realistic ISM or CGM/ICM (Sokołowska et al., 2016). Another potential solution would be to only include metal line cooling in diffuse gas, but determining an arbitrary threshold below which unresolved multiphase structure exists is difficult and may have unforeseen affects on galaxy evolution. We therefore opt to not include it here. We discuss further in §4.4 how this lack of metal cooling may influence our conclusions.

### 2.2.2 The Romulus SMBH Model

The model for SMBHs and the AGN they generate in RomulusC differs from standard implementations in several key ways. First, black holes are seeded based on gas particle properties, rather than the host halo mass, as is common in the literature. Second, accretion onto SMBHs accounts for the presence of rotationally supported gas nearby the black hole. Third, the feedback model avoids prescribing a mass or accretion rate dependence to the feedback mode and instead only includes a simple model for thermal feedback which, thanks to the resolution and implementation of the model, naturally results in large-scale outflows that can quench star formation in massive galaxies (Pontzen et al., 2017; Tremmel et al., 2019). The SMBH model is described in further detail in Tremmel et al. (2017), so we only provide a brief overview here to highlight the aspects relevant to the AGN-merger

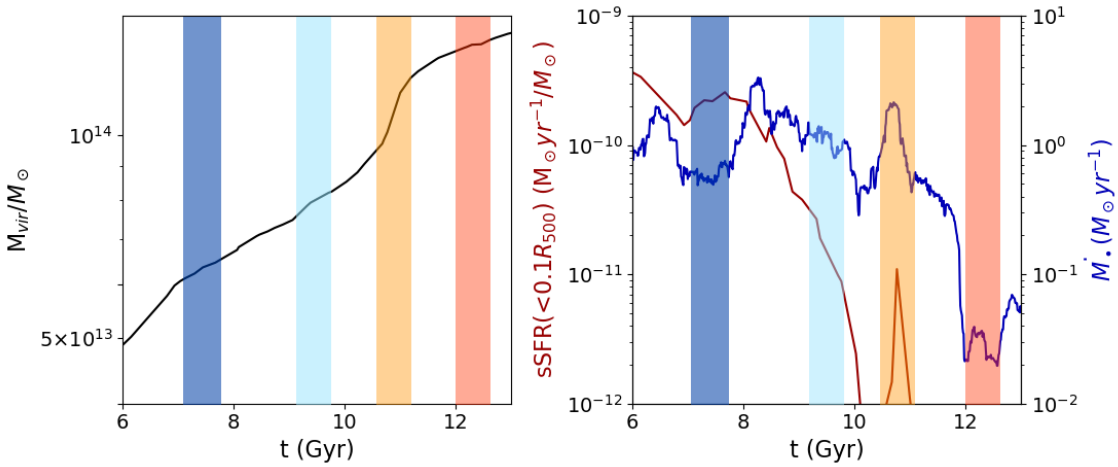


Figure 2.1: *Left panel:* Evolution of the virial mass of the RomulusC cluster over time. *Right panel:* Black hole accretion rate (blue) and specific star formation rate in the central 10kpc (red), both smoothed over 250Myr, over time in RomulusC. In this work, we specifically investigate the four key epochs indicated in the shaded color: before (purple) and after (blue) quenching, between quenching and beginning of the merger (orange), and during the merger (red). The horizontal dashed lines represent accretion rates corresponding to bolometric luminosities $10^{44}$ and $10^{45}$ ergs/s, assuming a radiative efficiency of 10%.

connection and impacts on core gas properties.

### Black hole seeding

Black holes are initially seeded in the simulation from a sub-set of potentially star-forming gas particles that (i) have densities that exceed 15 times the threshold for star formation, (ii) have very low metallicity ($Z < 3 \times 10^{-4}$), and (iii) have a temperature just below the limit of atomic cooling, 9500-$10^4$K. This physically identifies dense, quickly collapsing regions that are most likely able to grow a $10^6$ M$\odot$ black holes in the early Universe. Most other cosmological simulations posit instead that every halo will contain a SMBH by the time its mass hits a certain threshold, usually $10^{10-12} M_\odot$ (e.g., Sijacki & Springel, 2005; Steinborn et al., 2014; Weinberger, 2016; Stevens et al., 2017). In comparison, SMBHs in Romulus are seeded at higher redshift and in lower mass halos ($10^8 - 10^9 M_\odot$) in RomulusC. AGN feedback in RomulusC halos is allowed to begin much earlier ($z \gtrsim 5$) and in lower mass halos compared to other simulations of similar scale. Ricarte et al. (2019) find that in Romulus SMBH growth (and therefore feedback) traces the star formation of galaxies even at early times and in low mass halos. These results appear to be in contrast with other theoretical results showing a suppression of SMBH growth in low mass galaxies due to supernovae feedback (Dubois et al., 2015; Habouzit et al., 2017; Bower et al., 2017; Anglés-Alcázar et al., 2017).

We note that a lack of sustained SMBH growth does not itself prove that feedback from SMBHs is unimportant. Sharma et al. (2019) show that AGN feedback can have an effect on the evolution of low mass galaxies, which further highlights the importance of modeling these feedback processes in the early Universe. The high density environment of clusters may also result in unique episodes of AGN feedback as galaxies experience ram pressure (Ricarte et al., 2020).

**Black hole accretion and feedback**

Accretion is a slightly modified version of the Bondi (1952) model:

$$\dot{M}_\bullet = \alpha \times \begin{cases} \frac{\pi (G M_\bullet)^2 \rho}{(v_{bulk}^2 + c_s^2)^{3/2}} & \text{if } v_{\rm bulk} > v_\theta \\ \\ \frac{\pi (G M_\bullet)^2 \rho c_s}{(v_{bulk}^2 + c_s^2)^2} & \text{if } v_{\rm bulk} < v_\theta \end{cases} \tag{2.2}$$

$$\alpha = \begin{cases} \left( \frac{n}{n_{th,*}} \right)^\beta & \text{if } n \geq n_{th,*} \\ \\ 1 & \text{if } n < n_{th,*} \end{cases} \tag{2.3}$$

where $\rho$, $c_s$ and $v_{\rm bulk}$ are the density, sound speed and bulk velocity of the gas particles neighboring the black hole, and $n_{th,*}$ the critical density for star formation. The density dependent boost factor $\alpha$, identical to that of Booth & Schaye (2009), acknowledges that gas with densities $n$ higher than the threshold for star formation $n_{th,*}$ will have unresolved, multi-phase structure. Calibrating against a series of observed black hole scaling relations, the best-fit value for $\beta$ was 2 (Tremmel et al., 2017). Importantly, this definition for the boost factor only takes effect for high density gas. Even at this high resolution, structures below $10^4$ K and at densities higher than $\sim 0.2$ m$_p$/cm$^{-3}$ are unresolved due to the limited mass ($\sim 10^5$ M$_\odot$) and spatial (250 pc) resolution. Gas at such high densities likely has considerable, unresolved multiphase structure that will result in under-predicted accretion rates if unaccounted for.

A key difference from the Bondi model is the introduction of $v_\theta$, the rotational velocity of the gas around the black hole. This explicitly accounts for rotational support against free fall into the black hole. $v_\theta$ is computed as the velocity a parcel of gas would have at one softening length $\epsilon_g$ away from the black hole, if angular momentum from larger scales were conserved. This introduces a coupling between feedback and gas kinematics. When there is little to no coherent rotation measured at these scales, the model reduces to the Bondi rate boosted by the factor from Booth & Schaye (2009).

Energy is continuously fed back into the surrounding gas every black hole timestep as a thermal injection. Each time a particle receives feedback energy from a black hole,

its cooling is shut off for a duration equal to one black hole time step, similar to the blastwave model of Stinson et al. (2006). Black holes and the gas particles around them are placed on the smallest global timestep, typically $\sim 10^4$ yrs, so that the cooling shutoffs are short compared to the local free fall time (3-5Myr) so that thermal properties are more continuously sampled when calculating accretion and feedback. The cooling shutoff aims to address the artificial overcooling resulting from insufficient resolution, and has been shown to produce better convergence in gas properties than other versions of thermal feedback and kinetic/momentum-driven feedback (Smith et al., 2018). In this context, the cooling shutoff, in combination with the very short SMBH timesteps, captures the fact that energy from growing SMBHs is transferred continuously rather than instantaneously. In this implementation, gas properties are able to respond to the transfer of energy before immediately – and unrealistically – radiating that energy away. The result is that this simple feedback prescription is able to drive powerful outflows out to 10s of kpc (Pontzen et al., 2017; Tremmel et al., 2019) in a way that is predictive, rather than a choice explicitly made in the sub-grid model.

The feedback energy is proportional to the accretion rate,

$$E_{FB} = E_r E_f \dot{M}_\bullet c^2 dt, \tag{2.4}$$

where the radiative efficiency $E_r$ is assumed to be 0.1 and the best fit value for $E_f$ was found to be 0.2 (Tremmel et al., 2017). The numerical resolution of RomulusC allows for the injection of thermal energy from SMBH feedback to occur on scales of $\sim$100pc. This is observed to drive outflows on scales of 10s-100s of kpc (Tremmel et al., 2019; Pontzen et al., 2017) with neither explicit large-scale implementations nor momentum injection. This feedback prescription, unlike recent simulations in the literature (Sijacki & Springel, 2005; Dubois et al., 2013; Sijacki et al., 2015; Weinberger et al., 2017; Oppenheimer et al., 2018), does not distinguish between quasar and radio mode at different accretion rates. These simulations distinguish between an inefficient radiative/quasar mode and a more efficient kinetic/radio mode occuring typically for more massive black holes with lower eddington ratios. We choose to keep the feedback prescription simple, since the microphysics of AGN feedback are still poorly understood and are sensitive to parameters like black hole spin and magnetic fields that are beyond current detection methods. Besides producing large-scale outflows, our constant efficiency thermal feedback with a cooling shutoff reproduces scaling relations for galaxies at a range of masses (Tremmel et al., 2017). We refer the reader to §2.2 of Tremmel et al. (2019) for a more detailed discussion.

During the epochs considered in this simulation, the mass of the SMBH in RomulusC doubles from $7 \times 10^9$ to $1.4 \times 10^{10} M_\odot$. The AGN feedback power fluctuates rapidly around a mean total luminosity (assuming 10% radiative efficiency and 2% feedback efficiency) of $\sim 10^{44}$ erg/s while the cluster is isolated and falls to $\sim 2 \times 10^{42}$ erg/s after the merger; and only 2% of the radiation energy couples to heat the gas.

## 2.3 Results

### 2.3.1 The four epochs of cluster dynamics

We consider the cluster at four different epochs shown in Figure 2.1, chosen to represent four important stages of evolution for the brightest cluster galaxy (BCG). The duration of each epoch is $\approx 0.5$Gyr, about twice the dynamical time in the core, so that stochasticity in the AGN activity does not dominate our analysis. The first period (7.3-7.7 Gyr, dark blue) captures the cluster when it is isolated and star-forming. The next epoch (9.2-9.7 Gyr, light blue) is characterized by the BCG actively quenching, coincident with a period of enhanced AGN activity and outflows as discussed in Tremmel et al. (2019). The third epoch (10.8-11.3 Gyr, orange) occurs after the BCG is fully quenched but the cluster is still isolated, and the fourth (12-12.5 Gyr, red) takes place during the first pericenter passage of a merger with a galaxy group, which was approximately one-eighth the mass of the main halo at in-fall. We keep these colors consistent throughout the following analyses.

The left panel shows the evolution of the virial mass of RomulusC over cosmic time. The epochs that we study begin when the cluster progenitor is $\sim 6 \times 10^{13}$ $M_\odot$ in mass. On the right panel, we plot the specific star formation rate (red) and black hole accretion rate (blue) as a function of time. The horizontal dashed lines indicate the accretion rates that correspond to the AGN feedback rates of $10^{44}$ and $10^{45}$ erg/s. The light blue epoch witnesses a decline in specific star formation rate (sSFR) of two orders of magnitude, and the orange epoch encompasses a slight resurgence before the quenching is complete. The red epoch witnesses the quenching of black hole activity. The $r_{500}$ at each of these epochs is 287, 388, 481 and 601 kpc, respectively. The mass of the black hole increases from 8.5 $\times 10^9 M_\odot$ to $1.3 \times 10^{10} M_\odot$, with most of the growth happening before the merger begins at 11.65 Gyr. The emission-weighted $kT_{500}$ ranges from 1.2 to 2.0 keV over this period, before reverting to 1.4 keV at z = 0.

Figure 2.2 shows the column density, mass-weighted temperature, mass-weighted pseudo-entropy $K \equiv k_B T \times n_e^{-\frac{2}{3}}$, and volume-weighted pressure $P \equiv k_B T \times n_g$ along the line of sight through a slice with 10 kpc in thickness during each of these epochs; each image represents a 500 kpc-per-side view of the cluster. The weighting for each quantity is chosen to most closely resemble the observable analogue.

Despite star formation in the BCG declining by over two orders of magnitude, the structure of the ICM remains relatively unchanged until the right-most panel depicting the time of the merger event. Figure 2.3 zooms in on the four snapshots immediately surrounding the first pericenter passage of the merging substructure (now with 300 kpc-per-side). The top three maps clearly show bulk motions of gas, which takes high density, low temperature gas from the core and mixes it with warmer gas at larger radii. The temperature map shows that gas is also heated during the pericenter passage. A shock wave is first seen at 11.97Gyr, and expands and diffuses within a radius of 150kpc by the

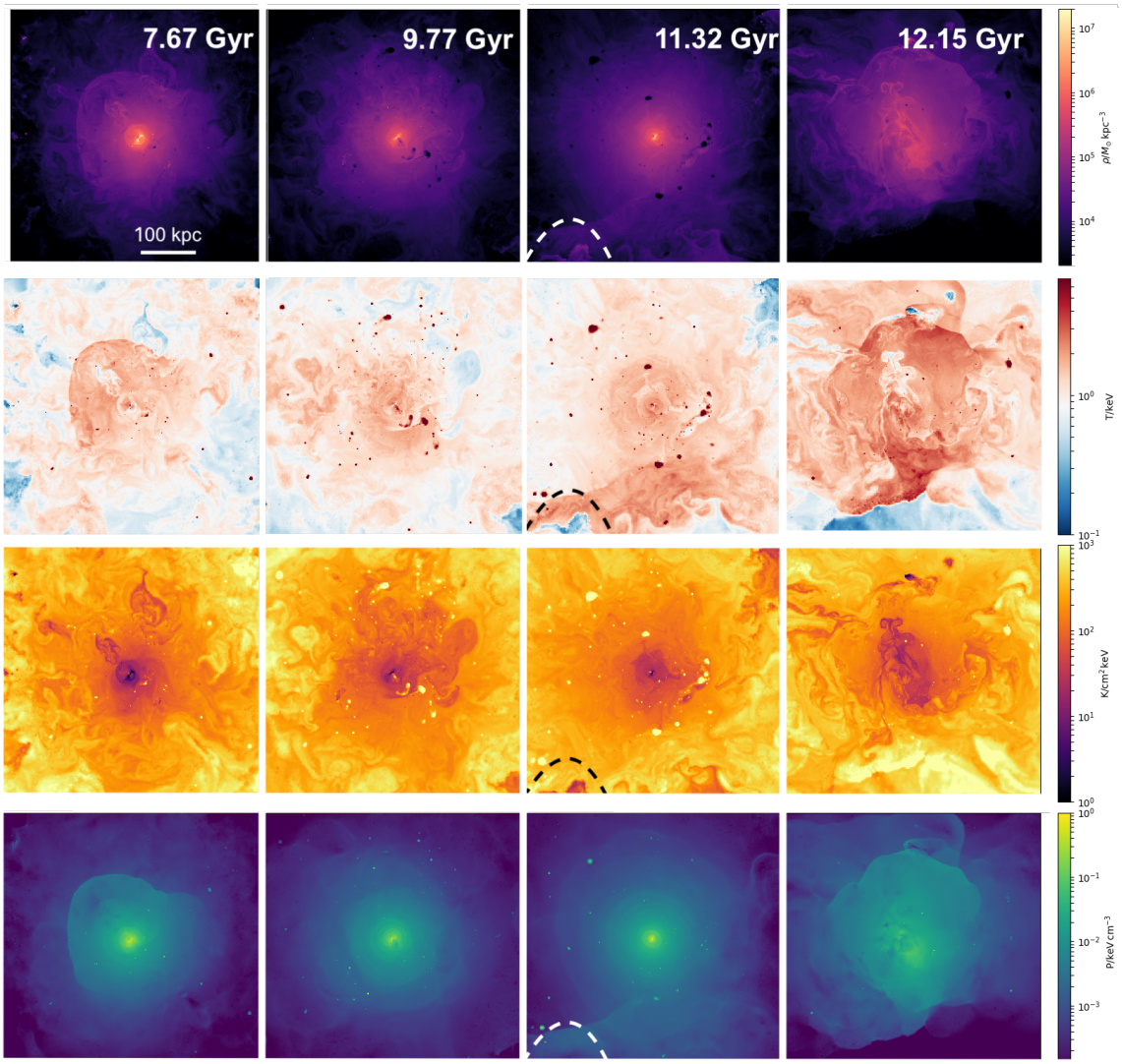


Figure 2.2: From top to bottom: ICM column density, mass-weighted temperature, mass-weighted entropy, and volume-weighted pressure maps through a slice with 10kpc thickness of RomulusC at the four key epochs analyzed in this work: low (*first column*) and high (*second column*) AGN activity before merger, once the central galaxy has been quenched (*third column*) and at the beginning of the merger (*last column*). Each map is 500 kpc a side, projected over 10 kpc along the line of sight. The in-falling substructure, whose northern outskirts are seen to the bottom of the images in the third column, disrupts the ICM structure shortly after it begins to interact with the cluster core ($t = 12.15$ Gyr, fourth column). The core remains in this disrupted state, characterized by a marked decrease in cooling and AGN activity, at least until the end of the simulation 1.65 Gyr later.

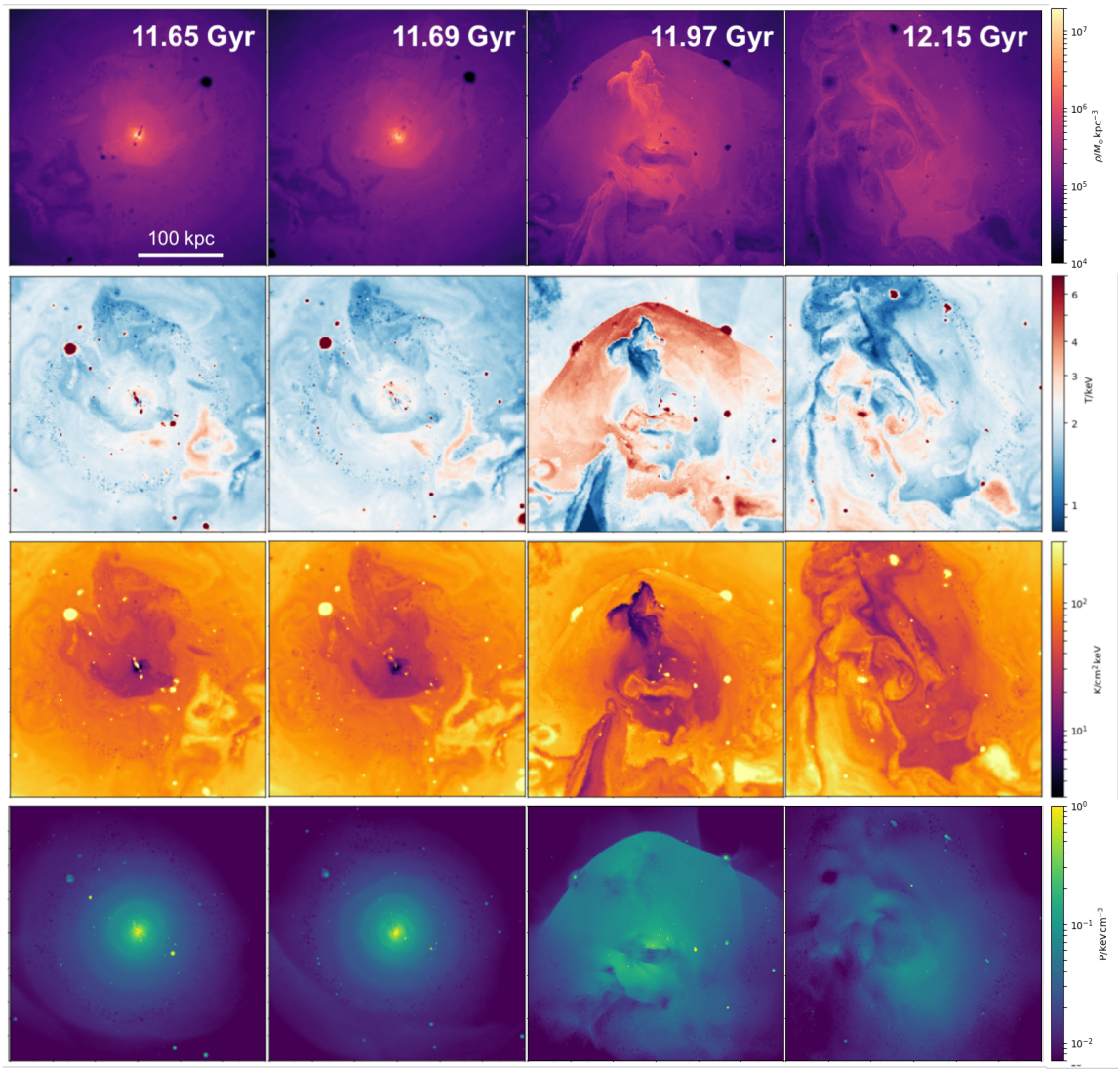


Figure 2.3: Maps of column density, mass-weighted temperature, mass-weighted entropy and volume-weighted pressure through a slice with 10 kpc thickness from the halo center immediately around the disruptive merger event. The shown region is 300kpc in size. The substructure is outside this region in the first two snapshots, punches through the core of the main halo at 11.97 Gyr, creating a high pressure bubble that expands and heats the ICM by 12.15 Gyr. Throughout this time period, AGN activity is 1-2 orders of magnitude lower than when the cluster was isolated, so that it cannot cause the heating.

next snapshot 0.2Gyr later. The disruption of the low entropy core thus occurs not only from removing cool, dense gas from the core and mixing it with less dense, hotter gas from further out, but also by shock heating of the central gas by the merging substructure. This heating channel is also found to be significant in idealised simulations (McCarthy et al., 2004; Poole et al., 2006, 2008).

Figure 2.4 shows profiles for the volume-averaged density, mass-weighted temperature, entropy, and pressure during each of the four epochs discussed above. Similar to observations, entropy and pressure profiles were derived from the mass-weighted temperature and volume-averaged electron number density within a given radial bin. All radial profiles are computed for gas hotter than $10^6$K, corresponding to the temperatures detectable by Chandra ($> 0.1$ keV). We shade the central $0.04\mathrm{R}_{500}$, the largest size of the BCG, which conservatively denotes the area experiencing noisy behavior due to stellar and SMBH feedback processes associated with the BCG. This was estimated by examining the gas content of the simulation (see, e.g., Figure 10 from Tremmel et al. (2019)) for the region dominated by the cold ISM disk. This region encompasses the vast majority of star formation prior to quenching. Within this region there are strong fluctuations due to stellar and black hole feedback processes. These fluctuations are absent in the epoch of merger (indicated in red), where the cold gas disk has been destroyed by the merger. All the profiles are self-similar, i.e., described by gravitational collapse alone (Kaiser, 1986), outside $0.1R_{500}$ ($\sim$60 kpc at z = 0) for all but the earliest epoch, where the cluster seems to still be forming; there, the temperature and entropy profiles are self-similar outside $0.2R_{500}$. Secular processes in the ICM do increase the entropy in $r = (0.1 - 0.3)R_{500}$ over time, but only after the merger is the entropy significantly elevated and flattened within the central $r \lesssim 0.1R_{500}$. To account for the change in background density and temperature expected in the $\sim 5$ Gyr considered here, the density is normalised by the critical density of the Universe at the corresponding redshift; the appropriate normalisation $K_{500}$ was derived in McCarthy et al. (2008), and $T_{500}$ and $P_{500}$ follow simply thereafter.

When the cluster core is isolated and AGN activity is low (dark blue), the entropy profile declines all the way to the central $0.05R_{500}$. A prolonged episode of AGN feedback quenches star formation in the BCG (Tremmel et al., 2019) while slightly increasing entropy at intermediate scales at $r = (0.03 - 0.15)\mathrm{R}_{500}$ (light blue).The profile maintains this form as the BCG gets completely quenched and the AGN activity spikes yet higher in the orange band. Importantly, the gradient of the profile becomes more positive in the light blue epoch compared to the dark blue, and in the orange compared to the light blue. In this latter, fully quenched epoch, the entropy gradient is positive even in the central 10 kpc. Idealised studies (e.g., McCourt et al., 2012; Voit, 2018) have shown that such a positive entropy gradient, along with $t_{\rm cool} >> t_{\rm ff}$, suppresses the condensation of low-entropy gas out of a warm-hot ICM, and we now see the same effect in our cosmological simulation.It is important to note that this inner region of the simulation is dominated by the galaxy and is therefore strongly affected by various feedback processes. Only after the merger (red)

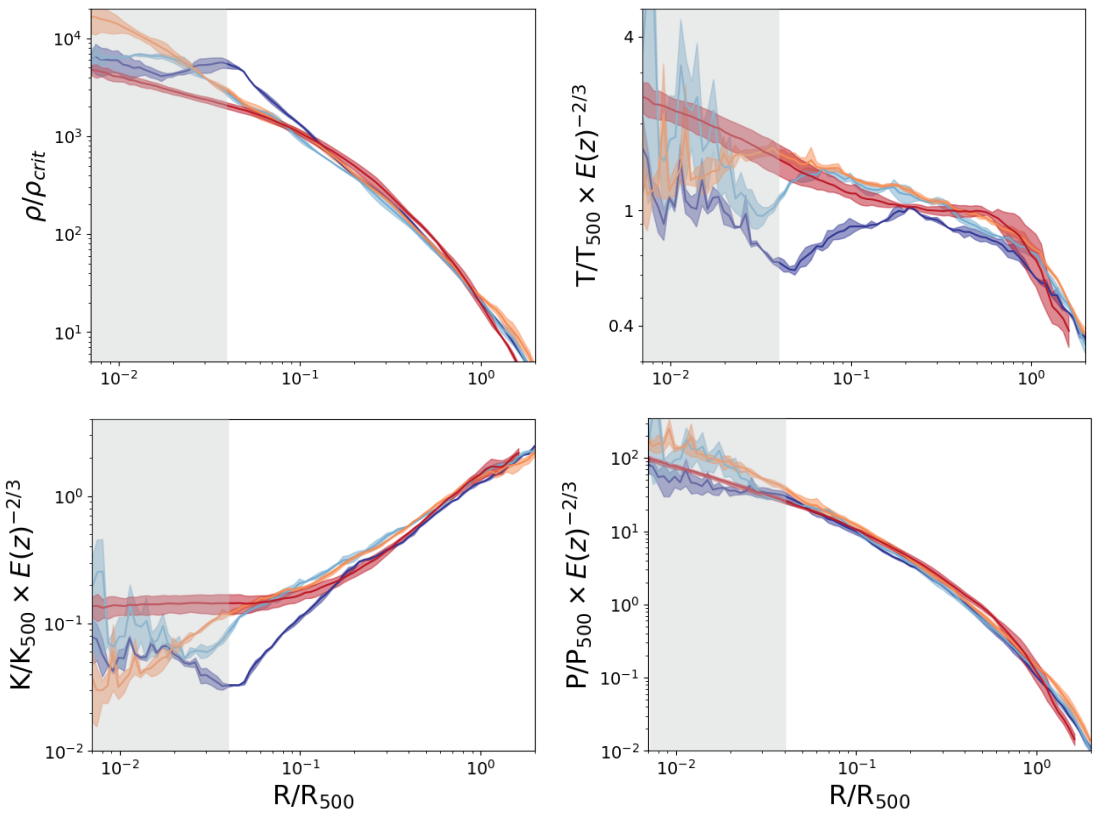


Figure 2.4: Evolution of 3D gas mass density (*top-left*), mass-weighted temperature (*top-right*) and entropy (*bottom-left*), and volume-weighted thermal pressure (*bottom-right*) derived from the volume averaged electron number density and mass-weighted temperature in the ICM. Each color represents each of the four key epochs: before (purple) and after (blue) quenching, between quenching and beginning of the merger (orange), and during the merger (red). All quantities are normalised by the value at $R_{500}$, with the self-similar values for $K_{500}$ and therefore $T_{500}$ derived in McCarthy et al. (2008). Since the quantities fluctuate within each 0.5 Gyr epoch, the solid line shows the mean value and the shaded region shows the 1-$\sigma$ variation. The thermal pressure remains roughly constant throughout, validating its use as a mass proxy regardless of the dynamical state of the cluster.

does the shape of the entropy profile change; it is now flat within $0.1R_{500}$, or 60 kpc at that time.

In the lower right panel of Figure. 2.4, we see that neither the merger nor AGN activity affects the thermal pressure profiles. This is in agreement with observational and theoretical evidence that cluster pressure profiles exhibit a remarkable level of self-similarity (Nagai et al., 2007b; Arnaud et al., 2010) and that its integrated counterpart, the core-corrected Compton Y, ought to be robust mass proxy (Nagai, 2006; Kravtsov et al., 2006; Poole et al., 2007) even in presence of AGN feedback and mergers.

### 2.3.2 AGN feedback and mergers as regulators of gas cooling

Analytical work and idealised simulations have also shown that the infall of cooling gas depends crucially on the shape of the entropy profile. Small fluctuations in entropy create many small pockets of gas that are cooler than their surroundings. These parcels move radially inward, until they reach a region where they match the local entropy (Voit, 2018). If the entropy profile is flat within a certain radius, gas that is cooling at that radius will fall rapidly towards the center. Note that in some of the idealised studies, the fluctuations are seeded by turbulence from AGN (e.g., Prasad et al., 2017, 2018, 2020). In a cosmological cluster, such as ours, the fluctuations are generated by mergers, movements of galaxies within the ICM, and penetrating streams from the cosmic web (e.g., Nagai & Lau, 2011; Nagai et al., 2013; Zhuravleva et al., 2013; Zinger et al., 2016; Lau et al., 2017), in addition to feedback.

Figure 2.5 shows the distribution of entropy of all the gas particles within 500 kpc of the halo centre during each of the four epochs. Each cell in this entropy-radius phase space is colored by the log of the probability density function, which is the gas mass in the cell divided by the total gas mass within 500 kpc. The mass-weighted profile of the hot ($T > 10^6$K) X-ray emitting gas is plotted in purple. Particles that were close to the central SMBH at any recorded snapshot are shown in red. These particles are a subset of those that have received direct thermal energy injection from AGN feedback, since intermediate timesteps are not recorded. We treat these particles instead as tracers of gas that have received feedback more or less directly from the SMBH and these results show that such gas is quickly evacuated to larger radii.

The upper two panels in Figure 2.5 show a significant amount of low-entropy gas within the central 10s of kpc. Although the AGN is active during these epochs, much of the energy imparted by AGN feedback escapes the core of the cluster via collimated outflows (Tremmel et al., 2019), which is why dramatic changes in AGN activity do not affect the central entropy profiles in these isolated phases. By the third (lower-right) panel, as low-entropy gas is gradually extinguished from the core, the BCG is quenched. At this epoch, the central entropy profile increases monotonically with radius, and the dispersion in the central entropy is significantly reduced. Interestingly, this development corresponds

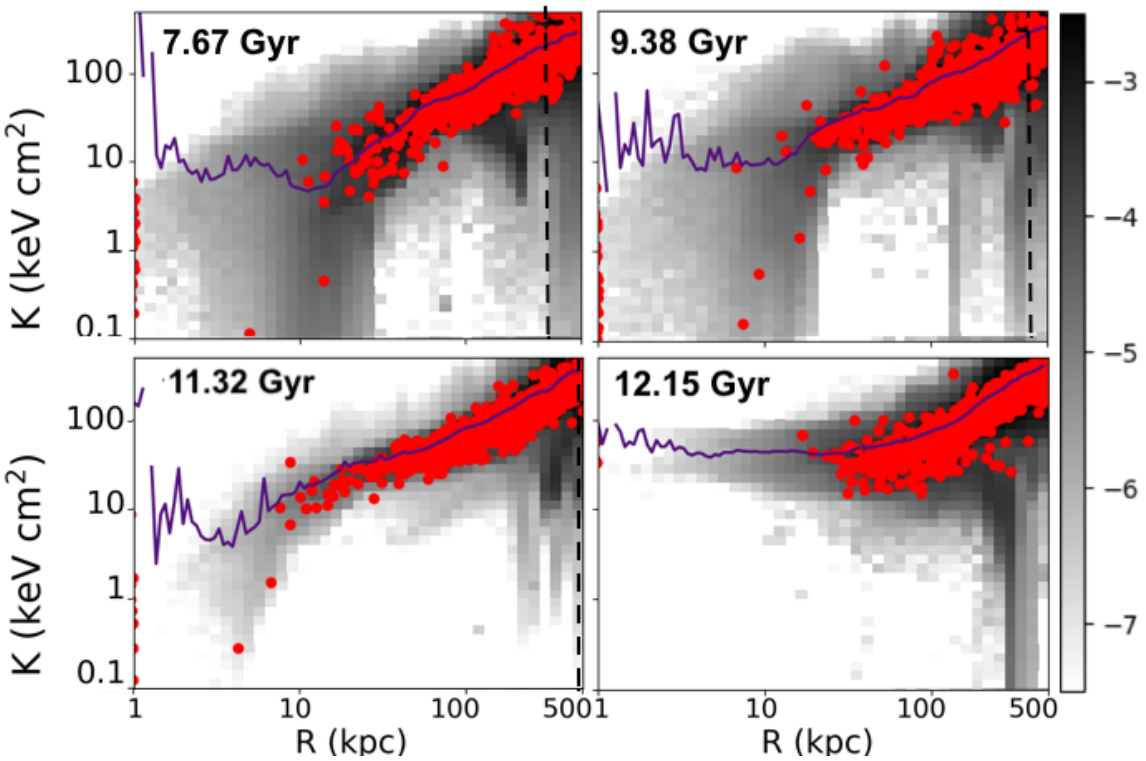


Figure 2.5: The entropy distribution of all the gas particles within 500kpc of the halo centre. The purple line shows the mass-weighted average of the hot ($T > 10^6$K) X-ray emitting gas. Red points represent a subset of the particles that received feedback energy from the AGN any time after $t = 6$Gyr. The colour map is the log of the probability distribution of particles at a given point in the grid. The black vertical dotted lines show $R_{500}$ at the corresponding snapshot; it is outside the depicted region in the last panel. The orange dashed lines indicate the shaded region in the profile plots. AGN heating clearly removes gas from the cluster centre, since the red particles rapidly settle at $r > 30$kpc where their entropy is close to the average profile. However, the entropy in the inner $\sim$30kpc remains low until the merger, with plenty of gas significantly lower in entropy than the average. The merger diminishes the amount of low-entropy gas at all radii, and elevates the core entropy within 1 Gyr of the subshalo entering the virial radius of the main halo.

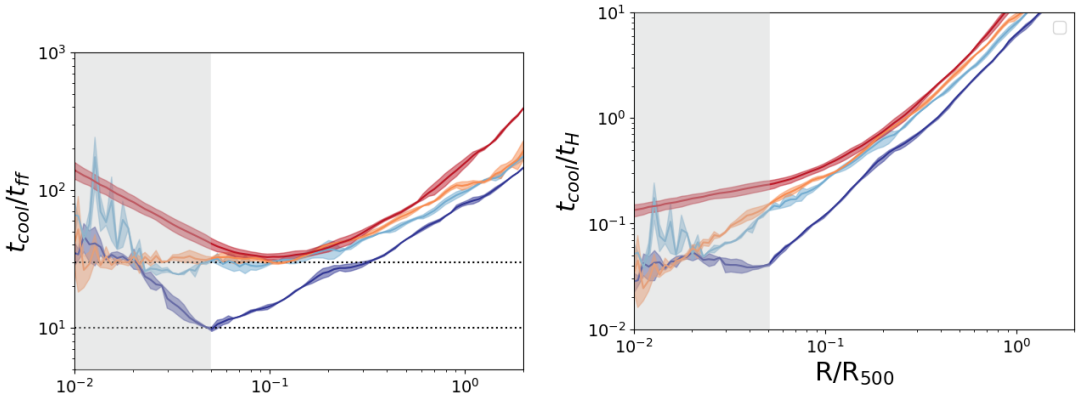


Figure 2.6: *Top panel:* The ratio of cooling time to free-fall time as a function of cluster-centric radius. As in Figure 2.4, the shaded region indicates the extent of the BCG at the earliest epoch; at later times, it is a slightly smaller fraction of $R_{500}$. At early times when the BCG is actively forming stars, the ratio is as low as 10. During the period when AGN activity is quenching star formation and decreasing the amount of cooler gas in the center of the cluster, the ratio hovers around 30. The dashed lines represent the approximate unstable region predicted by theory and supported by observations. AGN feedback is able to increase this ratio to avoid runaway cooling and star formation. *Bottom panel:* The cooling time as a function of cluster-centric radius. The evolution seen in the top panel is due to an increase in the cooling time, particularly within $\sim 0.1 R_{500}$ as well as a steepening of the cooling time evolution with cluster-centric radius. Even as star formation quenches in the BCG, the cooling times are significantly below a Hubble time. While the cooling times are increased by a factor of several during the merger at the end of the simulation, they are still as low as 10% the Hubble time. The on-going merger is a likely source for continued heating at $z = 0$, but this suggests that the low entropy, actively cooling core is likely to reform within a few Gyr following the merger in absence any continued heating source.

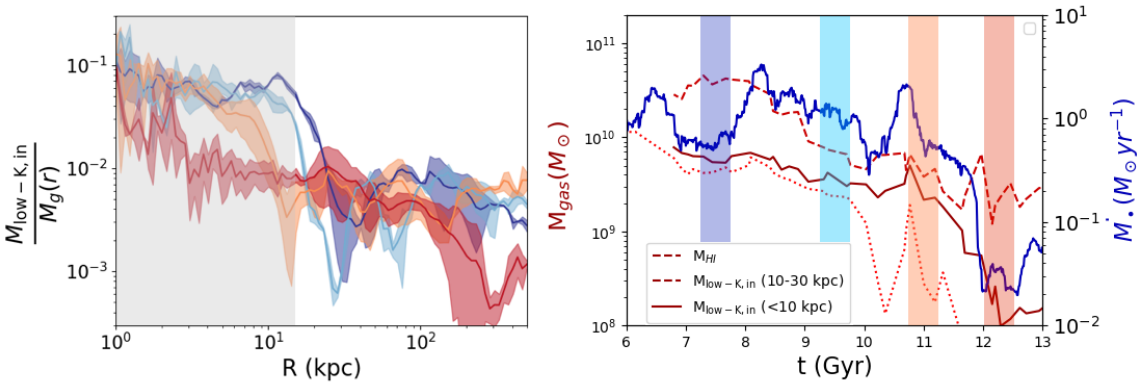


Figure 2.7: *Left panel:* Mass of infalling, cooling gas, normalised by the total gas mass, as a function of radius during the four epochs. The cooling gas is defined as that with entropy one standard deviation less than the mass-weighted average at a given radius; alternate definitions of cooling gas yielded the same qualitative result. Normalising by the total gas mass accounts for changes in the core gas density, seen in Figure 2.4. The cooling gas fraction is about ten times higher in the central 10-15 kpc before the merger than after; the cooling gas mass fraction mononically decreases with radius, confirming that there is less cooling in the outskirts than in the core. *Right panel:* The total amount of infalling cooling gas, i.e., the left panel integrated within the central 10 kpc (solid) and in 10-30kpc (dashed) as a function of time. The dotted line shows the mass of neutral hydrogen (HI, which is explicitly modelled in the simulation) within the central 10kpc, to show that this lower-entropy gas does correlate to our definition of cooling gas. Black hole accretion rate is plotted on the right axis as in Figure 2.8. Consisent with results presented in Tremmel et al. (2019), during the period of AGN activity from $\sim 8-11$ Gyr the amount of lower-entropy gas, as well as neutral hydrogen, in the central regions of the cluster declines, eventually leading to the quenching of star formation while the AGN remains active. The merger event represents a more complete disruption of cooling and extinguishes the AGN activities.

to quenching of star formation in the central galaxy. In the final panel, we see the effect of the merger, which unlike AGN feedback raises the entropy of the X-ray emitting hot phase in the central 100 kpc and eliminates the cold phase entirely. We see in Figure 2.1 that during this phase the central SMBH accretion also decreases by more than an order of magnitude, so it cannot be AGN activity that heated the core.

The difference between panels 3 and 4 is crucial. In the former, the BCG is quenched, the core is running out of cold-phase gas, but the entropy profile of the hot-phase gas is still relatively low in the center. The latter is after the shock heating at 11.97 Gyr, witnessed in Figure 2.3. There is now no gas with entropy lower than 10 $\mathrm{keVcm}^2$ within the central 50 kpc, and the entropy of the hot phase is entirely flat in the central 150 kpc. These are very different dynamical states of the cluster.

Observations and idealised simulations suggest that the gas cooling is regulated by the AGN-ICM feedback loop. Multi-phase structure in the ICM arises naturally when the heating and cooling balance is globally maintained when the ratio $t_{\rm cool}/t_{\rm ff}$ falls in the range $\sim 5-30$ (McCourt et al., 2012; Sharma et al., 2012; Prasad et al., 2015; Voit et al., 2015; Hogan et al., 2017; Pulido et al., 2018). Under such conditions, local density enhancements driven, for example, by turbulent velocity perturbations (c.f., Gaspari et al., 2013; Prasad et al., 2017, 2018, and references therein) are thermally unstable and condense into clouds that then decouple from their surroundings and 'rain' down upon the BCG, driving star formation and powering the central AGN (Gaspari et al., 2013; Prasad et al., 2015, 2017, 2018; Li et al., 2015; Tremblay et al., 2016).

We find that this ratio is indeed important in RomulusC. The top panel of Figure 2.6 shows the ratio of cooling time ($t_{\rm cool}$) to free-fall time ($t_{\rm ff} = \sqrt{2r/g}$). In the first epoch, when AGN feedback is relatively quiet and the BCG is still star forming, the ratio is significantly lower, falling to values as low as $\sim 10$. The subsequent steps, during which the BCG is in the process of quenching and the AGN is active, the ratio hovers around $\sim 30$. This is consistent with the studies above, which see H-$\alpha$ emitting $10^4$K gas, indicative of active cooling (Sanders et al., 2008; McDonald et al., 2010; Fabian et al., 2011), present primarily in groups and clusters with $t_{\rm cool}/t_{\rm ff} \approx 10-30$, marked with the dotted lines in Figure 2.6. We acknowledge that our cooling times are overestimated since we do not include metal line cooling in the simulation. We discuss this caveat further in §4.4. However, the prediction that the transition from star forming to quenching is coincident with a change in the ratio of cooling and free-fall times should be robust to these details.

The bottom panel of Figure 2.6 compares the cooling time to the Hubble time, $\rm t_{\it H}$. Prior to the merger, even when the BCG is actively quenching (light blue and orange profiles), the cooling time is sub-Gyr. The $t_{\rm cool}$ follows a power law profile at all pre-merger epochs, and central cooling time is less than 1 Gyr. Even after the merger, the cooling time is still of order $10\%$ of the Hubble time. The simulation ends before the merger finishes, and it is likely that the continual heating of gas through shocks and turbulent dissipation through sloshing in the core would lead to the re-formation of the original ICM structure over several Gyrs (Poole et al., 2006, 2008).

In order to capture the evolution of gas cooling out of the hot ICM in RomulusC, we define gas as "potentially cooling" if it (i) has lower entropy compared to the mass-weighted mean entropy of gas at its cluster-centric radius, i.e., $K < \left[\bar{K}(r) - \sigma_K(r)\right]$, and (ii) is radially in-falling toward the cluster center, $v_r < 0$. Radial bins with small numbers of gas particles, typically those at the center of the cluster, can have large values for the standard deviation of entropy, $\sigma_K$. When this occurs we consider all in-falling gas with entropy $K < \bar{K}(r)/2$. While not a precise value, as it is difficult to determine *a priori* which gas particles will effectively cool, this provides a rough baseline with which to compare the ICM evolution. In Figure 2.7 we show this profile of in-falling, relatively low entropy gas as a fraction of the total gas at the corresponding radius. This quantity

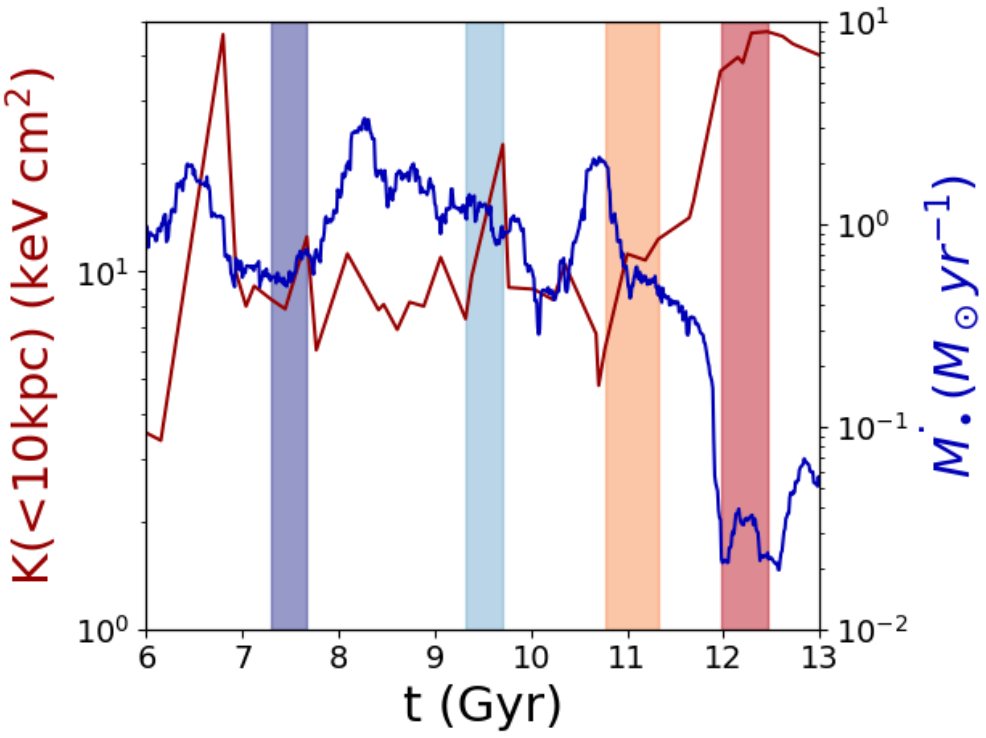


Figure 2.8: Mass-weighted average entropy within the central 10kpc is plotted in red on the left axis, while the black hole accretion rate is plotted in blue on the right axis. The merger at $\sim$ 12 Gyr results in a rapid change in entropy and SMBH activity.

does not change outside 20 kpc at all epochs, consistent with the unchanging entropy and density profiles at scales above $r \gtrsim 0.2R_{500}$ as shown in Figure 2.4. At these scales we are only capturing random gas motions and the natural scatter in entropy. However, within $\sim$10-20 kpc depending on the epoch, while the cluster is isolated, the fraction of cooling gas jumps an order of magnitude higher than in the outskirts. Here in the core the ICM, gas is more susceptible to cooling based on the entropy and $t_{\rm cool}/t_{\rm ff}$ criteria discussed above. This region of enhanced cooling decreases from the star forming, through quenching (light blue) and quenched (orange) epochs. After the merger, however, it disappears entirely. The cooling gas fraction within 10kpc is over five times lower post-merger than in the epoch immediately prior.

On the right-hand panel of Figure 2.7, we show the total mass of such cooling gas within the central 10 kpc (solid red), $r = (10 - 30)$ kpc (dashed red) and HI (dotted red). As the cluster goes from star forming to quenching and then quenched, there is less and less cooler gas (HI, molecular hydrogen, etc.) available in the core for star formation. In the inner 50 kpc of the cluster between $t = 8$ Gyr and $t = 10$ Gyr, where the majority of the quenching takes place, the "potentially cooling" gas mass decreases by $10^{10.3} M_{\odot}$ and stellar mass increases by $10^{10.7} M_{\odot}$. The increased stellar mass more than accounts for this loss of low-entropy gas. Tremmel et al. (2019) discusses in detail the decrease in both sSFR and cooler gas mass around this time. Meanwhile, the accretion rate of the black hole (blue solid) slowly declines as well. Once the merger occurs, accretion onto the black hole, which in practice is fueled by this low-entropy gas in the center, is extinguished. This is in line with observations that find that AGN activity is much more common in clusters with low rather than high central entropy (Edwards et al., 2007; Sun, 2009; Mittal et al., 2009; Hlavacek-Larrondo et al., 2012).

### 2.3.3 Disruption of the ICM structure

Early baryonic simulations suffered from an overcooling problem, where too much cold gas accumulated in the cores of galaxies and galaxy clusters (e.g., Lewis et al. 2000; Nagai et al. 2007b; Borgani et al. 2008; Vazza 2011; Borgani & Kravtsov 2011). Since then, several phenomenological models of AGN feedback have succeeded in producing realistic gas and star formation profiles and galaxy luminosity distributions in cosmological simulations (Brighenti & Mathews, 2006; Sijacki et al., 2007; Vazza et al., 2013; Weinberger et al., 2017), and some are even able to produce fractions of CC/NCC clusters that are in agreement with the observations (Rasia et al., 2015; Hahn et al., 2017; Barnes et al., 2018). Still, a clear sense of how this distribution is established and maintained remains elusive. The high resolution of RomulusC allows us to understand the mechanism of AGN feedback by directly following the outflows launched by it and studying their impacts on the surrounding gas.

We find that a period of enhanced AGN activity is associated with the quenching of star

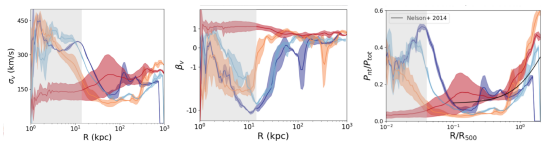


Figure 2.9: *Top panel:* The average one-dimensional velocity dispersion as a function of cluster-centric distance. *Middle panel*: The anisotropy parameter $\beta$ for the motions in the ICM; $\beta$ = 1 for perfectly radial motions, and $\beta = -\infty$ for purely tangential motions. Before the epoch of merger, we now see clearly that the high velocity dispersion in the central 10kpc originates from rotational motions, associated with the BCG gas disk, which lead to a very negative $\beta$. *Bottom panel:* The fraction of non-thermal pressure support for cluster gas compared to the results from Omega500 zoom-in hydrodynamical cosmological simulations of galaxy clusters (Nelson et al., 2014). Rotational motion and AGN outflows result in strong non-thermal support within $r \lesssim 0.1R_{500}$. The merger event disrupts this non-thermal support in the core. Outside $r > 0.1R_{500}$, the non-thermal pressure fraction increases monotonically toward cluster outskirts.

formation (as shown in Figure 2.1) and the lack of cooler gas in the cluster core (as shown in Figure 2.7). Even in this dynamic environment, however, Figure 2.2 shows that the entropy within ∼10kpc remains below 10 $\mathrm{keV\ cm^2}$ until the merger. One reason, as shown in Figure 2.5, is that particles receiving thermal energy from the AGN quickly move out to large radii until they are in equilibrium with their surroundings, instead of dissipating that heat to other gas particles in the core. Furthermore, the energy imparted by the AGN over characteristic cooling times of 10 Myr is $\sim 10^{61}$ ergs, a mere 0.1% of the $10^{64}$ergs required to heat all the gas within the central $0.1R_{500}$ to the post-merger entropy of 100 keV cm$^2$. We note that the AGN at the core of RomulusC is not particularly weak, and at its brightest is comparable to most luminous low-redshift AGN known, which lives in the galaxy cluster MS-0735 (Gitti et al., 2007).

Galaxy cluster mergers generate significant bulk and turbulent gas motions, which in turn can be converted into heating of the ICM through a combination of mixing and turbulent dissipation (Poole et al., 2006, 2008; ZuHone et al., 2010; Zuhone et al., 2011). The top panel of figure 2.9 shows the one-dimensional velocity dispersion of all the gas in RomulusC, assuming an isotropic velocity distribution ($\sigma_v = \sigma_{3D}/\sqrt{3}$). The velocity dispersion decreases significantly in the central ∼20 kpc after the merger, and increases outside of this region. Prior to the merger, this central region is rotationally supported, with large tangential velocities associated with the rotating BCG gas disk. After the merger, this rotational support is disrupted, as are the powerful radial outflows generated by the central SMBH, which also becomes significantly quieter during this epoch.

We verify this explanation of the evolution of the gas dynamics in the core by breaking up the motions into tangential and radial components. The middle panel shows the velocity anisotropy parameter $\beta \equiv 1 - 0.5\sigma_t^2/\sigma_r^2$, where $\sigma_t$ and $\sigma_r$ are the radial and tangential

velocity dispersions, respectively. Note that $\beta = 1$ for purely radial motions, and $\beta \to -\infty$ for purely tangential motions. Outside the central $0.1R_{500}$, before the merger, the velocity dispersion flattens around 100 km/s, consistent with gas motions generated by mergers and movement of galaxy motions through the ICM (e.g., Ruszkowski & Oh, 2011; Nagai et al., 2013). The bump around 100 kpc for the earliest (dark blue) epoch is due to rotational motions. The one-dimensional average velocity dispersion in the central $0.1R_{500}$ of RomulusC is 200-400 km/s. Breaking this down into radial and tangential components, we find that the higher values in the center are dominated by the rotation of the BCG. Outside the core, and at all radii after the merger, the values are consistent with the 150-200 km/s measured by Hitomi in the Perseus cluster (Hitomi Collaboration, Hitomi Collaboration) and numerical simulations (Lau et al., 2017; Bourne & Sijacki, 2017).

Bulk motions of the gas are also a source of pressure support against the gravitational potential of the cluster, in addition to the thermal pressure of the ICM. This non-thermal pressure fraction, $P_{\rm nt}/P_{\rm tot} = \mu m_p \sigma_v^2/(k_B T + m_p \sigma_v^2)$, translates into the deviation from hydrostatic equilibrium, which is a key assumption in mass measurements both from X-ray and SZ observations (e.g., Nagai et al., 2007a; Mahdavi et al., 2008, 2013; Hoekstra et al., 2015; Biffi et al., 2016; Shi et al., 2016; Pearce et al., 2020; Angelinelli et al., 2020). Large-box cosmological simulations to date have found that this non-thermal pressure fraction increases with halo mass, and increases with cluster-centric distance, since mergers and accretion are a major source of this pressure are more frequent in high mass clusters (Lau et al., 2009; Nelson et al., 2014; Shi et al., 2015). Consistent with these results, Mahdavi et al. (2013) find via a joint X-ray and weak lensing analysis of 50 observed galaxy cluster systems that while CC clusters show no evidence of hydrostatic mass bias, NCC clusters exhibit a 15%-20% bias between $R_{2500}$ and $R_{500}$.

The non-thermal pressure fraction for RomulusC is shown as a function of the cluster-centric radius in the bottom panel of Figure 2.9. For comparison, the black line shows the average non-thermal pressure fraction of 65 massive galaxy clusters from the *Omega500* non-radiative simulation (Nelson et al., 2014). The merger does increase the non-thermal pressure support outside $0.1R_{500}$, but within the core ($r \lesssim 0.1R_{500}$) this is actually reduced, since, as described above, the central region was dominated by strong tangential gas motions associated with gaseous disk of the BCG and outflows from the AGN, both of which are disrupted by the merger.

## 2.4 Discussion

### 2.4.1 Comparison with Other Cosmological Simulations

Cosmological simulations of galaxy clusters provide a realistic environment and assembly history within which to study their evolution, self consistently modeling the effects of

both feedback processes, cosmological accretion and sub-structures on the ICM, and BCG evolution. Generally, the major limiting factor of such simulation is the lack of sufficient resolution to resolve all relevant dynamic ranges of this multi-scale, multi-physics problem. A major strength of RomulusC is its resolution, matched only by the TNG50 simulation (Nelson et al., 2019) to date. This is critical for a proper treatment of both feedback processes, as well as to reproduce the distribution of cooler ($T < 10^5 K$) gas in the ICM (Butsky et al., 2019).

The TNG suite implements AGN feedback as an isotropic momentum kick instead of a thermal injection with a local cooling shutoff; in a comparative study of different sub-grid heating models (Smith et al., 2018), these two prescriptions were found to have the best convergence with resolution. The differences due to both the hydrodynamic solver and feedback implementation, however, are expected to decrease at higher resolutions. Indeed, similar to RomulusC, Nelson et al. (2019) find that even though the energy input is isotropic, the outflows are collimated as they follow the path of least resistance perpendicular to the gas disk of the galaxy. They also find that the AGN activity quenches star formation in the late stages of the galaxy's evolution, but continues after star formation is quenched. In the larger box of Illustris-TNG300, Barnes et al. (2018) found that CCs are not more relaxed than NCCs, suggesting that mergers may not be solely responsible for disrupting CCs. This is in contrast to recent works (Rasia et al., 2015; Hahn et al., 2017, e.g.,) that produce realistic CC/NCC fractions and agree with our finding that mergers play a crucial role in increasing and flattening the entropy of cluster cores. This is an interesting discrepancy that should be explored in further work.

### 2.4.2 Relation to Theoretical Models for AGN-regulated Cooling

The evolution of cooling to free-fall time for RomulusC presented in Figure 2.6 shows that our results are broadly consistent with the picture of precipitation-regulated cooling (c.f., Sharma et al., 2012; Gaspari et al., 2013, 2017; Voit et al., 2015; Prasad et al., 2017, 2018). Typical cooling to free-fall time ratios for observed clusters lie in a range $\sim 10-30$ (Hogan et al., 2017; Voit et al., 2018), though values below 10 have been observed (Pulido et al., 2018; Babyk et al., 2018). Ratios below 30 are seen in clusters with significant multiphase gas, whereas values around 30 or above are coincident with ICM that are mostly single phase (Voit et al., 2018). As shown in Figure 2.6, the $t_{\rm cool}/t_{\rm ff}$ ratios in the RomulusC are typically no smaller than 10 and, but the ratios fall well below 30 during the phase with significant cooling and star formation in the core. During the period when the BCG is quenching due to strong, large-scale outflows driven by the AGN (Tremmel et al., 2019) the ratio remains steady at or just below $\sim 30$, consistent with observed clusters with less multiphase gas in their centers.

As shown in Butsky et al. (2019), the ICM of RomulusC contains both the X-ray emitting ($T > 10^6 K$) and the cooler ($T < 10^5 K$) phases. However, despite the state-

of-the-art resolution, the current simulation still lacks the resolution to fully resolve the thermal instabilities. Despite these uncertainties, the fact that we see AGN-regulated gas cooling that quenches star formation with realistic values of $t_{\rm cool}/t_{\rm ff}$ in a fully cosmological simulation is an important result and further supports this theoretical picture of CC clusters.

### 2.4.3 Thermodynamics of the Cluster Core

One of our main conclusions is that AGN activity alone is not capable of significantly increasing the entropy within the entire core region of RomulusC, or completely shutting off cooling. This is in contrast to the results of idealized simulations of AGN feedback in the ICM (e.g., Li et al., 2015; Li et al., 2017), where gas in the core goes through cycles of over- and under-heating by the AGN, corresponding to CC and NCC states of the core gas. There can be two factors at play here. First, these idealised simulations did not have turbulence other than that sourced from the AGN outflows. Gaspari et al. (2013) and Prasad et al. (2017) have shown that the presence of turbulence in the ICM enhances the formation of cold phase gas by 1-2 orders of magnitude. In the absence of this turbulence seeding additional thermal instability at larger radii, such idealised simulations have a much easier time overheating the core, since the core is not replenished as efficiently by inflows. Secondly, few idealised simulations have included a BCG, such as the one that forms in RomulusC. Prasad et al. (2018) found that adding a BCG potential increases the core density and decreases the core entropy, fortifying a CC structure and making it harder to disrupt.

The merger fundamentally disrupts the AGN-ICM equilibrium in at least three key ways. First, it shocks the gas in the core (Poole et al., 2006; McCarthy et al., 2007). We see this as a overpressured core in Figure 2.3, which expands and dissipates by the following snapshot, when the ICM structure is clearly disrupted. Secondly, the impact of the merging event physically removes cooler gas from the core of the main cluster and mixes high-entropy gas from larger radii with low-entropy gas in the core through gas sloshing (Poole et al., 2006, 2008; ZuHone et al., 2010; Zuhone et al., 2011). Third, this sloshing cascades into smaller scale turbulent motions which in turn dissipate into heat (Miniati, 2014; Banerjee & Sharma, 2014; Wittor et al., 2017). It is difficult to assess the relative importance of these processes in a cosmological simulation like RomulusC, because the effects of mergers as well as feedback are highly intertwined. Future work should focus on quantifying the role of each heating channel and its detailed mechanism using idealized simulations, in which each process is added and investigated systematically one at a time.

### 2.4.4 Gas Motions in the Cluster Core

The gas velocities in the center of RomulusC before the merger are larger that those observed in the Perseus cluster using Hitomi (Hitomi Collaboration, Hitomi Collabora-

tion), though Hitomi's spectroscopic measurement of the Perseus alone does not strongly constrain the rotational motions in cluster cores. While large gaseous disks have been observed in the centers of massive halos (e.g. Hamer et al., 2014; Nagai et al., 2019), they are often difficult to detect. Observations of molecular and neutral gas in the center of CC clusters have been observed to have significant rotational velocities (Russell et al., 2019). As the AGN feedback regulates gas cooling on larger scales in RomulusC, the rotationally supported core shrinks by a factor of $\sim 2$, evident from the evolution shown in Figure 2.9.

So far, a rotating disk of cold gas has been resolved in the BCG of the Perseus cluster (Nagai et al., 2019) and Hydra A (Hamer et al., 2014); Hamer et al. (2016) further find kinematic evidence for central rotating disks of cold gas in 2/3 of the galaxy clusters and groups they observed. These disks are extremely difficult to see using only X-ray telescopes, because the hotter gas dominates the luminosity, and current telescopes lack the dynamic range to resolve both the disk and surrounding ICM; furthermore, the response function of current X-ray telescopes falls off sharply below 1keV, and a disk in equilibrium with the BCG potential would be much cooler than this. Such X-ray only observations may be possible with future instruments, such as Lynx (Gaskin et al., 2019), which, in addition to a strong response at low temperatures and a significantly greater dynamic range, would capture X-ray spectra and allow the rotating component to be separated from the quasi-static ICM.

The model for AGN feedback may also affect this structure and the presence of such a rotationally supported disk may be explained by feedback that is too inefficient, potentially supporting the need for variable efficiency similar to two-mode models. Important for our results, the presence of such rotational support likely helps keep the core stable against disruption from the AGN, requiring instead a more catastrophic event like a head-on merger. Differences from other idealized and cosmological simulations already point to a dependence on AGN feedback prescription for the evolution of cluster cores. However, we stress that the result that AGN feedback regulates cooling and star formation while maintaining the cluster's core structure remains important and robust despite these uncertainties. Understanding the effects of different AGN implementations will require further comparison with results from cosmological simulations of similar resolution (e.g., TNG50) as well as a larger sample of high resolution simulations of massive halos.

Finally, RomulusC cannot show that the core heating is permanent, since the simulation ends 2 Gyr after the merger begins. At $r = 0.1R_{500}$ in Figure 2.6, the cooling time is still $\sim 3$ Gyr, so that to check for a permanent transformation, we would have to run the simulation forward another 2-3 Gyr. What we can say is that this one, relative low mass ratio, head-on merger disrupts the cluster core for at least 3 Gyr.

### 2.4.5 Caveats & Future Work

As discussed in Tremmel et al. (2019), and briefly here in §2.1, the ROMULUS simulations do not include the effects of high temperature metal lines, an important coolant in the hot gas of massive halos. This will primarily affect the accretion history of gas onto the central galaxy, though this process is affected by the details of stellar and AGN feedback implementations as well (van de Voort et al., 2011a,b). Were we to have included metal line cooling, gas feeding star formation and SMBH activity at later times might have cooled sooner which would affect when quenching takes place as well as the physical state of the ICM at the time of the merger. However, we stress that even without metal line cooling, the cooling times in the core of ROMULUSC prior to the merger are sub-Gyr (Figure 2.6), meaning that this alone cannot explain the regulation of cooling and that additional heating from both AGN and the merger event is required to regulate and quench star formation. Still, the presence of additional cooling processes may affect the detailed evolution of the $t_{\rm cool}/t_{\rm ff}$ ratio. The relative evolution of this ratio within the framework of this simulation and its coincidence with the onset of quenching remains an important prediction in agreement with both theoretical models and observations. It is likely that different cooling models, as with different feedback recipes, will result in different star formation and SMBH growth histories, as well as different $t_{\rm cool}/t_{\rm ff}$ ratios. Higher resolution simulations capable of resolving molecular gas and metal line cooling are still needed to make more accurate predictions, though such simulations will still be sensitive to *ad hoc* choices in AGN feedback prescriptions. While more advanced simulations are needed to make more detailed predictions, the fact that AGN feedback is capable of regulating gas cooling on large scales without disrupting the ICM core structure is an important proof of concept, along with the connection between quenching and $t_{\rm cool}/t_{\rm ff}$.

The details of AGN feedback are highly uncertain given that all of the relevant micro-physics are unresolved at even the high resolution of ROMULUSC. The choice to include only thermal feedback with a cooling shutoff (see §2.2.2) means that the large-scale kinetic feedback that we observe in the simulation is driven by hot, buoyant gas, which may be different if kinetic feedback were implemented directly. Simulations which implement a 'two-mode' feedback prescription (e.g., Weinberger et al., 2017) will generally change the feedback efficiency for black holes of different mass. In ROMULUSC our black hole feedback prescription assumes a constant proportionality with accretion rate, meaning that high accretion rates are required for strong feedback to occur. Since this efficiency was optimized to produce broadly realistic galaxies (Tremmel et al., 2017), changing AGN feedback efficiency within uncertainties (i.e., without significantly disturbing the galaxy properties) will likely alter the detailed star formation and SMBH growth histories of the BCG. However, our results regarding AGN feedback and its ability to regulate large-scale cooling should be insensitive to the details of the model, as our sub-grid physics affects gas at 100s pc scales while our results pertain to 10s-100 kpc scales in the simulation.

Further, RomulusC does not include the effects of magnetic fields or cosmic rays, which have been shown to play an important role in transfering feedback energy into the ICM. Ruszkowski & Oh (2010), for example, showed that in the presence of tangled magnetic fields, as expected in a turbulent ICM, thermal conduction from the hot outskirts to the core can be significant. Enßlin et al. (2011) showed similarly that their simulated CC structure was weakened by cosmic rays. Each of these would make it easier to form a high, flat-entropy core using AGN activity alone, since the core would never get as cold and dense as in their absence (e.g., Nulsen, 1982; Sarazin, 2004; Mcnamara & Nulsen, 2007, for a review). The role of each of these physical processes is currently being explored by idealised simulations (e.g., Ruszkowski et al., 2007; Sharma et al., 2009; Parrish et al., 2009; Enßlin et al., 2011; Parrish et al., 2012; ZuHone et al., 2013; Kannan et al., 2016; Yang & Reynolds, 2016). Further testing of the effects of different feedback mechanisms will be important. The results of this paper should be seen as a proof-of-concept that it is possible to regulate cooling and star formation with large-scale AGN feedback without disrupting the dense core structure in the ICM.

## 2.5 Conclusions

Using the RomulusC high resolution cosmological simulation of a $10^{14}$ $M_{\odot}$ galaxy cluster we study the relative roles of AGN feedback and major mergers in regulating star formation and determining the structure of the ICM. With its unprecedented resolution, RomulusC produces gas particles as cool as $10^4 K$ (Butsky et al., 2019) and naturally produce large-scale collimated outflows from AGN that are able to quench star formation without significantly changing the structure of the ICM (Tremmel et al., 2019). The simulation also undergoes a merger event at $z \sim 0.14$ that is still on-going at $z = 0$, which, in contrast with AGN feedback, results in a significant change to the ICM structure and cooling efficiency. In this work we focus on understanding in more detail how AGN feedback is able to regulate star formation in the BCG while co-existing with a low entropy ICM core and contrast this with the effect of the merger event. In order to do this, we examine the simulation within four time bins representing different phases of evolution: 1) BCG is star forming, 2) BCG is actively quenching, 3) the BCG is fully quenched, and 4) onset of the merger event. We find that:

1. AGN feedback is able to quench star formation by reducing gas cooling at $\sim$ 10-30 kpc scales and steepen the entropy profile while co-existing with a low entropy cluster core and without disrupting the structure of the ICM.

2. A ratio $t_{\rm cool}/t_{\rm ff} \sim 30$ represents a critical transition between a rapidly cooling cluster core with a star-forming BCG and more moderate cooling with a quenching/quenched

BCG, consistent with both theory and observations. The exact value of this threshold may change upon inclusion of metal line cooling in our model.

3. Gas particles are heated directly by the AGN rise buoyantly to radii $> 30$kpc on short timescales, so that their much of their heat is dissipated on larger scales.

4. A head-on, 1:8 merger is highly disruptive to the ICM struture, resulting in a sudden increase and flattening of the core entropy and a marked decline in AGN activity by 1-2 orders of magnitude.

5. Cooling times in the core during the merger are of order $10\%$ the Hubble time. While energy dissipated from the on-going merger actively prevents this cooling through $z = 0$ it is likely that the core will relax again shortly after the completion of the merger.

This work demonstrates that AGN feedback can regulate cooling within cluster cores without disrupting the structure of the inner ICM. This is in contrast with a massive, head-on merger which does significantly disrupt, at least for a few Gyr, both the ICM structure and the regulating loop between AGN and gas cooling.

Prior to its disruption by the merger, the gas within the low entropy core of the simulated cluster showed strong rotational support. Such disks have been detected in 10-20$\%$ of systems via cold molecular gas, and have only been observed in two systems in X-ray; these could provide stability to cluster cores. Future X-ray spectroscopic missions such as Athena and Lynx may reveal the warm-hot component of rotating gaseous disk around BCG. The merger quickly destroys this rotational structure.

Ultimately, RomulusC is a simulation of a single cluster, and a complete comparison to observations will require simulations of a larger sample of galaxy clusters. A significantly larger volume with similar resolution is hard to achieve given current computational constraints. A promising alternative lies in the genetic modification (GM) technique of Roth et al. (2016), which would allow us to systematically vary individual merger parameters such as mass ratio, impact parameter, and infall velocity, in a controlled fashion currently restricted to idealised simulations.

# Chapter 3

# Constraining Merging Galaxy Clusters with X-ray and Lensing Simulations & Observations: The case of Abell 2146

*U. Chadayammuri, J. A. ZuHone, P.E.J. Nulsen, S. Felix, D. Nagai, F. Andrade-Santos, L. King, H. Russell*

[1]Chandra X-ray Center, Smithsonian Astrophysical Observatory, 60 Garden Street, Cambridge, MA 02143, USA
[2]Department of Physics, Yale University, 52 Hillhouse Ave, New Haven, CT 06511, USA
[3]Department of Physics, University of Texas - Dallas, Richardson, TX 75080, USA
[4]School of Physics and Astronomy, University of Nottingham, Nottingham NG7 2RD, UK

**Accepted to MNRAS Sep 10, 2021**

## Abstract

Galaxy cluster mergers are a powerful laboratory for testing cosmological and astrophysical models. However, interpreting individual merging clusters depends crucially on their merger configuration, defined by the masses, velocities, impact parameters, and orientation of the merger axis with respect to the plane of the sky. In this work, we investigate the impact of merger parameters on the X-ray emitting intracluster medium and gravitational lensing maps using a suite of idealised simulations of binary cluster mergers performed using the GAMER-2 code. As a test case, we focus on modeling the Bullet Cluster-like merging system Abell 2146, in which deep *Chandra* X-ray and lensing observations revealed prominent merger shocks as well as the mass distribution and substructures associated with this merging cluster. We identify the most interesting parameter combinations,

and evaluate the effects of various parameters on the properties of merger shocks observed by deep *Chandra* and lensing observations. We show that due to gravitational compression of the cluster halos during the merger, previous mass estimates from weak lensing are too high. The plane of the merger is tilted further from the plane of the sky than estimated previously, up to $30^\circ$ from the plane of the sky. We discuss the applicability of our results to multi-wavelength observations of merging galaxy clusters and their use as probes of cosmology and plasma physics.

## 3.1 Introduction

Merging galaxy clusters are powerful astrophysical laboratories for studying cosmology and astrophysics. To date, merging galaxy clusters have provided unique constraints on the nature of dark matter (Markevitch et al., 2004; Clowe et al., 2006; Massey et al., 2015; Harvey et al., 2015; Massey et al., 2018) and on the plasma physics of the X-ray emitting intracluster medium (ICM; see Markevitch & Vikhlinin, 2007; Zuhone & Roediger, 2016, for reviews). Mergers are crucial to the hierarchical formation of galaxy clusters, and the frequency of mergers with different mass ratios depends on cosmology (Lacey & Cole, 1993; Fakhouri et al., 2010). Spatial offsets between the collisionless stars, dissipative gas, and lensing mass in merging systems like the Bullet Cluster provide constraints on the cross-section of self-interaction of the dark matter (Randall et al., 2008; Kahlhoefer et al., 2014; Kim et al., 2017; Robertson et al., 2017; Tulin & Yu, 2018, for a review). Shocks and cold fronts are also used to derive unique constraints on the microphysics of the ICM, such as the rate of electron-proton equilibration (Rudd & Nagai, 2009; Avestruz et al., 2015; Wang et al., 2018), thermal conduction (Markevitch et al., 2003; ZuHone et al., 2013), and viscosity (Roediger et al., 2013; ZuHone et al., 2015a; Schmidt et al., 2017); each of these in turn constrains the properties of cosmic magnetic fields (see e.g., Brunetti & Jones, 2014, for a review).

Cosmological simulations yield distributions for the merger speed and dark matter concentrations of the halos (Neto et al., 2007; Duffy et al., 2008), which in turn provide priors for dynamical parameters for merging clusters. However, interpreting specific observed features associated with merging clusters is particularly challenging, because (a) the initial merger and structural parameters are unknown and (b) the systems are not in equilibrium (Golovich et al., 2016, 2017; Wittman et al., 2018). Understanding and controlling the effects of these parameters are crucial for using merging galaxy clusters as probes of cosmology and plasma physics.

Idealised simulations enable powerful, controlled experiments to explore the large space spanned by the cluster merger parameters as well as non-gravitational processes operating during the cluster formation and evolution (Ricker & Sarazin, 2001; Ritchie & Thomas, 2002; Poole et al., 2006; ZuHone, 2011). For example, the halo masses, infall velocity and

impact parameter largely determine the curvatures and Mach numbers of the shocks. The observed features also depend critically on the direction from which the merging cluster is viewed. Pre-shock gas temperatures depend on the masses of the two substructures, as well as their initial gas profiles. The strength of a merger shock depends on the velocity of the perturbing subcluster core through the ICM of the primary cluster, and on the time, or merger phase, at which the system is observed (Zhang et al., 2019, 2020). Furthermore, the observed strength of a shock and the curvature of the shock front both decrease as our viewing direction deviates from the normal to the plane of the merger. Due to the large number of parameters and potential degeneracies between them, they cannot be determined analytically. It is necessary to explore the multi-dimensional parameter space with tailored simulations.

In this work, we use simulations to understand one of the best-observed merging galaxy clusters in the X-ray. The ICM of Abell 2146 was first observed with the *Chandra* X-ray Telescope in 2009 (Russell et al., 2010). This observation revealed some of the clearest merger shocks since the Bullet Cluster (Markevitch et al., 2002). Being less massive and thus cooler than the Bullet Cluster, the gas in Abell 2146 radiates in an energy range where the effective area of *Chandra* is higher, so that surface brightness and temperature can be mapped in unprecedented detail. Constraints on the mass ratio $R = M_2 : M_1$ of the system have been made in previous work using weak lensing and galaxy velocities (King et al., 2016; White et al., 2015), one projection angle was inferred from the line-of-sight velocity separation between galaxies in different subclusters, and infall velocities and time since pericentre passage have been estimated from the positions and Mach numbers of the two shocks in the X-ray (Russell et al., 2012).

In order to determine the parameters of the merger in Abell 2146, we perform a suite of idealised simulations of binary cluster mergers using the GPU-accelerated adaptive mesh refinement code GAMER-2 (Schive et al., 2018). We use the most quickly evolving observables to narrow down the times at which simulated mergers best match Abell 2146, and then assess the effects of the remaining parameters and viewing direction on the observable X-ray and lensing properties of the simulated clusters.

We describe the simulation setup and translation to observable quantities in §4.2. We present observational constraints from X-ray and lensing observations of A2146 in §3.3. We describe the parameter tests, concluding with best fit parameters for Abell 2146 in §4.3, discuss caveats in §3.5 and close with conclusions in §4.6. Throughout this paper we use the flat Planck Collaboration et al. (2016) cosmology with $H_0 = 67.7\,\mathrm{km\,s^{-1}\,Mpc^{-1}}$ and $\Omega_\mathrm{m} = 0.307$. At the redshift of Abell 2146, $z = 0.2323$, this corresponds to an angular scale of $3.823\,\mathrm{kpc/arcsec}$.

## 3.2 Simulations

The simulations were run with GAMER-2 (Schive et al., 2018), a GPU-accelerated Adaptive MEsh Refinement code. The GPU acceleration allows us to simultaneously explore the effect of an unprecedented number of distinct parameters. For this initial study, we use $\sim 25$ million dark matter particles, and use four levels of refinement to achieve a hydrodynamic resolution of 6.8 kpc. Each run takes 5 hours on the Nvidia Tesla K80 GPU nodes on the Grace cluster at the Yale High Performance Computing centre. The present suite of simulations models the dark matter and non-radiative gas. Here, we describe the initial conditions and set up of the merger simulations.

### 3.2.1 Dark matter and gas profiles

We model the initial dark matter distribution of a cluster with the "super-NFW" profile:

$$\rho(r) = \frac{3M}{16\pi a^3} \frac{1}{(r/a) \times (1 + r/a)^{5/2}} \tag{3.1}$$

where the scale radius is related to the half-mass radius as $a = R_e/5.478$ (Lilley et al., 2018). This form has a finite total mass, which makes it preferable to the NFW profile for ensuring a smooth cutoff of the DM density at large radii. sNFW properties are related to those of the more widely used NFW profile as follows. The scale radius $r_{sc}$ of a halo is defined as the radius where the logarithmic slope of the density profile is $d\log\rho/d\log r = -2$, and the concentration is defined as $c_{\rm NFW} = r_v/r_{sc}$, where $r_v$ is the virial radius. For NFW halos, Duffy et al. (2008) measured the concentration-mass relation:

$$c_{\rm NFW} = 5.74 \times \left(\frac{M}{2 \times 10^{12} h^{-1} M_\odot}\right)^{-0.097}, \tag{3.2}$$

where the distribution in $c_{\rm NFW}$ at fixed $M$ is log-normal and the standard deviation of $\log_{10} c_{\rm NFW}$ is 0.14. For the sNFW profile, $r_{sc} = 2a/3$ so that the concentration is $c_{sNFW} = r_v/r_s = 3r_v/2a$. Fitting sNFW profiles with NFW formulae, Lilley et al. (2018) find that the concentrations in the two models are well-described by a linear fit, $c_{sNFW} = 1.36 + 0.76 c_{\rm NFW}$. Therefore, given an NFW concentration, we find the equivalent sNFW concentration, which then yields the scale radius $a$.

The gas is initially set up to be in hydrostatic equilibrium with the dark matter. This criterion alone, however, is insufficient to yield both temperature and density profiles. We therefore model the gas density with the modified beta profile of Vikhlinin et al. (2006), which, along with the condition of hydrostatic equilibrium, gives the temperature. These

profiles have the form

$$n_p n_e = n_0^2 \frac{(r/r_c)^{-\alpha}}{(1+r^2/r_c^2)^{3\beta-\alpha/2}} \frac{1}{(1+r^\gamma/r_s^\gamma)^{\epsilon/\gamma}} \tag{3.3}$$

where $n_e$ and $n_p$ are the number densities of electrons and protons, respectively. The inner density slope $\alpha$ and the core radius $r_c$ control the strength and extent of the cool core. The scale radius of the gas density, $r_s$, is independent from the sNFW scale radius $a$. At intermediate radii the slope of the density profile, in log-log space, is - $3\beta$, and outside $r_s$ it transitions to -($3\beta$ + $\epsilon$/2) over a length scale determined by $\gamma$. Once the total mass profile is set, the dark matter particles are given velocities that place them in virial equilibrium, using the procedure outlined in Kazantzidis et al. (2004), where the energy distribution function is calculated via the Eddington formula (Eddington, 1916):

$$\mathcal{F}(\mathcal{E}) = \frac{1}{\sqrt{8}\pi^2} \left[ \int_0^{\mathcal{E}} \frac{d^2\rho}{d\Psi^2} \frac{d\Psi}{\sqrt{\mathcal{E}-\Psi}} + \frac{1}{\sqrt{\mathcal{E}}} \left( \frac{d\rho}{d\Psi} \right)_{\Psi=0} \right] \tag{3.4}$$

where $\Psi = -\Phi$ is the relative potential and $\mathcal{E} = \Psi - \frac{1}{2}v^2$ is the relative energy of the particle. We compute this distribution function and use it to determine DM particle speeds using the acceptance-rejection method. The direction of each particle's velocity is determined by choosing random unit vectors in $\Re^3$. The gas cell velocities are zero, i.e., the system is in hydrostatic equilibrium.

In §3.4.6, we explain how $r_c$ was chosen to roughly match observations of relaxed cluster profiles. Since this study focuses on merger shocks, we do not vary the model parameters $r_s/a$, $\gamma$ or $\epsilon$, which affect the gas distribution on large scales. These would likely be relevant if the merger were more evolved and the shocks much further out, or in modeling a system with accretion shocks. Both these scenarios are outside the scope of the current work. We adopt $\beta$ = 2/3, $\gamma$ = 3 and $\epsilon$ = 3, which were found to fit all the observed clusters in the Vikhlinin et al. (2006) sample, and set $r_s = a$.

### 3.2.2 Merger geometry

The merger evolution and observed properties depend on the impact parameter $b$ and relative velocity $v$—their product $L$ is the specific angular momentum of the subhalo. Initially,the primary halo sits on the $x$-axis and has a speed $v/2$ in the positive $x$ direction. The centre of the subhalo is located in the $x$–$y$ plane at $y = b$, with its $x$ coordinate chosen to make the distance between the two centres 3 Mpc, comparable to the sum of the virial radii. The subhalo is set in motion at speed $v/2$ in the negative $x$ direction. This is shown schematically in Fig. 3.1.

For two halo masses $M_1$ and $M_2$, the approximate infall velocity can be analytically estimated by considering the turnaround radius $d_0$ where the relative radial velocity is 0,

as shown in (Sarazin, 2002):

$$d_0 \simeq 4.5 \text{ Mpc} \times \left(\frac{M_1 + M_2}{10^{15} M_\odot}\right)^{1/3} \times \left(\frac{t_{\rm merge}}{10^{10} \text{ yr}}\right)^{2/3} \tag{3.5}$$

$$v \simeq 2930 \text{ km/s} \left(\frac{M_1 + M_2}{10^{15} M_\odot}\right)^{1/2} \left(\frac{d}{1 \text{ Mpc}}\right)^{-1/2} \left[\frac{1 - \frac{d}{d_0}}{1 - (\frac{b}{d_0})^2}\right]^{1/2} \tag{3.6}$$

where $d$ is the separation between the halo centres at the beginning of the simulation, $b$ is the impact parameter, and $t_{\rm merge}$ is the age of the Universe at the time of the merger. Since Abell 2146 is observed at z = 0.2323 and is close to pericentre passage, we use $t_{\rm merge} = 10.8$ Gyr. The infall velocity, on average, then ranges from 720 - 1220 km/s for the range of halo masses explored.

Neither the infall velocity nor the impact parameter is directly observable post-merger, and the separations and velocities they do produce are observed in projection. Assuming that the two BCGs in the field trace the potential minima of the two clusters, White et al. (2015) constrained the merger plane to be tilted 13-19° from the plane of the sky. The observed shock velocity, 2200 km/s for the bow shock, is higher than the initial velocities, since the halos and the gas in them accelerate under gravity; this point was crucial in the interpretation of the Bullet Cluster, which was otherwise considered an anomaly within ΛCDM (Springel & Farrar, 2007; Lage & Farrar, 2015). The X-ray observations suggest a small, non-zero impact parameter (Russell et al., 2010), but cannot constrain it directly. We test a range of values from 50-700 kpc and assess how it affects the X-ray features.

To summarise, the initial cluster velocities are along the $x$-axis, the impact parameter along the $y$-axis, and the default line-of-sight is the $z$-axis, (0, 0, 1). If the viewing direction is defined by the polar and azimuthal angles ($\theta$, $\phi$), images we see will be projections of the simulation box along the normal

$$\mathbf{n} = [\sin\theta \cdot \cos\phi, \sin\theta \cdot \sin\phi, \cos\theta]. \tag{3.7}$$

Thus, if the 3D separation between the halo centres is $\mathbf{d}$ and their 3D relative velocity is $\mathbf{v}$, the observed separation and relative line-of-sight velocity are given by $d_{\rm proj} = \sqrt{\mathbf{d}^2 - (\mathbf{d} \cdot \mathbf{n})^2}$ and $v_{\rm los} = -\mathbf{v} \cdot \mathbf{n}$.

## 3.3 Constraining Cluster Merger Models using X-ray and Lensing Observations

In this work, we focus on modeling multi-wavelength observations of Abell 2146, consisting of X-ray observations (Russell et al., 2010; Russell et al., 2012), spectroscopic data on the bright galaxies (White et al., 2015), and strong+weak lensing measurements (King

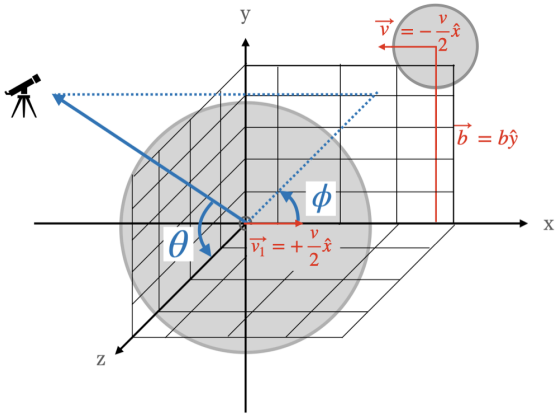


Figure 3.1: Schematic of initial configuration. The relative velocity between the subclusters is in the x direction, with an initial impact parameter $b$ along the y direction; the merger thus occurs in the $x-y$ plane. The observer is in the direction of the telescope, so that the viewing direction is determined by the polar angle $\theta$ and the azimuthal angle $\phi$.

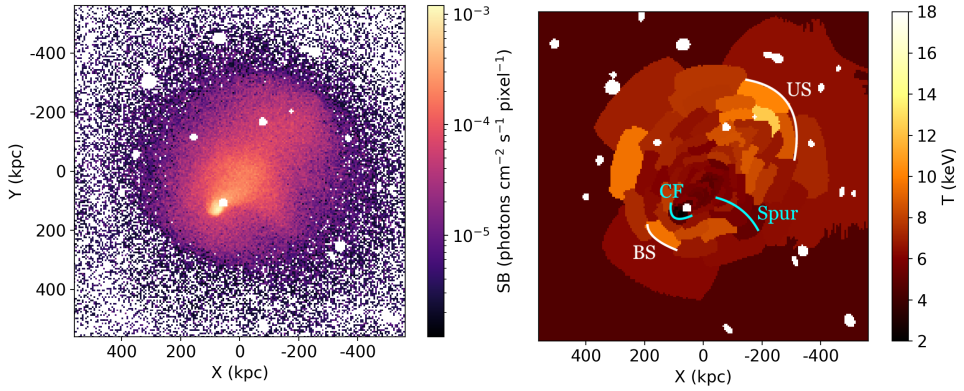


Figure 3.2: X-ray surface brightness (left) and temperature (right) maps of Abell 2146, reproduced from the *Chandra* archive. The BCGs A2146-A and A2146-B identified and used in optical and lensing studies are marked as white crosses on the surface brightness map. The bow shock and upstream shock are highlighted in white, and the cold front and plume in blue, on the temperature map. The black areas in the surface brightness and corresponding white areas in the temperature map are where bright point sources were masked.

et al., 2016; Coleman et al., 2017). The details of each observation can be found in the corresponding papers. Below, we highlight the salient features of these observations that are relevant to the merger and structural parameters of A2146. The quantitative constraints are summarised in Table 3.1.

### 3.3.1 The *Chandra* data

We use the 419.5 ks of ACIS observations of A2146 from the *Chandra* archive. The data were reduced using the `chav` software package[1] with `CIAO v4.6` (Fruscione et al., 2006), following the processing described in Vikhlinin et al. (2005) and applying the `CALDB v4.7.6` calibration files. The X-ray surface brightness map has a resolution of 1", corresponding to 3.7 kpc at the cluster redshift $z_c$ = 0.2323. The temperature maps are coarser, since it is necessary to bin several pixels together to get enough photons to fit a spectrum. Therefore, we use the surface brightness maps to identify sharp features in the ICM, and then infer from the temperature maps whether they are shock or cold fronts.

#### Shock fronts

A shock is an abrupt increase in both temperature and density occurring when a perturber - in this case, the infalling subcluster - moves through an ambient medium, creating and propagating a compressive disturbance. Unlike in an adiabatially compressed region, the entropy in a shock is increased.Abell 2146 features two of these - a bow shock with a Mach number $\mathcal{M} = 2.3 \pm 0.2$, and an upstream shock of $\mathcal{M} = 2.1 \pm 0.1$ (Russell et al., 2012, Russell et al. in prep.). The two have slightly different formation channels, and reproducing both simultaneously is a strong constraint on our simulations. As elaborated in §3.3.2, the merger produces other shocks too, although these are too weak to be detected by current X-ray telescopes.

Bow shocks form in front of the perturber, with the leading edge perpendicular to its direction of motion. The upstream shock is a reverse shock that forms ahead of the centre of the primary cluster. As the subcluster falls in, its halo gas is impeded by the ICM of the primary cluster and slows down. Gas stripped from around the leading edge of the merging subcluster forms an obstacle to the gas falling in its wake. The resulting pressure disturbance travelling into the wake then develops into a shock propagating upstream into the wake. We note that this shock is distinct from the leading shock that propagates away from the initial contact discontinuity through the subcluster.

The bow shock forms first, followed shortly by the upstream shock. For each shock, the Rankine-Hugoniot jump conditions yield the Mach number, which along with the distance travelled provides an estimate of the age of the shock. Russell et al. (2012) used this method to place the system at 0.1-0.3 Gyr post pericentre passage. The relation between the shock

[1] `http://hea-www.harvard.edu/~alexey/CHAV/`

strength and age, however, is non-trivial for realistic cases where the perturber is not a rigid object, but rather a diffuse cluster that gets stripped and deformed over time (Zhang et al., 2019). The distance between the two shocks evolves rapidly following pericentre passage. This is therefore our preferred indicator of dynamical stage.

In the optically thin ICM, a shock front only appears as a sharp feature where it is nearly tangent to our lines-of-sight. What we observe is the projection of the emission per unit volume along the line-of-sight. A shock front generally curves away from the direction of propagation. Sight lines outside the shock intersect only unshocked gas. Sight lines inside the shock intersect some shocked gas, and the depth of the shocked gas increases as the line moves further inside the front. The abrupt edge is due to the depth of the sight line within the shocked gas varying with distance, $x$, behind the front as $\sqrt{x}$, for small $x$. Only the component of the gas velocity perpendicular to the shock front is affected by the shock, so that the shock is generally strongest at its leading edge and weakens towards the periphery of the curved shock front, where the front is inclined to its direction of motion. As a result, the standoff distance between the shock and the cold front marking the boundary of the remnant gas core is smallest at the leading edge of the shock and increases towards the periphery. This causes the observed standoff distance to depend on viewing direction, increasing as our lines-of-sight tilt away from the normal to the plane of the merger (see Markevitch & Vikhlinin, 2007, for a more detailed review of these effects).

The preshock temperature for the bow shock is close to the initial temperature of the gas at the appropriate radius in the primary cluster. The potential minimum of the primary cluster, like its observed BCG, lie within the upstream shock. The pre-shock temperature of the upstream shock, on the other hand, is that of high entropy gas from the outskirts of the subcluster, which has been subject to substantial adiabatic compression as it flowed into the central region of the primary cluster.

The strength of the bow shock depends on the movement of the perturber (i.e., the substructure core) through the ICM. This depends on the initial velocity, as well as on its gravitational acceleration due to the masses of the two halos, which in turn is larger if the impact parameter is lower. For the upstream shock, the velocity difference is between the gas stripped from the leading edge of the substructure, and the rapidly infalling gas from its outskirts.

Given the above considerations, constraints on initial velocity, masses, impact parameter and projection angles can only be inferred once the correct snapshot, i.e., dynamical phase, has been identified. Since the shock separation is the most rapidly evolving observable, we use that to select suitable snapshots.

### Cold fronts

Unlike shock fronts, cold fronts are discontinuities where the temperature decreases as the density increases; in merging clusters, these are usually the remnants of cool cores

Table 3.1: Summary of observed constraints for Abell 2146.

| | |
|---|---|
| $\mathrm{M}^{\dagger}_{\mathrm{tot,lens}}$ | 1.01 - 1.36 $\times 10^{15} M_{\odot}$ |
| $d^{*,1}_{\mathrm{BS-US}}$ | 700 kpc |
| $\mathrm{d}^{*,2}_{\mathrm{BS-CF}}$ | 140 kpc |
| $(T_f, T_i)^{*,3}_{\mathrm{BS}}$ | (10, 5) keV |
| $(T_f, T_i)^{4}_{\mathrm{US}}$ | (12, 6) keV |
| $\Delta v^{\ddagger}_{rel}$ | 763 km $\mathrm{s}^{-1}$ |

† King et al. (2016)
* Russell et al. (2012)
‡ White et al. (2015)
[1] Shock separation, i.e., distance between the points of maximum curvature of the bow and upstream shocks.
[2] Standoff distance, i.e., distance between points of maximum curvature of the bow shock and cold front.
[3] Pre- and post-shock temperature for the bow shock.
[4] Pre- and post-shock temperature for the upstream shock, from Russell et al. in prep.

(Markevitch & Vikhlinin, 2007). If the merger were perfectly head on, the two cores would strongly disrupt, so that any cool core remnants feature would be very spread out. Furthermore, the two disrupting cores would be elongated along the same axis, that of the merger.Abell 2146 has an obvious cold front associated with BCG-A, a bullet-like subcluster punching through the ICM of the larger primary cluster, and a second, less striking discontinuity perpendicular to the axis between the shocks. These two are highlighted with blue curves in the temperature map of Fig. 3.2. The second feature has been called the "plume" in the X-ray observations, which also suggested that this is most likely the disrupted gas core of the primary halo (Russell et al., 2012). Such a configuration of cold features requires a non-zero impact parameter. If the impact parameter is too large, the substructure remnant will curve significantly towards the merger axis and towards the primary core, but never pass through any part of it directly. The two cool cores would thus be left relatively intact. Thus we can constrain the impact parameter using the brightness, width, and relative orientation of the two cold features.

### 3.3.2 The origin of observable merger features

Fig. 4.1 shows snapshots illustrating the development of the observed features. These have been described in detail in Roettiger et al. (1996, 1997); Takizawa (2005); Poole et al. (2006). Here, we present a brief summary to develop physical intuitions into the effects of the explored parameters. Illustrative snapshots are shown in Fig. 4.1. In the first panel, we see that as the subcluster falls in from the right, high entropy-gas from

the outskirts of the two clusters is compressed into a high-temperature region around the contact discontinuity. This is enveloped by an extended, weakly shocked region. The centre of the subcluster, and therefore its BCG, originally lies outside this shocked region, but accelerates toward the shocked region as the rightward shock moves towards it, so that it eventually enters the shocked region. The subhalo core overtakes and passes through the initial contact discontinuity, and drives a shock behind the leftward moving shock. This is seen as the yellow-white, hottest region in the middle temperature panel. As the subcluster core undergoes pericentre passage, these two shocks connect, creating the appearance of prominent bulge near the centre of the large-scale front. This bulge is the feature identified as the bow shock in the observations. The pre-shock temperature ahead of this bow shock is that of the ICM of the primary halo. There is a second contact discontinuity between the cool core of the subcluster and the shocked ICM of the primary cluster, which is the cool core of the subcluster being elongated by ram pressure; this is what Poole et al. (2006) call a 'comet-like tail', and is seen in both the Bullet Cluster (Markevitch et al., 2002) and Abell 2146. Some gas stripped from the remnant subcluster core obstructs higher velocity gas falling to the left, in the wake of the subhalo, leading to the formation of the upstream shock, seen clearly in the third panel. The pre-shock gas here is from the outskirts of the subcluster, so that it has a relatively high entropy and adiabatic compression heats it well above its initial temperature. The core of the primary cluster is disrupted; this low entropy gas gets ejected perpendicular to the cold front from the subcluster core, forming the feature called a plume by Poole et al. (2006).

Eventually, the subcluster core turns around, whereas the shocks continue to move outwards. In our simulations, as in Poole et al. (2006), this happens $\sim$1 Gyr after the first pericentre passage. However, the shocks at this point are too weak and extended to be comparable to systems like Abell 2146. Therefore, we focus on what can be learned from mergers in the first 0.5 Gyr after pericentre passage, while their morphology resembles that of Abell 2146 and the Bullet Cluster.

We treat the brightest cluster galaxies (BCGs) as tracers of the gravitational potential minima of the two merging clusters. The optical observations, used to determine positions and velocities of the BCGs, have *Hubble*'s diffraction-limited resolution of 0.05" or $\sim$0.18 kpc. Spectroscopic data is available for 63 of the brightest galaxies in the clusters (White et al., 2015), which yields line of sight velocities with uncertainties of less than $1\%$. We note that BCGs do not generally lie exactly at the potential minima of their host clusters, especially not in the midst of a merger. The relation between the BCG and cluster core velocities, therefore, is significantly less precise.

There is a clear BCG in the bullet-like cold front, referred to in the literature as BCG-A and treated as the BCG of the primary cluster referred to as Abell 2146-A (e.g., Canning et al., 2012; White et al., 2015; King et al., 2016; Coleman et al., 2017). These studies have assumed that the second brightest galaxy in the field, shown in the left panel of Fig. 3.2 near the upstream shock, is the BCG of the secondary cluster; this has been called

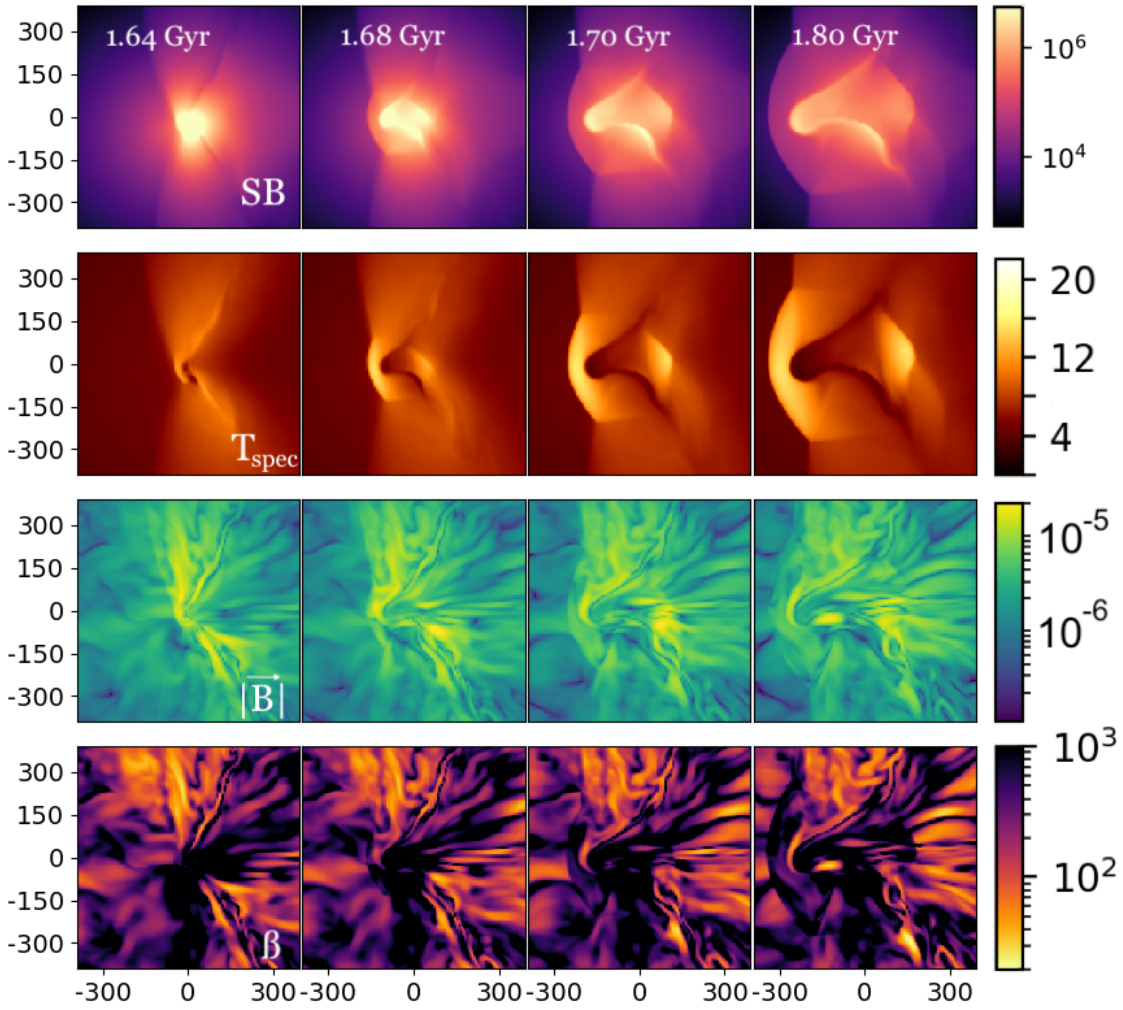


Figure 3.3: Snapshots of the surface brightness (top) and Mazzotta-weighted projected temperature (bottom) maps around the pericentre passage of the subcluster through the primary cluster, illustrating the development of the observed X-ray features. The first panel shows the initial contact discontinuity (i.e., a cold front), surrounded by one weak shock traveling towards the left and another towards the right. Pericentre passage occurs just before the middle panel, and the substructure core here creates an additional bow shock and contact discontinuity. By the final panel, subcluster gas that had been swept upstream by ram pressure meets gas that is still infalling, creating the upstream shock. The remnant of the primary cluster core is ejected almost perpendicular to the axis between the bow and upstream shocks, and is called the "plume" in observations.

BCG-B. Instead, our simulations consistently show that BCG-A must be associated with the secondary cluster, and BCG-B with the primary cluster, in order to reproduce the X-ray features.

### 3.3.3 Mass Profiles from Lensing Data

Weak lensing maps offer complementary constraints on the total mass and mass profiles of Abell 2146. These rely on measurements of the distortion of shapes of background galaxies in deep imaging with the *Hubble Space Telescope (HST)* (King et al., 2016). The observed ellipticity of a background galaxy ($\epsilon$) depends on the intrinsic ellipticity ($\epsilon_i$), as well as the (complex) reduced shear from the the cluster lens ($g$):

$$\epsilon = \epsilon_i + g = \epsilon_i + \frac{\gamma}{1-\kappa}\,, \tag{3.8}$$

where $\gamma$ and $\kappa$ are the (complex) cluster shear ($\gamma \equiv \gamma_1 + i\gamma_2$) and convergence, respectively. The convergence is given by $\kappa = \Sigma/\Sigma_{cr}$, where $\Sigma$ is the surface mass density of the lens, and $\Sigma_{cr}$ is the critical surface mass density

$$\Sigma_{cr} = \frac{c_v^2 D_s}{4\pi G D_{ds} D_d}\,, \tag{3.9}$$

which depends on the angular diameter distances to the source $D_s$, to the lens $D_d$, and between the two, $D_{ds}$. The speed of light is denoted by $c_v$. $\kappa$ and $\gamma$ depend on the second derivatives of the lensing potential $\psi$:

$$\kappa = \frac{1}{2}\left(\psi_{,11} + \psi_{,22}\right) \tag{3.10}$$

and

$$\gamma_1 = \frac{1}{2}\left(\psi_{,11} - \psi_{,22}\right) \tag{3.11}$$

$$\gamma_2 = \psi_{,12}. \tag{3.12}$$

In the weak lensing regime, $\kappa \ll 1$ and $|\gamma| \ll 1$.

A strong lensing analysis of the multiple images shows that the mass peaks at the brightest galaxy in the bullet-like cold front, BCG-A (Coleman et al., 2017). The parametric models considered in the weak lensing analysis had NFW components centred on the BCGs A and B, simultaneously fit to the lensing reduced shear data (ellipticities of the distant galaxies) (King et al., 2016). The free parameters were the two cluster radii $r_{200}$ or, equivalently, masses enclosed inside $r_{200}$, $M_{200}$. The field-of-view of the data ($\sim$750 kpc at the system redshift) is not sufficient to simultaneously fit the cluster concentrations and masses. Therefore, the concentrations of the two clusters were fixed for each parametric

fit, and were set to be equal to one another and in the range expected from the cluster mass-concentration relationship (Duffy et al., 2008). For $c = 4$, the total virial mass of the clusters is $M_{200} = 1.2 \times 10^{15} M_{\odot}$, and their mass ratio is $\approx 4$. The total mass is about $10\%$ bigger for $c = 3.5$ and $10\%$ smaller for $c = 4.5$. In the weak lensing analysis, Abell 2146-A, centred on BCG-A, is the more massive cluster. Instead, our simulations suggest the opposite to be the case - the deeper potential minimum, associated with the primary cluster, resides in the upstream shock, like the observed BCG-B.

In order to fit projected mass density profiles to the simulation data, or obtain synthetic shear maps, we must project the total 3D mass in the simulation boxes along the line of sight to obtain $\Sigma$ or $\kappa$. Assuming that the gravitating mass profile of each cluster is well described by the NFW model (Navarro et al., 1996), we can then simultaneously fit projected NFW profiles (Łokas & Mamon, 2001) centred on the two potential minima to the projected mass using

$$\Sigma(R) = \frac{c^2}{2\pi} g(c) \frac{M_v}{r_v^2} \cdot \frac{1 - \mid c^2 \tilde{R}^2 - 1 \mid^{-1/2} C^{-1} \left[ \frac{1}{c\tilde{R}} \right]}{c^2 \tilde{R}^2 - 1}, \tag{3.13}$$

where $c = c_{\rm NFW}$, $\tilde{R} = R/r_v$, $R$ is the projected distance from the centre and

$$g(c) = \frac{1}{\ln(1+c) - \frac{c}{1+c}},$$
$$C^{-1}(x) = \begin{cases} \cos^{-1}(x), & \text{if } R > r_s \\ \cosh^{-1}(x), & \text{if } R < r_s. \end{cases}$$

Roediger & Zuhone (2012) have shown that the observed mass of a subcluster within a given radius can vary dramatically over the course of a merger (though they only examined a single simulation with a large impact parameter). The gravitational potential deepens, and includes the mass of both systems near pericentre, so that during pericentre passage the measured concentration would be substantially larger than pre-merger. When the system eventually virialises again with the combined mass of the two halos, the total concentration is lower than pre-merger, consistent with the concentration-mass relation.

There is a degeneracy between mass and concentration in weak lensing observations, such that assuming a lower concentration requires a higher mass to produce the same convergence $\kappa$. Furthermore, lensing observations do not sample the full density field - rather, they provide local measurements of the reduced shear $\gamma/(1-\kappa)$ at the positions of background galaxies. For Abell 2146, King et al. (2016) had $\sim$1500 such shape measurements. The limited number of galaxies per radial bin combines with the shape noise, i.e. inherent dispersion in the unlensed distribution of shapes for the background galaxies, to restrict the signal-to-noise ratio. Lastly, as noted above, the field of view of the HST observations did not extend to the outskirts of the cluster system. As a result,

it was unfeasible to simultaneously fit the dark matter concentration and total mass/virial radius of each cluster. Therefore, the lensing analysis focused on a range of concentrations $3.5 \leq c_{\rm NFW} \leq 4.5$, motivated by the concentration-mass relation (e.g., Duffy et al., 2008), and then fit the virial radius for each $c_{\rm NFW}$. These masses are 50-100$\%$ higher than those from X-ray and SZ observations.

The concentrations of merging halos, however, are systematically different from those of their relaxed counterparts. We found that initial concentrations of $3 < c_{\rm NFW} < 6$ for either halo, a range broader than the 1-$\sigma$ scatter in the $c-M$ relationships at cluster masses, was consistent with the X-ray observations. We then created maps of the projected density at 10 snapshots around the one that best fit the X-ray observations, capturing the 0.2 Gyr centred on core passage. At each snapshot, the projected density was sampled at $\approx$ 60,000 points and projected NFW density profiles were simultaneously fit to this sampling using least-squares minimization of the difference in $\kappa$ between the simulation and model. The results of these fits are shown in the top panel of Fig. 3.4, where the initial values were $c_1 = c_2 = 5$ (corresponding to clusters referred to as Abell 2146-B and Abell 2146-A respectively in the lensing papers). Assuming that a spherically symmetric NFW profile is a good description for the haloes even this close to core passage, the best-fit $c_{\rm NFW}$ is biased high, particularly for the less massive subcluster. Consistent with the results of Roediger & Zuhone (2012), $c_{\rm NFW}$ peaks at pericentre passage and then decreases over time. Even 0.1 Gyr after pericentre passage, the fit concentrations are $20\%$ higher than the initial values.

To illustrate and quantify the mass error due to the assumption of particular concentration values when fitting parameterised lens models, we created shear maps using a Fast Fourier Transform (FFT), and lensed synthetic background galaxy populations with galaxy number density set to match the observed $HST$ field. As was done in the lensing papers, we assume different values for $c_{\rm NFW}$ and fit only for the virial mass $M_{200}$. The upper panel of Fig. 3.5 shows the results for haloes of mass $M_1 = 5.0 \times 10^{14} M_\odot$ and $M_2 = 1.6 \times 10^{14} M_\odot$ and concentrations $c_1 = c_2 = 5$. Fit distributions are shown when $c = 3$ is assumed for each halo. Results for the lower (higher) mass halo are shown in orange (blue), with a vertical line indicating the true mass. To demonstrate the impact of adopting a particular concentration, the bottom panel shows the results of such a lensing forward model for a halo mass $M = 1.6 \times 10^{14} M_\odot$ and $c = 5.0$, i.e., the best fit initial NFW parameters for the less massive subcluster. For 100 different realizations of background galaxy positions and ellipticities, the orange, green and red curves show the distributions of the fit mass $M_{200}$ assuming $c = 3$, $c = 4$ and $c = 5$ while fitting respectively.

Note that assuming concentrations lower than the true value biases mass high. During model fitting, as noted above, King et al. (2016) focused on concentrations in the range $(3.5 - 4.5)$ for the clusters in the system, and correspondingly obtained a higher mass, $(1.0-1.3) \times 10^{15} M_\odot$ than would have been obtained when adopting higher concentrations, which is consistent with our analysis. However, as noted in King et al. (2016), in order for

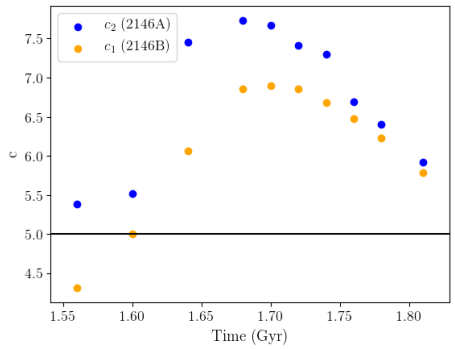


Figure 3.4: The evolution with time of the dark matter concentration parameter for NFW haloes fit to the simulated projected (dark matter) density. In this case, the clusters have initial true total masses $M_1 = 5 \times 10^{14} M_\odot$ and $M_2 = 1.6 \times 10^{14} M_\odot$ and concentrations $c_1 = c_2 = 5$ respectively as indicated by the horizontal line.

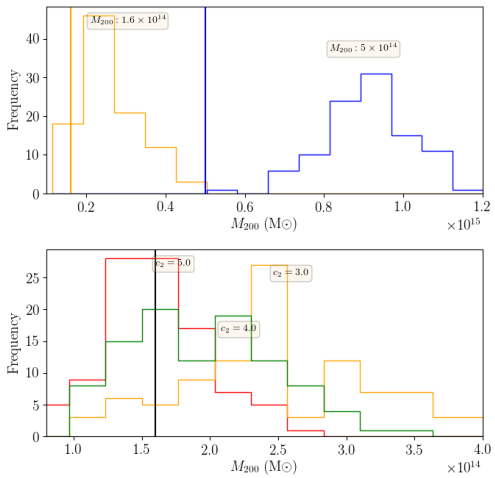


Figure 3.5: Upper panel: The distribution of masses for NFW haloes fit to synthetic lensing catalogues, generated using haloes with true masses $M_1 = 5.0 \times 10^{14} M_\odot$ and $M_2 = 1.6 \times 10^{14} M_\odot$ and concentrations $c_1 = c_2 = 5$. Fit distributions are shown when $c = 3$ is assumed for each halo. Results for the lower (higher) mass halo are shown in orange (blue), with a vertical line indicating the true mass. The masses are overestimated by $\sim 50\%$ for the less massive halo, and $\sim 85\%$ for the more massive halo. Lower panel: The distribution of masses for NFW haloes fit to synthetic lensing catalogues, generated using a halo with $M_2 = 1.6 \times 10^{14} M_\odot$, $c_2 = 5$. Fit distributions are shown when $c_2 = 3$ (orange), $c_2 = 4$ (green) and $c_2 = 5$ (red) are assumed. The true halo mass is indicated with a black vertical line.

| Observable | Simulated Analogue |
|---|---|
| Surface brightness | Emission-weighted projected photon emissivity in 0.3-7 keV |
| Temperature | Mazzotta-weighted projected temperature |
| Lensing | Projected density map |
| Galaxy spectra | Average velocity of dark matter particles in 50 kpc radius (BCG) or 1 Mpc (cluster average) |

Table 3.2: Summary of the simulated analogues to observed quantities

the lensing data to yield a mass for Abell 2146-A similar to that of Abell 2146-B, Abell 2146-A would have to have $c_1 \sim 9$ when $c_2 \sim 3.5$ for Abell 2146-B.

A key lesson from this exercise is that lensing masses, especially from parametric reconstruction, are degenerate with the assumed concentrations. Ideally, there would be sufficient signal-to-noise and field-of-view in the lensing data to constrain both simultaneously. But this is very rare in space-based lensing observations. Instead, the robust, model-independent quantity from lensing surveys is the reduced shear measured from the distant galaxy ellipticities. Comparisons between cluster mass model parameters from simulations and from observations must therefore be made by forward modeling the simulations and fitting their shear maps to the same parametric mass models, under the same observational conditions, such as field-of-view, galaxy number density available for shear measurements etc.

The simulated analogs to observable quantities are summarised in Table 3.2.

## 3.4 Results

The primary goal of this work is to investigate how the observed properties of A2146 depend on the parameters of the simulation. To this end, we compare simulations where all parameters are held constant except the one in consideration, and choose snapshots where the shock separation meets this observed constraint. For all sections but that on the viewing direction in §3.4.2, the system is viewed along the $z$ axis, perpendicular to the plane of the orbit.

### 3.4.1 Initial Cluster Merger Setup

Since the mass ratio of this merger derived from weak lensing has a large uncertainty due to the restricted field-of-view and the necessity to assume concentration parameters, we constrained this parameter by examining simulations from the Galaxy Cluster Merger Catalog (ZuHone et al., 2018).[2] This allows us to inspect mock observations of quantities

[2]http://gcmc.hub.yt

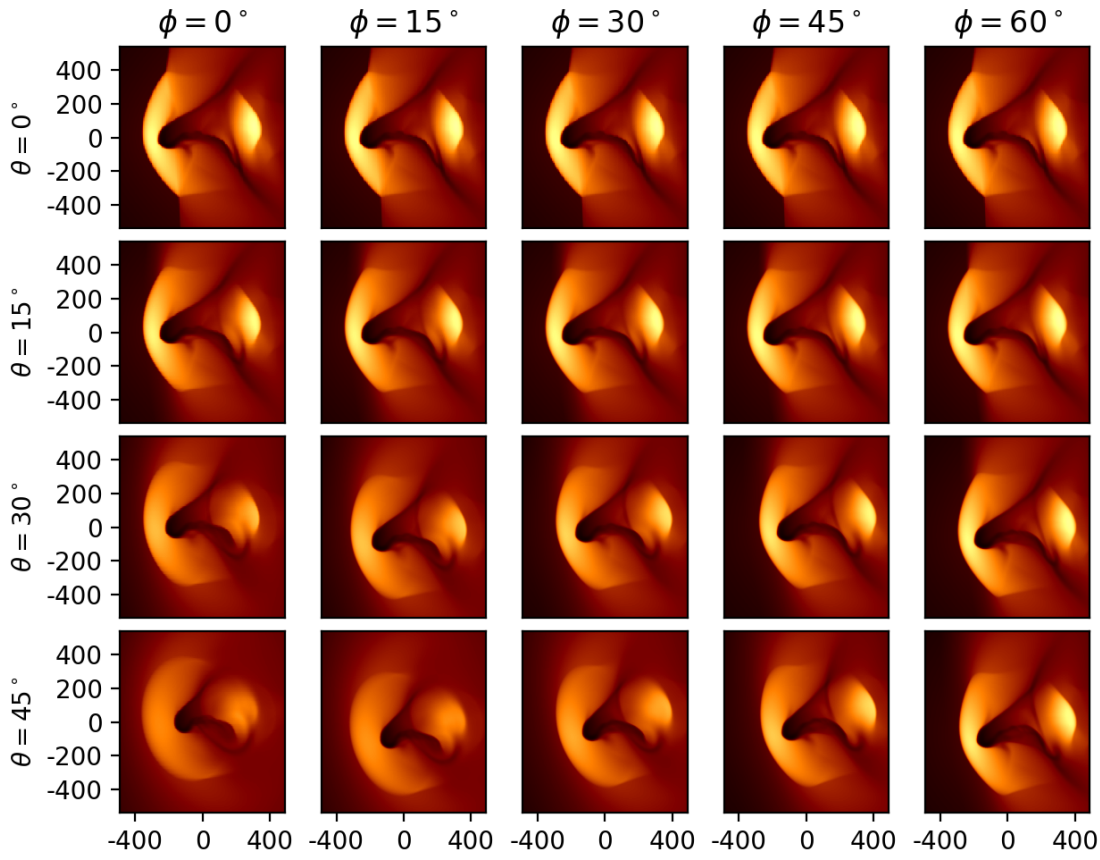


Figure 3.6: The effect of changing the viewing angles ($\theta$, $\phi$). Mazzotta-weighted projected temperature maps for the simulation with $M_1 = 5 \times 10^{14} \mathrm{M}_\odot$, $R = 1:3$, $b = 100$ kpc, $v_{\mathrm{rel}} = 1452$ km/s. Any viewing angle that is not perpendicular to the plane of the merger will cause weaker apparent shocks. Each panel is 800 kpc a side, and the colormap is the same as for all simulated temperature maps. We find that shocks are visible from every viewing direction shown here, i.e., visibility of shocks is not a guarantee of a nearly plane-of-sky merger.

such as projected X-ray surface brightness, spectral-like weighted temperature following Mazzotta et al. (2004) (henceforth Mazzotta-weighted), and total mass density for a range of mass ratios and impact parameters in binary merger simulations. Using the simulation set "A Parameter Space Exploration of Galaxy Cluster Mergers" in the Galaxy Cluster Merger Catalog[3] (Zuhone et al., 2011), we identified a region of parameter space to explore further to find an analog for Abell 2146. If the subhalo is very close in mass to the primary halo, the system would look more symmetric; if the mass of the subhalo is too small, the cold front would be much weaker and the core of the primary halo is barely disrupted. If the impact parameter is close to zero, both cores are extremely disrupted and the standoff distance between the bow shock and cold front is too big; if it is too large, the cold remnant core of the subhalo appears extremely curved as the cores accelerate towards each other. Lastly, for the cold front and both shocks to be prominent, the observation must have occurred shortly after first pericentre passage. The X-ray features of Abell 2146 were qualitatively similar to the mergers with a mass ratio of 1:3 and a small, non-zero impact parameter, seen (0.3-0.5) Gyr post pericentre passage. In this work, we will explore more finely around this position in parameter space, and additionally study the effects of varying dark matter and gas profiles of the halos, relative velocity, and viewing direction.

If the BCGs are relatively good tracers of the potential minima, the orientation of the merger is well-constrained by the angles ($\theta$, $\phi$) for which the 3D separation and relative velocities of the potential minima in the simulation match observations after projection. The projected maps of surface brightness, temperature and mass should be made for the appropriate viewing direction to compare with observations.

In addition to the BCGs, we can also use the separation between the bow and upstream shocks, which evolves rapidly, to identify a small number of snapshots for further inspection. As shown in Fig. 3.6, we find that the shocks appear too weak if $\theta \gtrsim 30^\circ$ and $\phi \gtrsim 30^\circ$. The observed separation between the leading edges of the two shocks is 440 kpc (Russell et al., 2010). Therefore, we only keep snapshots where $440 < \mathrm{d} < 508$ kpc, where the upper bound ensures that $d \cos 30^\circ \leq 440$ kpc.

The purpose of this study is to investigate how observed properties of the system depend on each of the input parameter of the simulation. Through a preliminary round of parameter tests, we chose to zoom in on the region around a primary cluster mass $M_1 = 6 \times 10^{14} M_\odot$, a mass ratio $R = 1:3$, an impact parameter $b = 100$ kpc, and initial relative velocity $v_{rel} = 1500$ km/s. The following sections describe the zoomed in region of parameter space, so as to focus on systems like Abell 2146.

### 3.4.2 Viewing direction

As shown in Fig. 3.1, the merger in our simulations occurs in the x-y plane of the simulation domain, with the initial relative velocities along the x-axis and initial impact parameter

[3]http://gcmc.hub.yt/fiducial/index.html

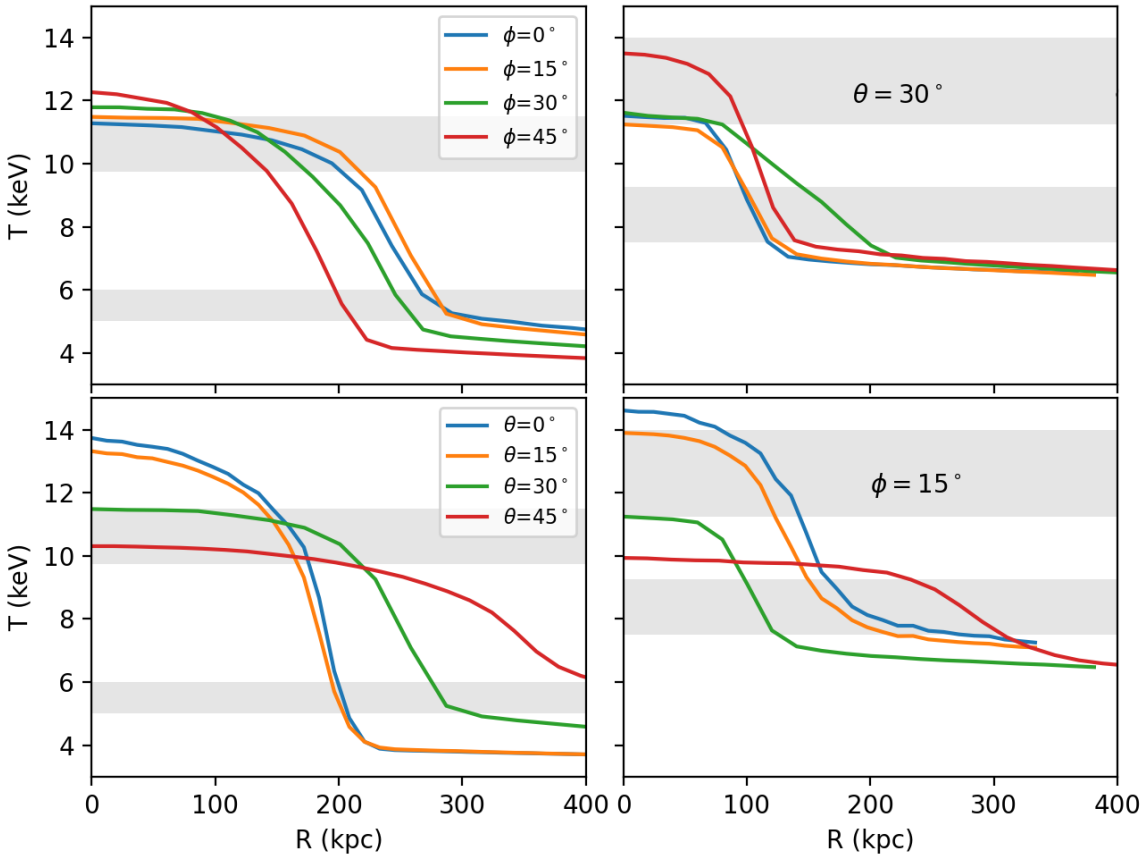


Figure 3.7: The temperature profiles of the bow (left) and upstream (right) shocks for different viewing directions. The top panels hold $\theta = 30°$ and vary $\phi$, while the bottom panels hold $\phi = 15°$ and vary $\theta$. The shaded grey regions show the 1-$\sigma$ error bars on the pre- and post-shock temperatures for the corresponding shocks from Russell et al. (2012).

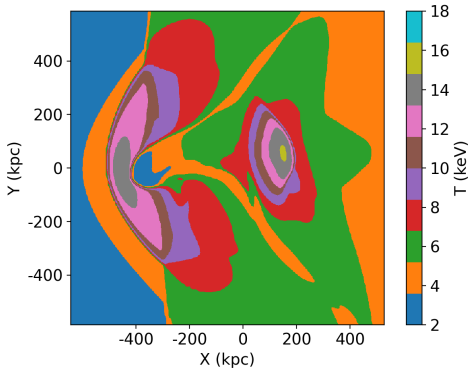


Figure 3.8: Temperature map for one of the snapshots similar to Abell 2146, using a discrete colormap to emphasise the gradient in pre-shock temperature. Changing the viewing angle would lead us to see the shock at a smaller distance from the primary cluster core, where the background temperature is higher. As a result, the shock will appear weaker.

along the y-axis; this defines the so-called plane of the orbit. The default line-of-sight is in the z-direction, as is the angular momentum. Instead, if the observer views the system along some different direction, they would see a different projection of the 3D system. Each viewing direction is defined by viewing angles $(\theta, \phi)$, where $\theta$ is the polar angle and $\phi$ the azimuthal angle (see Fig. 3.1).

Fig. 3.6 illustrates the effect on the appearance of a simulation of changing the two viewing angles for a given snapshot. For small values of $\phi$, increasing $\theta$ (a) increases the apparent pre-shock temperature, (b) increases the stand-off distance between the cold front and the bow shock and (c) decreases the apparent offset between shocks. The latter effect is the smallest, because the two shocks have large radii of curvature. Increasing $\phi$ has a barely discernible effect for low $\theta$, but as seen in the panels for $\theta \gtrsim 30°$, counters the effect of changing $\theta$ alone. Each of these effects can be explained by simple geometric arguments.

The shocks form along the axis of motion of the substructure through the ICM, in the x-y plane, so their separation is maximal along that axis. The velocities of the two subclusters are also entirely in the x-y plane, so that if viewed along the z-axis, the line-of-sight velocity difference between the subclusters is 0. The unperturbed cluster is spherical, and the radius of curvature $R_s$ of the shock front is smaller than its cluster-centric radial position $r$. The unshocked gas can be assumed to move at approximately the same speed around the shock front, but the jump conditions only apply to the component of the gas velocity perpendicular to the shock front at any point. The speed of the shock at each point on the front is therefore $v \cos \eta$, where $\eta$ is the angle between the normal to the front and the velocity of the front with respect to the gas; thus $\eta = 0°$ at the leading edge of the shock. Changing the viewing direction generally moves the point where our line of sight is tangent to the shock front away from the leading edge of the shock, so that the observed

shock strength is weaker. This additionally moves the tangent point to smaller $r$, increasing the preshock temperature at the tangent point. Finally, the radius of curvature $R_c$ of the cold front is smaller than $R_s$. This means that the minimum separation between the two features, i.e.,the standoff distance, is minimised in the plane of the merger, and increases for other viewing directions. Each of these phenomena can be understood intuitively as illustrated in Fig. 3.8, which shows a simulated temperature map with a discrete colormap to accentuate the difference in temperature depending on the position $r$.

Older simulation studies, tailored to the observing capabilities of telescopes like ROSAT, stated that the merger needs to be close to the plane of the sky for the shock features to be visible (e.g., Ensslin et al., 1998; Ricker, 1998), although how close is not clearly defined. Fig. 3.6 shows, however, that both shock fronts are distinctly visible even for inclinations as high as $(\theta = 30°, \phi = 15°)$. Therefore, the visibility of shocks does not constrain the merger axis to be very close to the plane of sky.

Instead, we need a more quantitative comparison, as shown in Fig. 3.7. Note that this is for $M_1 = 5 \times 10^{14} M_\odot, M_2 = 1.6 \times 10^{14} M_\odot$. Higher masses would increase the normalisation of the temperature profiles. The horizontal shaded areas show the 1-$\sigma$ error bars on the pre- and post-shock temperatures for Abell 2146 (Russell et al, in prep.). From Fig. 3.6, we find that $\theta = 30°$ produces the correct standoff distance at $\phi = 0$. The top panel of Fig. 3.7 shows the temperature profiles across the bow (left) and upstream (right) shocks for various values of $\phi$ at $\theta = 30°$, with good matches to the observations for $\phi < 15°$. The bottom panel then holds $\phi = 15°$ and varies $\theta$. In this way, we find that $\theta = 30°$ matches observations. Lower values result in a post-shock temperature that is too high, while higher values cause the shock to be much shallower than observed.

The standoff distance between the bow shock and the cold front also depends on the relative velocity, or, equivalently, the angular momentum of the merger. To break this degeneracy, we aim to additionally reproduce the observed line-of-sight velocity offset between the BCGs (White et al., 2015). Our simulations do not explicitly include cluster galaxies; however, BCGs are known to trace the potential minima of galaxy clusters (e.g., Zitrin et al., 2012, and references therein). The potential minima of the halos were identified using the `peak-local-max` function in the Scikit-Image Python package on the slice of the gravitational potential in the x-y plane. The velocity $v$ of a BCG is estimated as the average velocity of all the dark matter particles within 50 kpc of its potential minimum; this radius is characteristic for BCGs of clusters of the masses considered (e.g., Lin & Mohr, 2004, and references therein). The line-of-sight velocity difference between the BCGs depends on the viewing angle, as detailed in §3.2.2.

### 3.4.3 Total mass and mass ratio

Increasing the total mass, first of all, increases the overall projected temperature, since the thermal pressure now has to balance a greater weight of overlying gas. The Mazzotta-

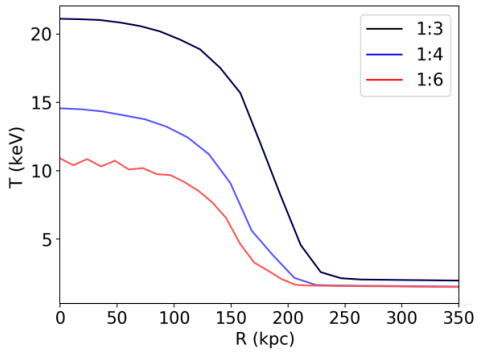


Figure 3.9: Projected temperature profiles of the bow shock for same primary halo mass but different mass ratios. Not only is the peak temperature significantly higher for a more massive secondary halo, but the shocked region is wider.

weighted average temperature of A2146 within a radius of 2 arcmin ($\simeq 440$ kpc), covering both the shocks, is 7.5 $\pm$ 0.3 keV if the cool core (of radius 10" or 37 kpc) is excised and 6.7 $\pm$ 0.3 keV if it is included (Russell et al., 2012). Simply by matching the limits of the colorbars in the observed and simulated maps of projected temperature, we can visually rule out systems whose average temperature is too small or too large. The core-excised (included) average temperatures for the 1:3 mass ratio mergers presented in Fig. 3.10 are 5.62 (5.15) for $M_{\rm tot} = 6.6 \times 10^{14} M_{\odot}$, 7.33 (6.23) for $M_{\rm tot} = 8.1 \times 10^{14} M_{\odot}$ and 8.10 (6.30) for $M_{\rm tot} = 9.4 \times 10^{14} M_{\odot}$, where $M_{\rm tot} = M_1 + M_2$ is the sum of the two total masses in the super-NFW formulation. The corresponding total virial masses are $(4.5, 5.4, 6.3) \times 10^{14} M_{\odot}$, with the middle value consistent with observed temperatures assuming that the merger occurs in the plane of the sky. Fig. 3.10 further reminds us that if the merger does not occur in the plane of the sky, the observed temperature is an underestimate. Therefore, a greater mass is possible if the viewing angles are larger.

Secondly, increasing the total mass increases the scale radii of the two halos. This means that for the same absolute magnitude of the impact parameter, greater fractions of the two cluster cores interact with each other during pericentre passage. In other words, increasing halo mass while holding impact parameter constant is equivalent to holding mass constant and reducing impact parameter, so that the cores are more disrupted. In the second row of Fig. 3.10, this is seen as a "fatter" bullet and a less prominent plume, either due to higher total mass at fixed mass ratio (top row), or higher mass ratio at fixed primary halo mass (second row). The acceleration due to increased halo mass also means that for the same initial relative speed in the simulation, the shocks produced at the best-fit snapshot are stronger. Fig. 3.9 additionally quantifies the difference between using different mass ratios but same mass for the primary halo, by plotting the temperature profiles out from the peak of the bow shock.

Increasing the mass of the secondary also increases ram pressure stripping of the

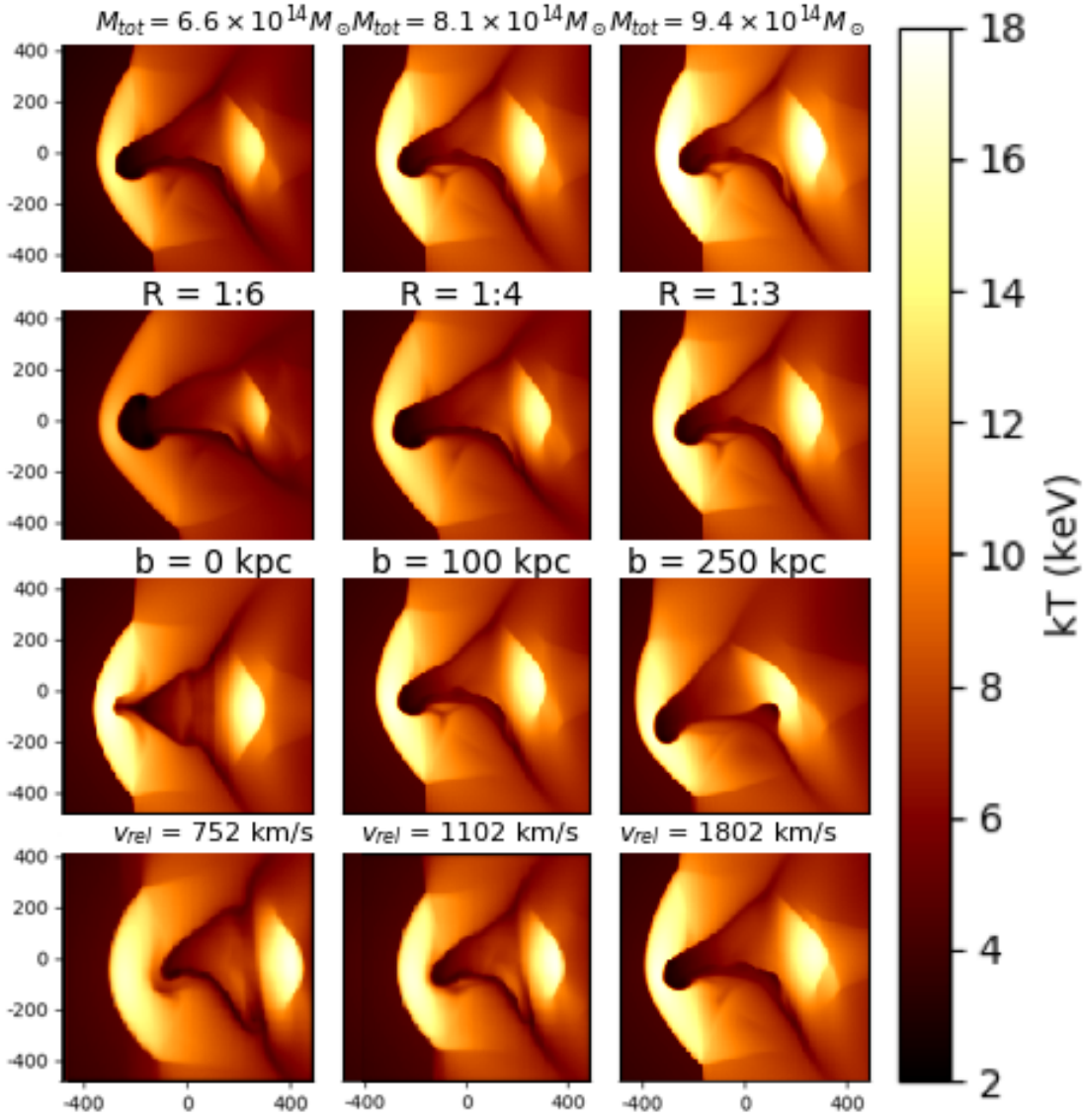


Figure 3.10: The effect of changing key dynamical parameters one at a time, holding all the others constant. *Top row:* Increasing the total mass of the system (shown in units of $10^{14} M_\odot$) increases the temperature of the ICM as well as the shocks. *Second:* Increasing the mass of the secondary cluster, and therefore the mass ratio $R = M_1 : M_2$, increases the strength of the shocks as well as increasing the standoff distance. *Third:* Increasing the impact parameter $b$ (in kpc), while holding all other parameters constant, curves the path of the secondary cluster core towards the primary core, creating a more arced cold front. The relative sizes and orientations of the different X-ray features are most significantly affected by $b$. *Bottom row:* Increasing the initial relative speed of the cluster centres increases the strengths of the shocks, but reduces the standoff distance and changes the radii of curvature of the shock fronts.

secondary core. This can be seen in narrowing of the leading edge of the core, the formation of a stronger upstream shock, and a larger standoff distance. Based on the second row of Fig. 3.10, then, we favour a mass ratio of 1:3. The standoff distance is still lower than in observations, but, as discussed above, this can be fixed with a larger $\theta$.

### 3.4.4 Impact parameter and initial relative speed

The X-ray observations rule out a perfectly head-on merger because the disrupted subcluster core is asymmetric. The head of the bullet is curved, and its tail fans out more towards the South than to the North. The greater the impact parameter, the greater this asymmetry. The appearance of this bullet is thus affected by the orientation of our line of sight with respect to the plane of the orbit. Fig. 3.6 showed this for the case $b = 100$ kpc. If viewed from sufficiently close to the plane of the orbit, the curvature of the bullet becomes very hard to perceive, and it becomes difficult to distinguish from a merger with a zero impact parameter. For larger $b$, however, the curvature of the bullet is too large to be erased by modest inclination of the merger plane with the plane of the sky. Furthermore, the core of the subcluster experiences very little ram pressure, and the cold front is much wider than observed. Similarly, the core of the primary cluster is less perturbed for larger $b$, leaving an intact core rather than a "plume". Given these effects, we can constrain $b \sim 100$ kpc.

As seen in the last panel of Fig. 3.10, increasing the relative velocity of the perturber increases the strength of the shock. The effect on the standoff distance is less linear. On the one hand, if the subcluster moves faster through the ICM, it stays closer to the bow shock, and this decreases the standoff distance decreases. We see this effect as we increase $v_{rel}$ from 720 to 1252 km/s. But increasing the velocity also increases the ram pressure, pushing gas from the subcluster core away from its direction of motion and increasing the standoff distance. This is what we see in further increasing $v_{rel}$ to 2200 km/s. Given the observed strength and width of the upstream shock, the intermediate speed of 1252 km/s is most likely; the observed standoff distance can then be increased by increasing $\theta$, as is already encouraged by the analyses of total mass and mass ratio.

### 3.4.5 Dark matter concentration

A higher concentration for either cluster makes its core more compact and resistant to disruption. If the primary cluster is more concentrated, there is more gravitating mass enclosed within the core, and the subcluster bullet is accelerated more during infall. As a result, the gas in the subcluster experiences higher ram pressure $p_{\rm ram} = \rho v^2$. This causes more gas to be swept away from the leading edge of the subcluster core, into a wake, which is undergoing a reverse shock. This has two observable consequences. Slowing the gas "bullet" increases the standoff distance between the bow shock and the cold front. At the same time, the gas displaced from the core of the infalling cluster impedes the gas infalling

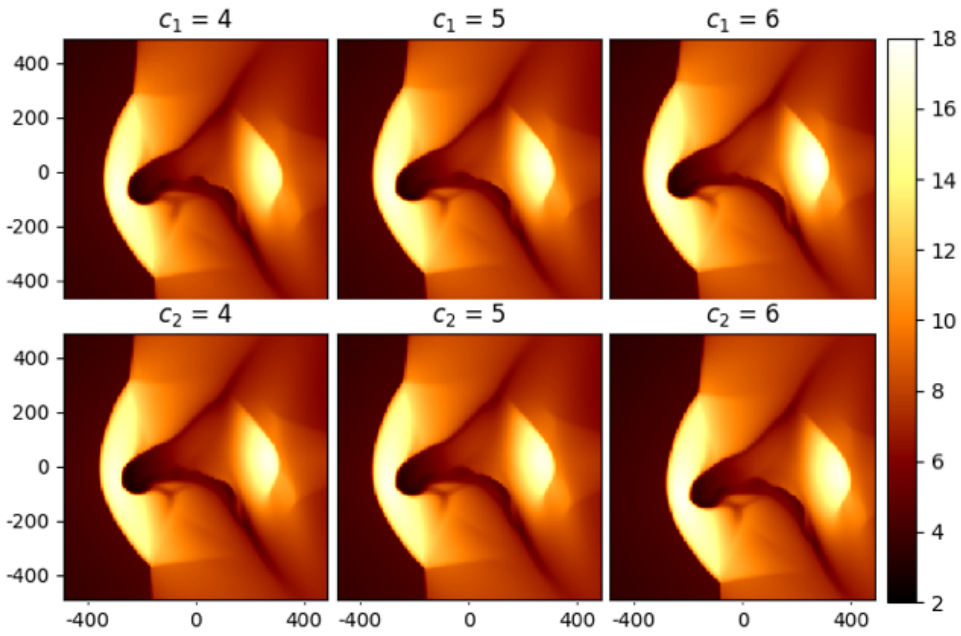


Figure 3.11: The effect of changing the dark matter concentration of the primary (top) and secondary (bottom) halo while holding all other parameters constant. A lower concentration for the primary, or a higher one for the secondary, results in more instabilities along the cold strip of gas connecting the two disrupted cores. We note that the details of KHI are sensitive to the presence of turbulence in the ICM, which we have not included. All other features remain unaffected.

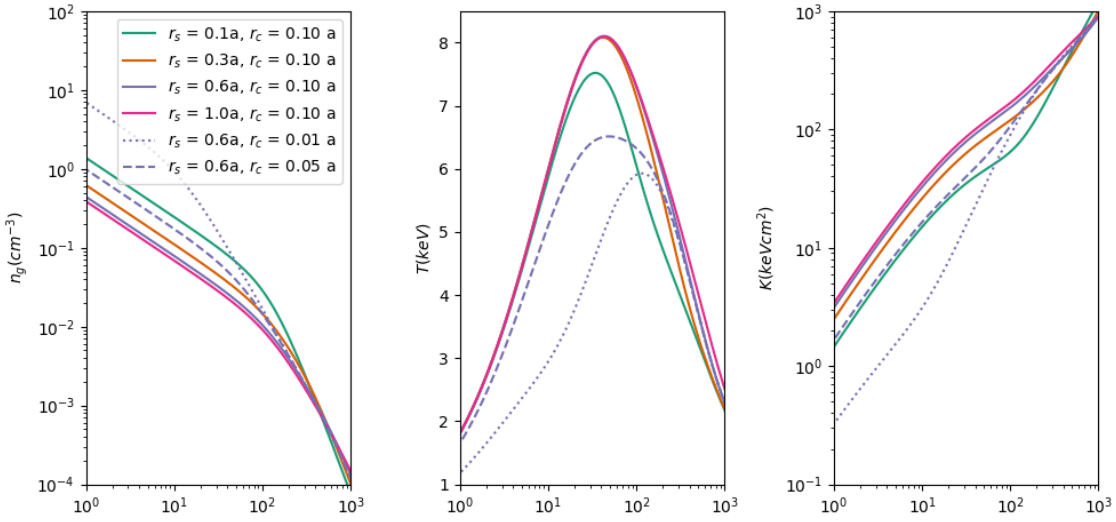


Figure 3.12: The effect of varying the gas scale radius $r_s$ in Eq. 3.3 and core radius $r_c$ for $\alpha = 2$. Here, $M_{sNFW} = 1.6 \times 10^{14} M_{\odot}$, $c_{\rm NFW} = 5.2$, and $r_c = 0.1a$. Decreasing either the scale or core radius produces a denser, lower-entropy core. While there is a spread in observed cluster cores, we find that the cool core population is generally well fit with $\alpha = 2, r_c \sim 0.05a$ and $r_s = 0.6a$, so that the entropy decreases monotonically towards the centre. Through a similar comparison, we describe non-cool cores with $\alpha = 0$, $r_c \sim 0.3a$ and $r_s = 0.6a$.

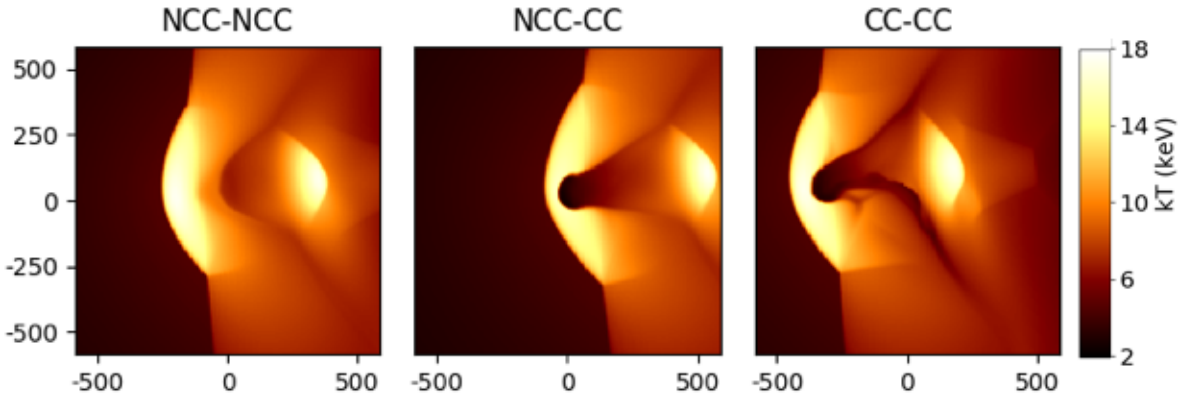


Figure 3.13: The morphology of the merger looks extremely different depending on whether each of the components has a cool or non-cool core. Here, both clusters are modeled with $\alpha = 0$; the cool cores have core radii $r_c = 0.02a$, and the non-cool cores have $r_c = 0.5a$, where $a$ is the NFW scale radius. Abell 2146 clearly resembles a system where both components were initially cool-core clusters.

from further in its wake, boosting the strength and extent of the upstream shock. Both of these effects are shown in the top panel of Fig. 3.11. The bottom panel shows that the plume feature associated with the core of the primary halo is brighter and less disturbed if its concentration is higher. We find that the concentration of the subcluster, on the other hand, has no appreciable effect on the gas observables. Since other parameters affect the same observables much more dramatically, we find that $c_2$ is not well-constrained by X-ray imaging.

We note that this result is for mergers of the explored mass ratios, 1:3-1:6. If a merger is closer to equal mass, $c_2$ would have much the same effect as $c_1$ on the gas in the other merging component.

The standoff distance was smaller than observed for the parameters tested in Fig. 3.10, which all used $c_1 = 4.1$. A denser dark matter halo, like $c_1 = 5$, would solve this issue and remove the need for larger $\theta$.

### 3.4.6 Gas profiles

The model in Eq. 3.3 contains two parameters that affect the compactness and cuspiness of the core - the core radius $r_c$ and the central density slope $\alpha$. The scale radius $r_s$ and the outer slope parameters $\beta$ and $\epsilon$ affect the outskirts, so we do not vary them in our study and just use the best-fit values from Vikhlinin et al. (2006).

It is important to note that $r_c$ is a purely empirical parameter, which can be arbitrarily tuned in the Vikhlinin et al. (2006) formulation to match the data. We would like to choose core radii that produce profiles analogous to observed relaxed clusters (De Grandi

& Molendi, 2002; Vikhlinin et al., 2005; Hogan et al., 2017). As shown in Fig. 3.12, our profiles look like cool-cores, with high central densities and temperatures decreasing in the centre, for $\alpha = 0,\ r_c/a$ = 0.02; for $\alpha = 0,\ r_c/a$ = 0.5, they have lower, flat central densities and high central temperatures, like observed non-cool cores. While we acknowledge that the cores of clusters do not follow a strict dichotomy, we use these pairs of parameters when modelling each halo as a cool or non-cool core.

Fig. 3.13 shows that the X-ray images of the merger depend strongly on whether, per our modeling above, each cluster has a cool- or non-cool core. In the left panel, both halos have a non-cool core. In the middle pannel, the subcluster has a cool core, and on the right, both clusters have cool cores. The three scenarios are strikingly different. When either core is non-cool, it is more extended and more susceptible to stripping. A cool-core secondary cluster will produce a bullet-like cold front; there is no low-entropy gas to form such a feature if it were a non-cool core. The remnant of the primary cluster core remains partially intact if it starts out as a cool-core, with the remainder drawn out into a plume-like shape if the secondary also has a cool core, as seen in Abell 2146. If it is a non-cool core, there is no low-entropy material to start with and form the plume. We therefore conclude that both the primary and secondary clusters in Abell 2146 must have had cool cores before the merger. Small adjustments of $r_c$ around the best-fit value of $0.02a$ then have very small effects on the width of the bullet (subcluster core remnant) and brightness and extent of the plume (primary cool remnant).

### 3.4.7 Best fit simulations for Abell 2146

Our simulations are consistent with the X-ray observations for a primary halo of virial mass $M_1 = 5.0 \times 10^{14} M_\odot$ and an infalling halo mass $M_2 = 1.6 \times 10^{14} M_\odot$, so that the mass ratio R = 1:3, observed 0.1 Gyr after pericenter passage. Both clusters initially have cool cores. The larger mass in each case would require the merger to be inclined with respect to the plane of the sky. The concentration of the more massive halo is $\sim 5$, on the higher end of the scatter in the concentration-mass relation; the concentration of the subhalo does not visibly affect either the X-ray or lensing maps. The initial relative speed of the cluster centres was likely $v_{\rm rel} \simeq$ 1200 km/s, and impact parameter $b$ = 100 kpc. The separation between the features is best reproduced at $\theta = 30^\circ$. Then, the observed temperature profiles as well as line-of-sight velocity offset between the BCGs is matched for $\phi = 15^\circ$.

## 3.5 Discussion

### 3.5.1 Error bars including covariance

Although, in principle, an error region could be constructed for the model of A2146, this is not feasible with current computing resources. Since the parameters affect the

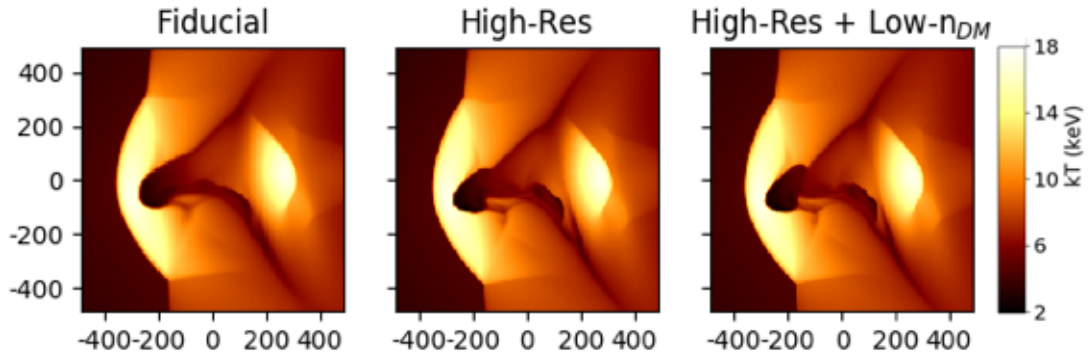


Figure 3.14: The effect of increasing the maximum refinement level (middle panel) and then halving the number of dark matter particles (right panel), in comparison with the resolution of this study (left panel). Doubling the hydrodynamic resolution increases the growth of fluid instabilities all along the cold discontinuities. However, the shock separation, standoff distance, average temperature, shock Mach numbers and the velocity offset between the BCGs remain unchanged. Reducing the force resolution by halving the number of dark matter particles has a negligible effect on the KHI.

same features in different ways, mapping out the interdependence of observed features on the parameters would require a large suite of simulations sampling many combinations of all the significant parameters, including $M_1$, R, b, v, $\theta$, $\phi$, $c_1$. This leaves us with a 7-dimensional space even after fixing the parameters $c_2$, $\alpha_1$, and $\alpha_2$, which which have less visible impact on the X-ray images. For each simulation in such a study, it will be important to quantify the similarity of each snapshot to the observation. This would have to involve some combination of at least the shock separation, the standoff distance, the shock strengths, and the average temperature with and without the cool core. Even exploring just three values for each parameter yields over 240 simulations, each of which would need to be viewed from at least 9 different viewing directions, for a total of $\sim$2200 inspections. This cannot be done manually in the same way as in this pilot study. Instead, it would require a pipeline to compare simulations to observations and move in the parameter space. Nevertheless, here we have explored the physical impact of each of these parameters on a binary merger like A2146, demonstrating the observable impacts of each parameter on the system and providing a basis for the interpretation of similar systems in the future.

### 3.5.2 Resolution tests

We tested the effect of adding an additional refinement level, i.e., doubling the spatial resolution and octupling the mass resolution. Increasing the resolution primarily reduces numerical viscosity, permitting faster growth of fluid instabilities, notably the Kelvin-Helmholtz Instability (KHI). Indeed, Fig. 4.9 shows that the boundaries of the bullet-like cold front are more disrupted, and clear wave-like structures appear in the bridge connecting

the two cool-core remnants. This will be significant in future studies that measure the plasma viscosity based on the development of KHI. It will also affect measurements of thermal conduction, which rely on the width of the contact discontinuities; this width cannot, of course, be lower than the simulation resolution. The distances between the features, however, remain unchanged, as do the temperature and velocity structures. Since these are the properties we use to constrain parameters in this study, we conclude that the hydrodynamic resolution of 6.8 kpc is sufficient. Reducing the number of dark matter particles by half also did not change the results; for similar studies in the future, we would recommend using this lower number of dark matter particles to reduce the simulation time by $\sim 40\%$.

## 3.6 Conclusions

We have performed a large suite of idealised simulations of binary mergers between galaxy clusters using the GPU-accelerated adaptive mesh refinement code GAMER-2, with the goal of constraining merger parameters using deep Chandra X-ray and lensing observations of Abell 2146. We assess the roles of halo masses, NFW concentrations, gas profiles, impact parameter, initial relative velocity, and viewing direction on observable quantities on X-ray properties and gravitational lensing observations. In searching for a simulated analog of the observed cluster merger Abell 2146, we find various results that will be helpful for any future interpretations of merging galaxy clusters. These will allow us to understand the laboratory, before using it as a test site for constraining cosmology and ICM microphysics. Our main findings are summarized as follows:

- The average temperature including and excluding the cool core pointed to a virial mass of $M_1 = 5.0 \times 10^{14} \mathrm{M}_\odot$ for the primary halo and $1.6 \times 10^{14} \mathrm{M}_\odot$ for the secondary halo.

- The large standoff distance favours an initial infall speed of $v_{\rm rel} = 1150\,\mathrm{km\,s^{-1}}$ and a viewing direction offset from the perpendicular to the plane of the merger (the $z$-axis) by about $30^\circ$ in the initial direction of motion of the infalling subcluster [$\theta = 30^\circ$]. The observed strengths of the bow and upstream shocks are then reproduced for $15^\circ < \phi < 30^\circ$. This viewing direction also brings the simulated velocity offset between the cluster potential minima in agreement with the observed line-of-sight velocity difference of the BCGs.

- If the primary cluster has a cool core, it is more efficient at stripping the secondary core, resulting in a stronger and brighter upstream shock than if it had a non-cool core. If the secondary cluster has a cool core, it is more resilient to stripping, and disrupts the core of the primary cluster to form a plume-like feature. If instead it is a non-cool core, almost all the gas is stripped into an upstream shock behind

the primary core, which in turn remains almost intact. We conclude that the cold "bullet" and "plume" features are the remnant cores of the secondary and primary clusters, respectively, if both clusters initially had cool cores and fell in with an impact parameter of $b = 100$ kpc.

- Smaller subcluster masses, smaller initial relative velocities, and larger impact parameters all result in lower Mach numbers for the shocks.

- In principle, increasing the dark matter concentration of the primary halo slightly strengthens the upstream shock and increases the standoff distance of the bow shock, i.e., its separation from the cold front. This is because the bullet is slowed by the greater ram pressure. However, using $3 < c_{\rm NFW} < 6$ for both clusters did not produce significant enough differences in the simulated X-ray images. Therefore, X-ray images alone are unable to constrain the dark matter concentrations of the halos.

- We find that the total mass of A2146 is significantly lower than previous determinations based on weak lensing data, and that (driven by the X-ray measurements) the more massive cluster is Abell 2146-B. The former factor can be explained since the parameterised models assumed NFW profiles with concentrations expected for relaxed cluster halos, whereas the core of the merging system is gravitationally compressed around pericentre passage, effectively increasing the concentration of the NFW model for each halo. Instead, it is important to consider lower halo masses than suggested from the earlier lensing analysis, and forward model using the simulations to obtain the synthetic lensing signal. That Abell 2146-A is the more massive cluster in the lensing analysis is still unexplained and is beyond the scope of this work.

This study paves the way for extracting more information from X-ray and optical observations for merging galaxy clusters. We have demonstrated how X-ray measurements alone can tightly constrain the halo masses even in a non-equilibrium system. The time since pericentre passage, impact parameter, dark matter concentration of the primary halo, and viewing direction can all be constrained using X-ray maps alone, and can be corroborated with optical measurements of BCG positions and velocities. The masses and velocities of merging clusters provide tests of cosmological models, which will be crucial in ongoing and upcoming surveys like eROSITA, DES, HSC, and Rubin. Once these hydrodynamic parameters have been constrained, a given merging cluster can then be used to study the nature of dark matter and ICM microphysics, such as viscosity, thermal conductivity, and magnetic field strength.

# Chapter 4

# MHD effects in merging clusters: A case study of Abell 2146

*U. Chadayammuri, J. A. ZuHone, P.E.J. Nulsen, D. Nagai, H. Russell*

[1]Chandra X-ray Center, Smithsonian Astrophysical Observatory, 60 Garden Street, Cambridge, MA 02143, USA
[2]Department of Physics, Yale University, 52 Hillhouse Ave, New Haven, CT 06511, USA
[3]School of Physics and Astronomy, University of Nottingham, Nottingham NG7 2RD, UK

**Submitted to MNRAS Oct 2021**

## Abstract

Kelvin-Helmholtz Instabilities (KHI) along contact discontinuities in galaxy clusters have been used to constrain the strength of magnetic fields in galaxy clusters, following the assumption that, as magnetic field lines drape around the dense interface between the cold and hot phases, their magnetic tension resists the growth of perturbations. This has been observed in simulations of rigid objects moving through magnetised media and sloshing galaxy clusters, and then applied in interpreting observations of merger cold fronts. Using a suite of MHD simulations of binary cluster mergers, we show that even magnetic field strengths stronger than yet observed ($\beta = P_{\rm th}/P_B = 50$) show visible KHI features. This is because our initial magnetic field is tangled, producing Alfven waves and associated velocity fluctuations in the ICM; stronger initial fields therefore seed larger fluctuations, so that even a reduced growth rate due to magnetic tension produces a significant KHI. The net result is that a stronger initial magnetic field produces more dramatic fluctuations in surface brightness and temperature, not the other way around. We show that this is hard

to distinguish from the evolution of turbulent perturbations of the same initial magnitude. Therefore, in order to use observations of KHI in the ICM to infer magnetic field strengths by comparing to idealized simulations, the perturbations which seed the KHI must be well-understood and (if possible) carefully controlled.

## 4.1 Introduction

Merging galaxy clusters provide unique constraints on the nature of dark matter and the plasma physics of the X-ray emitting intracluster medium (ICM). This hot, diffuse gas consists of baryons trapped in the cluster gravitational potential early in its formation. It evolves with time as the cluster accretes material from the cosmic web and merges with other clusters. Internally, the ICM is also affected by radiative cooling, turbulence, and feedback from AGN in the cluster galaxies; over time, these shape its temperature, density and metallicity profiles. How energy and metals are distributed in the presence of these processes further depends on transport processes, namely viscosity, thermal conduction, and ion diffusion. Spitzer (1952) and Braginskii (1958) derived the viscosity and thermal conductivity for a weakly collisional plasma, including how this is suppressed in the presence of a uniform magnetic field (Sarazin, 1988). Since then, a number of works have shown that plasma instabilities further impede cluster transport processes (e.g., Schekochihin et al., 2008; Kunz et al., 2011, 2012; Roberg-Clark et al., 2016).

Magnetic fields in clusters are understood to have grown from primordial seeds of $\sim 1nG$ (Ruzmaikin et al., 1989; Subramanian et al., 2006) to the observed present-day strengths of several microgauss ($\mu G$) through turbulence and bulk flows inherent in the process of hierarchical, merger-driven structure formation (e.g., Dolag et al., 2002; Medvedev et al., 2006; Vazza et al., 2014). In galaxies and clusters, they are crucial to understanding the transport of energy, metals and cosmic rays.

Most commonly, cluster magnetic fields are detected using radio observations. Using assumptions about the properties of cosmic ray electrons, we can infer the presence of diffuse magnetic fields from radio halos, radio mini-halos, and radio relics (e.g., Ensslin et al., 1998; Carilli & Taylor, 2002; Ferrari et al., 2008; Feretti et al., 2012). Another signature is the Faraday rotation induced in background radio sources, i.e., the change in the polarisation angle of background light by magnetic fields. The polarisation angle of a linearly polarised radio source varies with wavelength, $\lambda$, as $\mathrm{RM} \times \lambda^2$, where the Faraday rotation measure $RM \propto \int n_e B_{\parallel} dl$. This signal cannot be produced by anything other than a magnetic field; the only required corrections are for the foreground magnetic field of the Milky Way and, for Faraday rotation intrinsic to the radio source. The most detailed RM analysis in galaxy clusters to date has been of the Coma cluster, using seven radio sources at different radii (Bonafede et al., 2010). Assuming each point source to be representative of its radial annulus, and that the field followed a radial power law $\mathrm{RM} \propto \mathrm{r}^{-\eta}$, the study

found a slope $0.4 < \eta < 0.7$ within $1\sigma$.

Such analyses, of course, come with caveats. First, the measurements are local, restricted to regions with bright background radio sources. Next, the power law form assumed for the magnetic field profile is likely too simple. Since magnetic flux is frozen into the cluster gas, the mean magnetic pressure is expected to scale with the mean turbulent pressure. Further assuming that the turbulent Mach number is uniform through the plasma, the magnetic pressure can then be related to the thermal pressure $P_{\rm th} = kT \times n_g$. Observations, such as Dolag et al. (2001), have indeed found the correlations between the magnetic and thermal pressure in cluster plasmas. The thermal pressure profile has been shown to have a universal form, with different slopes in the core and outskirts (Nagai et al., 2007b; Arnaud et al., 2010). Constraining more parameters inevitably requires sampling the diffuse field at more points. Further, the RM tells us only about the component of the magnetic field along our line-of-sight. Converting this into the total field strength usually entails the assumption that its distribution is isotropic. This is certainly not the case during a cluster merger, where the field lines drape around the dense, low-entropy core of the subcluster (e.g., Dursi & Pfrommer, 2008). This list is not meant to be exhaustive, but illustrative of the limitations of a single method of measurement, and to emphasise the need for alternative metrics of the cluster field. While none of them can be perfect in isolation, each can provide more local measurements, which can compose a fuller picture of the global magnetic field.

Given the density and temperature of the ICM, the mean free path of the electrons and ions are on the order of kpc, whereas given the magnetic field strength of $\sim \mu$G and electron and ion temperatures, their Larmor radii are on the order of AU. This means that the transport across the field lines is heavily suppressed, making the transport processes highly anisotropic (Ruszkowski & Oh, 2010; Kunz et al., 2011; Kunz, 2011; Kunz et al., 2012). If the field lines are highly tangled, transport may be suppressed generally. Further suppression can result from plasma instabilities, which may drive waves that scatter the ions or electrons strongly (e.g., Schekochihin et al., 2008; Roberg-Clark et al., 2016). Because our understanding of the net effect of these instabilities and anisotropies is still evolving, extracting field strengths using constraints on the effectiveness of transport processes still entails significant theoretical uncertainty.

Yet another measure of cluster magnetic fields uses observed X-ray features of merging clusters. As the dense, low-entropy core of a subcluster moves through the hotter surrounding ICM during a merger, magnetic fields drape around its leading edge, forming a highly magnetized layer parallel to the front surface (Lyutikov, 2006); this draping also changes the geometry of the cold front, leaving it with smaller opening angles (e.g., Dursi & Pfrommer, 2008; Zuhone et al., 2011). Noting that such a sheath inhibits the growth of perturbations, Vikhlinin et al. (2001) used the lack of observed Kelvin-Helmholtz Instabilities (KHI) at the leading edge of the cold front in the merging cluster Abell 3667 to estimate $B \sim 10\mu G$. Similarly, if the KHI in sloshing cold fronts in Virgo are suppressed

by ICM viscosity, Roediger et al. (2013) found that this viscosity would have to be at least $\lesssim 0.1\nu_{\rm Spitzer}$. Magnetic fields offer one channel for such a viscosity suppression.

Here, we present just such a study of the merging galaxy cluster Abell 2146, whose complex ICM was first observed in the X-ray with the *Chandra* X-ray Observatory (Russell et al., 2010). This observation revealed some of the first merger shocks detected since the Bullet Cluster. Being less massive and thus cooler than the Bullet Cluster, the gas in Abell 2146 is better suited for observations in the Chandra band, so that surface brightness and temperature maps can be produced in unprecedented detail (Russell et al, in prep). In this paper, we describe the observable consequences of magnetic fields of different strengths on X-ray observations of merging clusters similar to Abell 2146.

The X-ray features are primarily determined by the mass profiles of the subclusters, their relative velocity, and the geometry of the merger. These parameters were constrained through an extensive parameter study in Chadayammuri et al. (2021) (henceforth Paper I). In this paper, we explore the role of adding magnetic fields with properties expected from observations. We make predictions not only for X-ray maps, but also for the Faraday rotation. Section 4.2 describes the simulation setup. We show our results for the effects of mergers on the magnetic field, and of the magnetic field on observables, in Section 4.3. We discuss caveats and future work in Section 4.5, and wrap up with conclusions in Section 4.6.

## 4.2 The Simulation Setup

We run a suite of idealized simulations with a GPU-accelerated Adaptive MEsh Refinement code, GAMER-2 (Schive et al., 2017). The simulations are run in boxes of $(14{\rm Mpc})^3$, split first into 128 cells per side and then adaptively refined up to 4 times, yielding a maximum resolution of 6.8 kpc. We also re-ran the $\beta = 100$ simulation with three additional levels of refinement to understand resolution effects, see the Appendix 4.4.

We initialise two cluster halos with dark matter and non-radiative gas. The halos are described by the super-NFW profile (Lilley et al., 2018):

$$\rho(r) = \frac{3M}{16\pi a^3}\frac{1}{(r/a)\times(1+r/a)^{5/2}} \tag{4.1}$$

where M is the total mass of the halo, and the scale radius $a$ relates to the half-mass radius as $a = R_e/5.478$. The major advantage of this over the more conventional NFW profile (**?**) is that the total mass converges as $r \to \infty$. For a given total mass of the halo, we assign a fraction $f_{\rm gas} = 0.17$ to the gas mass, and the remainder to the dark matter profile. The primary halo has a virial mass of $5 \times 10^{14} M_\odot$ and the secondary is $1.6 \times 10^{14} M_\odot$. The best fit dark matter concentration for the primary halo was found to be $c_1 = 5$ in Paper I. The concentration of the secondary halo could not be constrained; here, we set it also to

$c_2 = 5$. The impact parameter of the merger was constrained to be around 100 kpc, and the relative velocity 1200 km/s.

The gas density profile is modeled parametrically using the formulation of Vikhlinin et al. (2006):

$$n_p n_e = n_0^2 \frac{(r/r_c)^{-\alpha}}{(1 + r^2/r_c^2)^{3\beta-\alpha/2}} \frac{1}{(1 + r^\gamma/r_s^\gamma)^{\epsilon/\gamma}} \tag{4.2}$$

The normalisation $n_0$ is set so that the gas fraction within $R_{200}$ matches the universal average of 0.17. Through a parameter exploration described in more detail in Paper I, we found that the subclusters in Abell 2146 both initially had cool cores, and are well described by $\alpha = 2, r_s = 0.6 r_{vir}, r_c = 0.1 r_{vir}, \beta = 2/3, \gamma = 3$ and $\epsilon = 3$.

The magnetic field setup is described in more detail in Brzycki & ZuHone (2019, and references therein); here, we provide a brief summary. The field is initialised to be tangled, i.e., randomly oriented, with constant-$\beta$, meaning that in every radial aperture, the ratio between the magnetic and thermal pressures is roughly constant. Note that this is different from the gas density slope $\beta$, which we will no longer refer to in this work. The tangled field has a Kolmogorov power spectrum, $E(k) \propto k^{-5/3}$ with low and high scale cutoffs at 10 and 1000 kpc, respectively. The initial field is "cleaned" so as to remove any divergence, making $\nabla \cdot \vec{B} = 0$. We consider magnetic field strengths corresponding to $\beta$ = 200, 100 and 50; note that higher values mean weaker fields.

Since the initial magnetic field is random, generating a fresh set for every $\beta$ would produce different realisations of a random distribution. We want to isolate the effect of increasing the magnetic field strength, not to confound it with slightly different initial distributions. Therefore, we only generated a random field for the weakest case, $\beta = 200$. Since $\beta \propto 1/P_B \propto B^{-2}$, we multiplied the field strength by $\sqrt{2}$ for $\beta = 100$ and by 2 for $\beta = 50$. The magnetic field is evolved with the magnetohydrodynamic (MHD) approximation, conserving mass, momentum and magnetic flux (where the equations assume Gaussian units):

$$\frac{\partial \rho}{\partial t} + \nabla \cdot (\rho \vec{v}) = 0, \tag{4.3}$$

$$\rho \frac{\partial \vec{v}}{\partial t} + \rho(\vec{v} \cdot \nabla)\vec{v} = \frac{(\nabla \times \vec{B}) \times \vec{B}}{4\pi} - \nabla P + \rho \vec{g}, \tag{4.4}$$

$$\frac{\partial \vec{B}}{\partial t} = \nabla \times (\vec{v} \times \vec{B}), \tag{4.5}$$

where $\rho$ is the gas density, $\vec{v}$ its velocity, $\vec{B}$ the magnetic field, $\vec{g}$ the gravitational acceleration, $P$ thermal pressure, $\nabla$ the gradient operator and $\frac{\partial}{\partial t}$ with respect to time.

Paper I concluded that the merger was fairly close to the plane of the sky, $\theta \sim 30°$; for

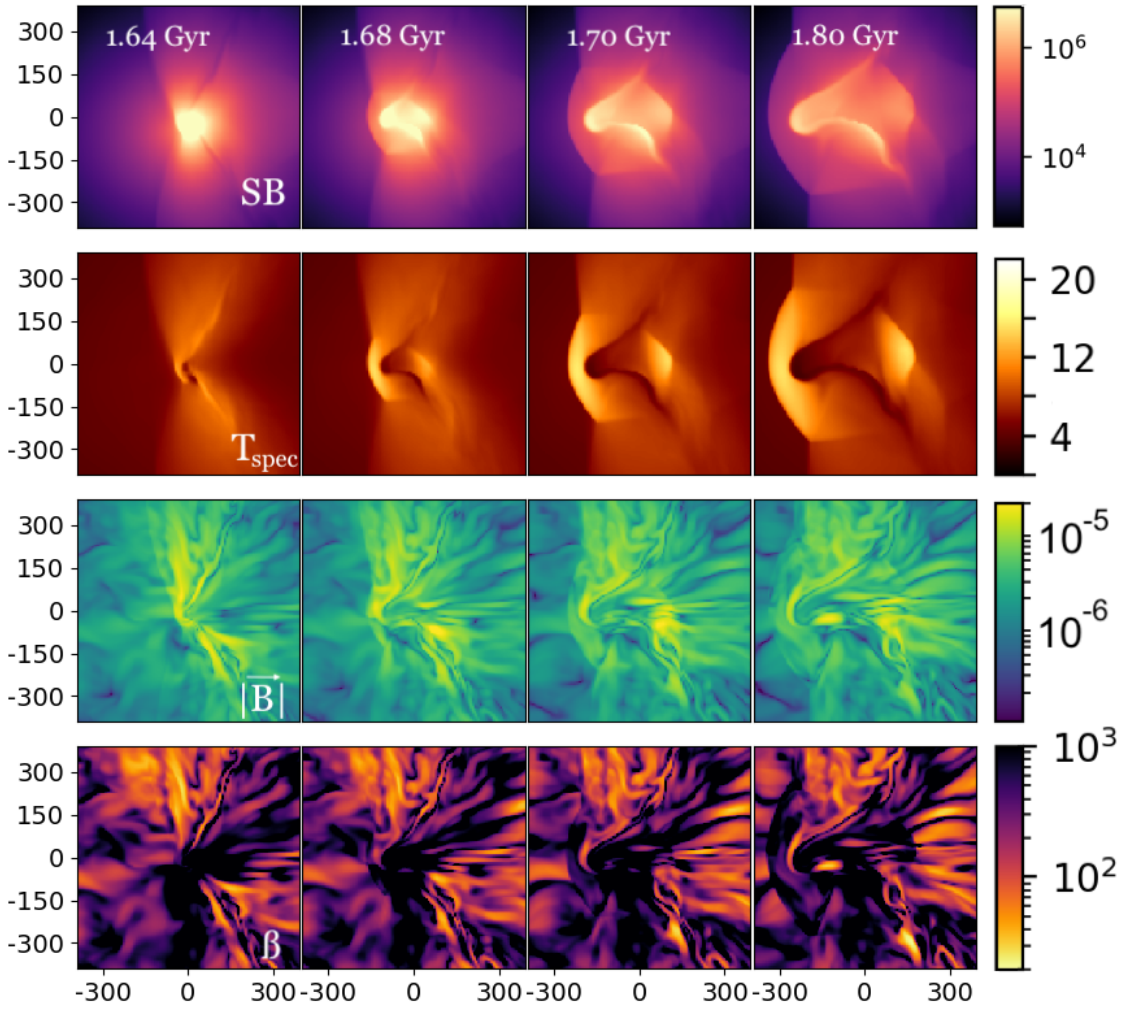


Figure 4.1: Slices of emission-weighted surface brightness (top), spectral-weighted temperature (second), slice of magnetic field strength $\vec{B}$ (third) and slice of $\beta = P_{\rm th}/P_B$ (bottom row) around pericenter passage for an initial average $\beta_i = 200$. The contact discontinuity is seen as a low surface brightness, high temperature, V-shaped feature initially ahead of the subcluster core, but connecting with it by pericenter passage at $t = 1.50$ Gyr. The magnetic field gets most amplified in the wake of the secondary subcluster, on the side closer to the core of the primary cluster. Here, $\beta$ is of order 10, so the magnetic field is dynamically significant. Also in the wake of the subcluster there are ripples, which look like KHI.

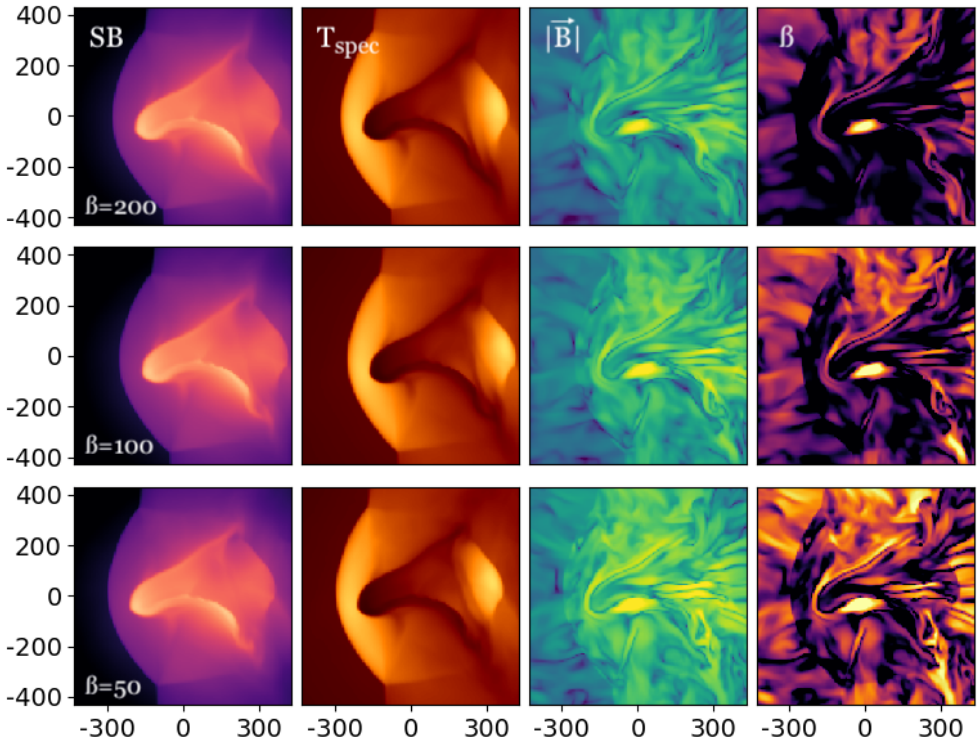


Figure 4.2: Comparison of emission-weighted surface brightness (left column), spectral-weighted temperature (second column), slice of magnetic field strength (third column) and slice of $\beta$ (right column) for $\beta_i = 200$ (top row), $\beta_i = 100$ (middle row) and $\beta_i = 50$ (bottom row). The colorbars are identical to Fig. 4.1. The ripples in the SB and temperature maps correspond to regions of ripples in the magnetic field. They are more prominent for stronger initial magnetic fields, because while magnetic tension can slow the growth of instabilities, in this case, the randomness of the seed field is also the only source of perturbations in the otherwise smooth cluster gas.

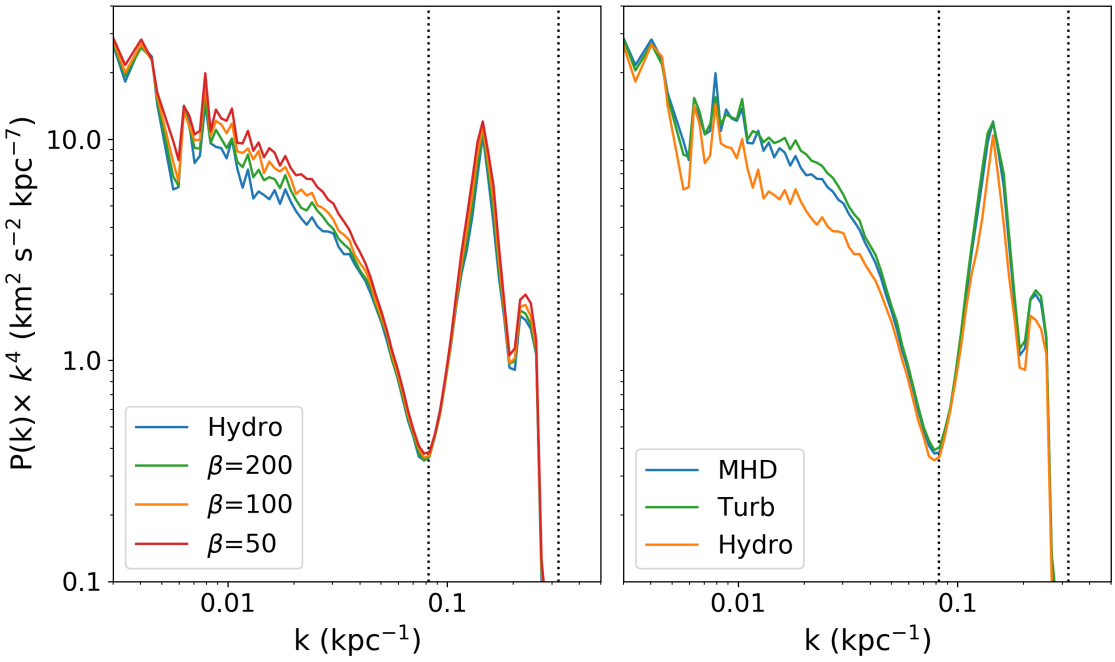


Figure 4.3: *Left:* Power spectra of the velocity in the hydrodynamic and three MHD simulations. *Right:* Power spectra of the velocity for $\beta = 50$ MHD (blue), seed $\beta = 50$ with $\vec{B}$ switched off at 0.7 Gyr to simulate turbulence (green) and the hydrodynamic case (orange). The power spectra are scaled by $k^4$ to highlight the differences. The scale $k = 1/l_{\rm kpc}$. The power in motions increases on scales of 20-100 kpc as the magnetic field gets stronger ($\beta$ decreases). The power in the hydrodynamic case is lower than for MHD, while that for turbulence without magnetic fields is higher. The vertical lines indicate the resolution limit $1/\Delta x$ and $1/2\Delta x$.

convenience, we present most of our results projected along the z-axis, i.e., onto the plane of the merger. The projected temperature map is computed using the spectroscopic-like weighting $w \propto \rho^2 T^{-3/4}$ (Mazzotta et al., 2004).

## 4.3 Results

### 4.3.1 Evolution of Magnetized ICM during Cluster Merger

Fig. 4.1 shows the evolution of the central 1 Mpc of the merging system for $\beta_i = 200$ in the 0.12 Gyr surrounding pericenter passage. The top row shows projections of the surface brightness, the second row projections of the spectral-weighted temperature, the third row slices of the magnetic field strength and the bottom row slices of $\beta$. The evolution of the gas is described in detail in §3.2 of Paper I; here we provide a brief summary as relevant to the evolution of magnetic fields. As the subcluster falls into the potential of

the primary halo from the right, the low density, high entropy gas from the outskirts of the two subclusters forms a contact discontinuity, an interface between the gas associated with each subcluster; the gas near this discontinuity is the first to be compressed during the merger. The core of the subcluster moves faster than the contact discontinuity, and the gas it displaces along its path moves out along the discontinuity. Pressure is almost continuous across the discontinuity, so the pressure gradient is the same on both sides, but the density differs, so gas on the low density side is accelerated to high speed in the direction parallel to the interface, creating a strong shear along it. This shear powers the growth of velocity fluctuations, initially created by Alfven waves from the tangled magnetic field, through the KHI. The compression and KHI also amplify the magnetic field along the interface, decreasing the plasma $\beta$ from initial values of 200 to $< 20$. The bow shock forms close to pericenter passage and quickly overtakes the leftward travelling shock that was initially launched from the contact discontinuity. Meanwhile, the low-entropy subcluster core forms a second contact discontinuity, referred to henceforth as the merger cold front. It is within this cold front that the magnetic field gets the most amplified, as seen in the third row. Ram pressure stripping sweeps gas from the subcluster core, creating an obstruction to the sub cluster gas in its wake, which gives rise to the upstream shock. This does not correspond to a particularly strong feature in the magnetic field structure, but most of the field amplification does happen in the region between the cold front and the upstream shock, where the gas is colder and denser. However, the $\beta$ here is not as low as along the initial discontinuity, since the thermal pressure is also rather large. The key morphology of Abell 2146 is reproduced 0.10 Gyr after pericenter passage.

These simulations show that merging clusters need to be seeded with a realistic level of turbulence in order for KHI to produce potentially observable structure in the wake of the secondary subcluster. Conversely, this means that the observed structure of the wake provides an opportunity to constrain the level of turbulence in the merging subclusters. MHD effects on these features, although present, will be difficult to separate from the level of seeded turbulence - at least in the absence of other data to constrain the strength of the magnetic field. In cosmological simulations, this can likely be achieved self-consistently, since primordial magnetic fields are frozen into the plasma well before they start collapsing into halos, get amplified through turbulence associated with collapse, accretion and mergers, and end up with a random, Kolmogorov-like spectrum; this is indeed seen in past studies (e.g., Dolag et al., 2005; Vazza et al., 2009, 2011).

### 4.3.2 KHI ripples behind the subcluster

One obvious effect of adding magnetic fields is the appearance of KHI-like ripples in the wake of the infalling cluster. We see that the interface associated with this instability is the contact discontinuity that forms in the early stages of the merger, which appears to extend along the edges of the bullet-like cold front in its wake. The gas in this discontinuity is

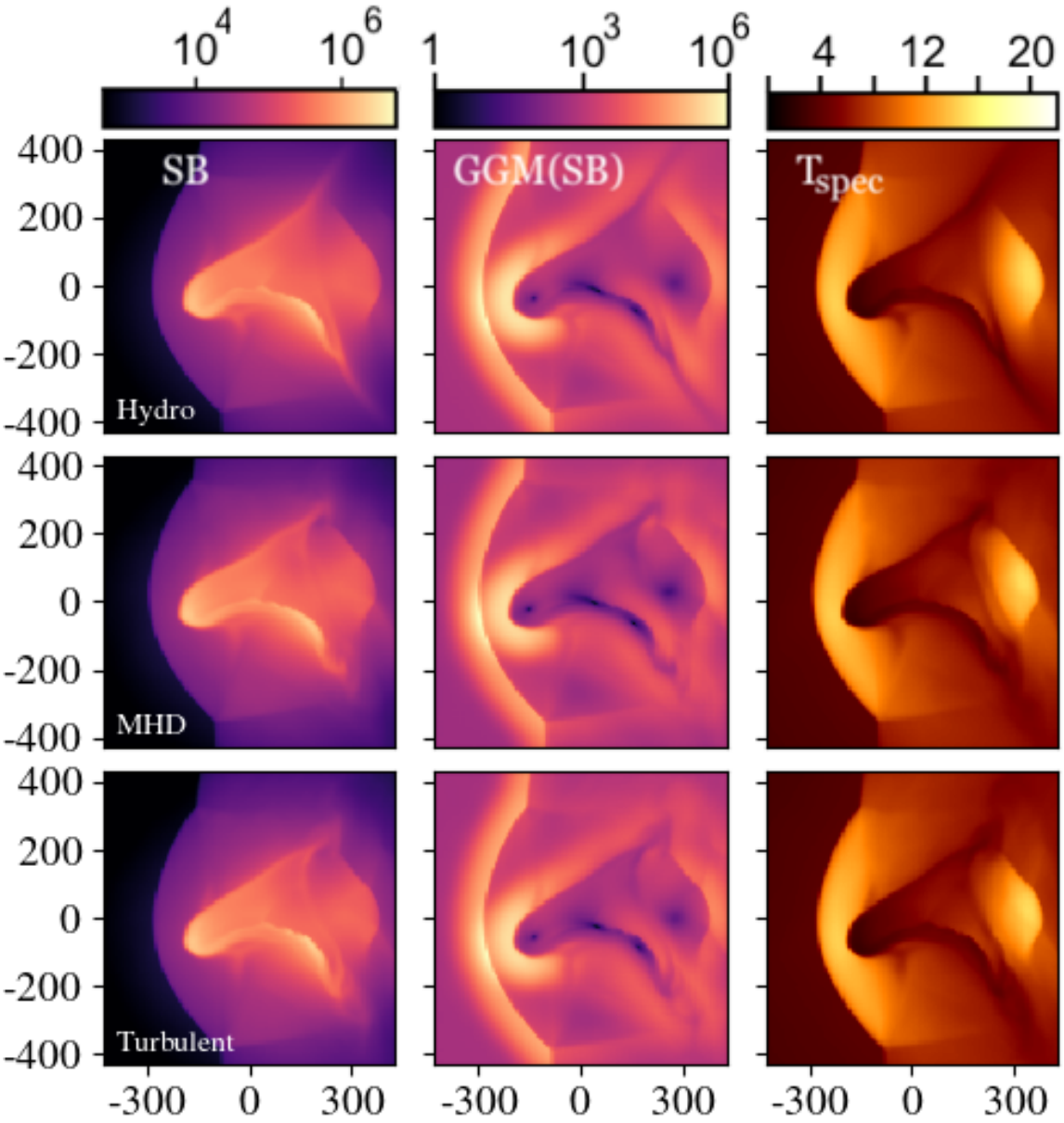


Figure 4.4: Surface brightness (left), Gaussian Gradient Magnitude (GGM) of the surface brightness (middle) and temperature (right) for the simulations with only hydrodynamics (top), MHD with $\beta = 50$ (middle) and a seed $\beta = 50$ to generate turbulence, with the magnetic fields turned off at 0.7 Gyr (bottom). The bottom row shows what would happen if there were turbulent fluctuations equivalent to those in the middle row, but there were no magnetic fields shaping their growth during the merger. The GGM highlights sharp features in the surface brightness image, making it easier to identify the ripples in the subcluster wake.

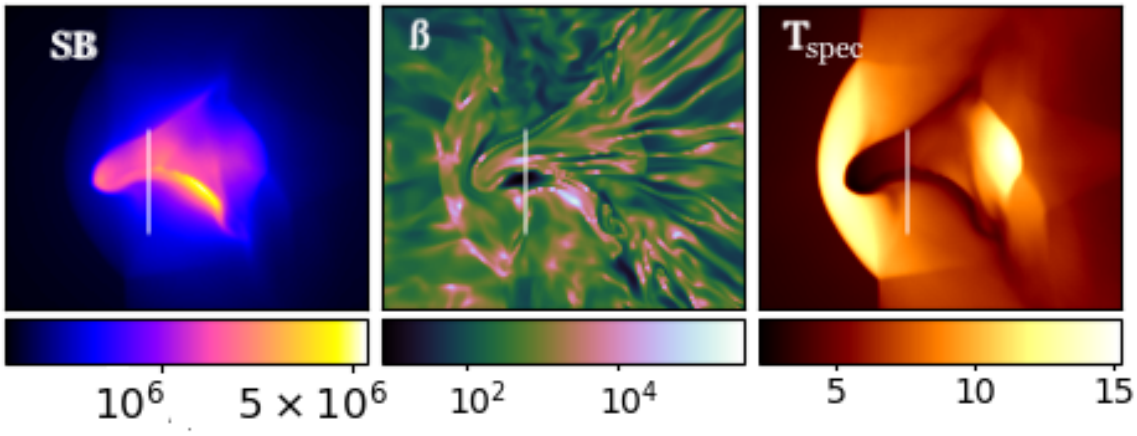


Figure 4.5: Projection of surface brightness (left), $\beta$ (middle) and temperature (right) for the simulation with $\beta_i = 100$. The vertical lines were chosen to pass through the region of lowest $\beta$, i.e., where the magnetic field is most dynamically significant.

pushed upstream of the subcluster core and away from the merger axis, creating a shearing layer. Perturbations in density, velocity, pressure, etc. along this shearing layer are expected to grow by the KHI. Fig. 4.2 shows the surface brightness, temperature, magnetic field strength and plasma $\beta$ for simulations with different seed field strengths, and confirms that the ripples are more prominent for stronger magnetic fields. While the field strength and $\beta$ show that the amplitude of the KHI ripples increases along the discontinuity with distance from the cool core, they are more visible closer to the core where the gas is denser and more luminous.

We quantify the relative prominence of the KHI ripples using the velocity power spectrum. We interpolated each component of the velocity $(v_x, v_y, v_z)$ of the gas within a cube of side 0.5 Mpc, centered on the potential minimum, onto a uniform grid of size $(256)^3$. The velocity grid was filtered with a Hanning window function to mitigate boundary effects in the Fast Fourier Transform (FFT). The FFT then yielded a 3D power spectrum, which was then binned into a 1D power spectrum for that particular velocity component. The left panel of Fig. 4.3 shows the power spectrum of the total velocity, $P(k) = P_x(k) + P_y(k) + P_z(k)$, multiplied by $k^4$ to highlight the differences. The peak at high $k$ corresponds to the resolution limit, $\Delta x < 1/k < 2\Delta x$. The magnitude of the power spectrum increases with decreasing $\beta$, i.e. it increases along with the strength of the magnetic field.

Our result, that the amplitude of KHI modes is greater with a stronger magnetic field, is contrary to earlier studies using uniform magnetic fields (e.g., Dursi & Pfrommer, 2008; Zuhone et al., 2011). On the other hand, simulations of a rigid body in a turbulent magnetic field did find an amplified, turbulent magnetic wake forming behind the perturber (Asai et al., 2007; Takizawa, 2008). When the magnetic field is uniform, we isolate the effect

of magnetic tension, which resists the bending of a fluid element into eddies. Random magnetic fields, on the other hand, generate the seed velocity fluctuations themselves; the magnetic field lines want to be straight, but as they straighten, field energy is converted to kinetic energy, so there is overshoot and Alfven waves are produced in the cluster gas. Alfven waves produce shearing velocities, similar to unstable KHI modes; as such, they provide effective seeds for KHI. Figs 4.2 and 4.3 suggest that the effect of the stronger seed fluctuations outweighs the resistance to KHI due to magnetic tension in the draped field layer.

To isolate the effect of turbulence from magnetic fields, we ran a simulation for $\beta_i = 50$ but turned the magnetic fields off at $t = 0.7$ Gyr. This gives enough time for the magnetic fields to generate velocity fluctuations in the cluster gas, but is well before the merger starts amplifying the magnetic field in the subcluster. Then we see what happens in the wake of the cluster, with the fluctuations seeded - but no longer affected - by magnetic fields. We chose the strongest seed field so that the effects are more visible.

The resulting maps are shown in Fig. 4.4. The top panel shows the hydrodynamic simulation, the middle panel MHD with $\beta = 50$, and the bottom panel started with the same magnetic fields as the middle panel, but these are switched off at 0.7 Gyr once they have seeded a random field of fluctuations analogous to turbulence. The left column shows the surface brightness, and the right column the spectral-weighted projected temperature. The middle column takes the Gaussian Gradient Magnitude of the surface brightness (Walker et al., 2016), which highlights sharp features and makes the ripples much more visible by eye. The velocity power spectra for the three simulations are shown in the right panel of Fig. 4.3.

The ripples are much less visible in the hydrodynamic case. As we suspected, however, they do show up in the bottom panel, where the turbulent fluctuation spectrum is seeded but the magnetic field then turned off. Lastly, the ripples have already evolved to the point of dissipation in the bottom panel, whereas in the middle panel they are still growing in size; in other words, if the magnetic fields continue to act throughout the simulation, they do suppress the growth of the fluctuations. Correspondingly, the hydrodynamic simulation with turbulence seeded by magnetic field has the highest normalisation for the velocity power spectrum on $\sim 10$ kpc scales, the hydrodynamic simulation with no seeded turbulence has the lowest, and the MHD run lies in between the two.

### 4.3.3 Surface brightness channels

Werner et al. (2016), in their $500ks$ *Chandra* observations and numerical simulations of sloshing cold fronts in the Virgo Cluster, found bands 10-15 kpc across with lower surface brightness that corresponded to regions of high magnetic field strength. The Virgo cluster is just 16.1 Mpc away from us, whereas Abell 2146 has an angular diameter distance almost 50 times greater. Therefore, a feature would have to be 50 times larger to be as

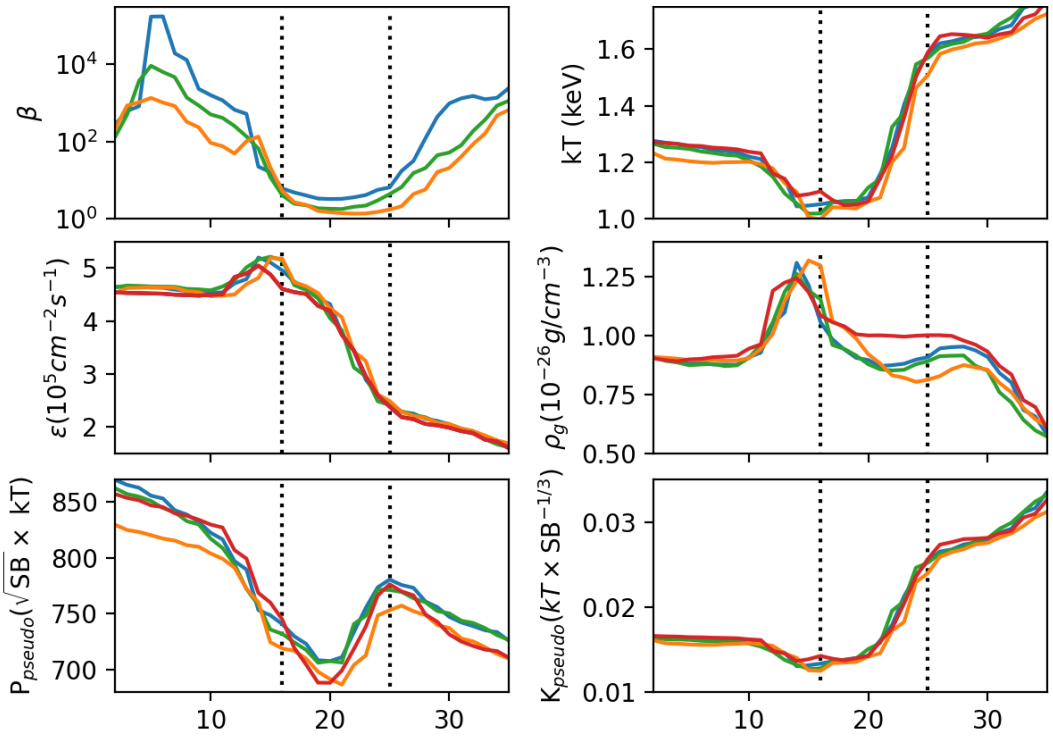


Figure 4.6: Profiles for the plasma $\beta$, projected temperature, photon emissivity, gas density, pseudo-pressure and pseudo-entropy along the line shown in Fig. 4.5, for $\beta$ = 200 (blue), 100 (green), 50 (orange) and the hydrodynamic case (red).The dotted lines mark the region where the magnetic field is the most amplified. The $\beta$ profiles show that the field amplification saturates in this region, as also seen in the RM plots. The density in the plane of the merger is significantly lower in the presence of magnetic fields than without them; however, this effect is entirely erased in projection. Furthermore, the dip in surface brightness, and corresponding adiabatic increase in temperature, also occur without magnetic fields, so that detecting such a dim "channel" does not imply magnetic fields.

well resolved in Abell 2146 as it is in Virgo. However, the scenario in Abell 2146 is also different - the cold fronts are associated with an ongoing merger, rather than sloshing; the much stronger bulk motions could, in principle, amplify magnetic fields a lot more. Wang et al. (2016), for example, claim to see such a channel in the merging cluster Abell 520. Here, the surface brightness dip is $\sim$400 kpc long, and aligns with the northern edge of the bridge behind the Bullet-like cool-core.

Fig. 4.5 shows the projected surface brightness, $\beta$ in the plane of the merger, and projected temperature for the $\beta_i = 100$ simulation, with a vertical line in each passing through a region of lowest $\beta$. Fig. 4.6 then shows the 1D profile along the highlighted line for each of these quantities, as well as the density, pseudo-entropy $P = \sqrt{SB} \times k_B T$ and entropy index $K = k_B T \times SB^{-1/3}$. In the distance range 15 - 25 kpc (marked with dashed vertical lines), where the magnetic field is the strongest, the temperature, density, pressure and photon emissivity all dip. The red line shows the hydrodynamic case, with no magnetic fields. The dip is just as visible in this case. The only property where the MHD profiles are significantly different is the slice of the density; this effect is washed out in projection, because the region of low $\beta$ is only a few kpc wide. This suggests that the dim "channel" seen in Abell 520 can be explained hydrodynamically, without invoking the need for magnetic fields.

### 4.3.4 Rotation Measure Maps

Fig. 4.7 shows the Faraday rotation measure for hypothetical background radio sources for the MHD simulations with the magnetic field increasing downward, so that $\beta = 200$ in the top row and 50 in the bottom, from the initial conditions the left column, through pericenter passage, and 0.1 and 0.3 Gyr later on the right. Again, the rotation measure is proportional to the integral of the electron density times the component of the magnetic field parallel to the line of sight. If the merger is in the x-y plane, and we view it side-on, then this is $B_z$ integrated along the $\hat{z}$ axis. Since observations of RM are necessarily local, we also show the observable quantity $\sigma_{RM} = \sqrt{< RM^2 > - < RM >^2}$, which is the standard deviation of the RM computed along different sight-lines (e.g., Bonafede et al., 2010; Böhringer et al., 2016).

The initial values of $\sigma_{RM}$ scale linearly with the seed field, as expected. The kinetic energy of bulk motions amplifies the magnetic fields, so that the RM signal peaks at pericenter passage at $\sim 3 - 4\times$ the initial value. The extent of field amplification is lower for stronger seed fields. This is the phenomenon of saturation - field amplification occurs when kinetic motions stretch magnetic field lines out; however, at some point, the magnetic pressure is so high that kinetic motions are unable to stretch the field lines any further. The amplification is, however, transient. Just 0.1 Gyr after pericenter passage, $\sigma_{RM}$ in this region has fallen by 40%, most of the amplification at the interface of high shear velocity on the top and bottom edges of the bridge connecting the cool core remnants. Within

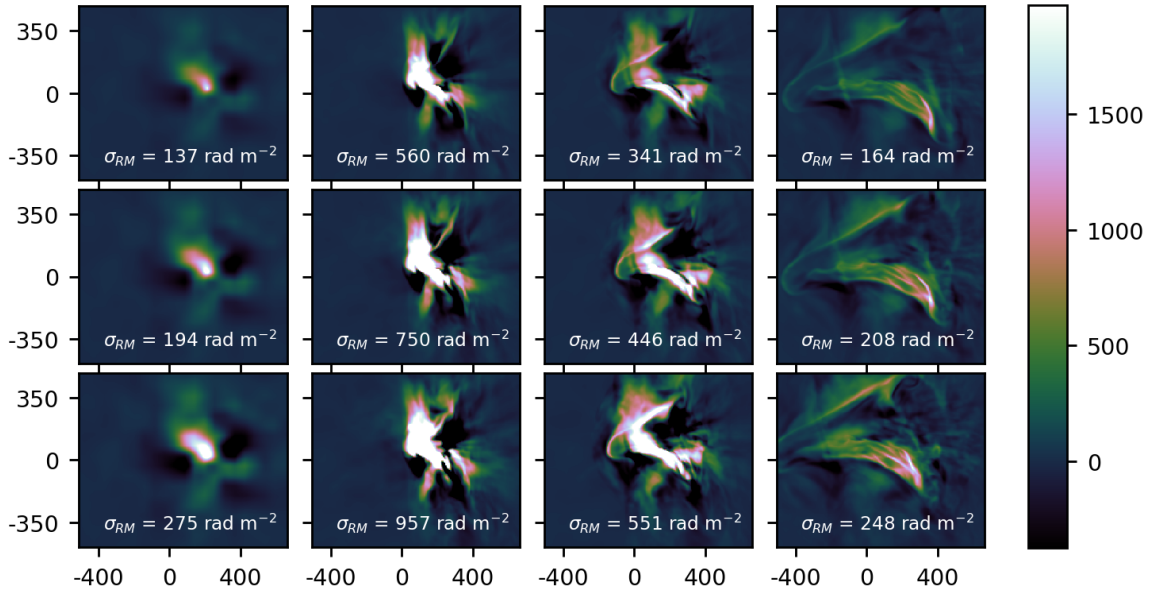


Figure 4.7: Faraday rotation measure (RM) in rad m$^{-2}$ for $\beta = 200$ (top), $\beta = 100$ (middle) and $\beta = 50$ (bottom). From left to right, the columns show the initial conditions, pericenter passage, and 0.1 Gyr and 0.3 Gyr after pericenter passage. The magnetic field gets significantly amplified ($\sim 4-5\times$) in the central 500 kpc right after pericenter passage. This amplification is temporary, and the field reaches $2-3\times$ the initial value 0.1 Gyr post pericenter passage, the dynamical phase most consistent with observations of Abell 2146. The amplification is localised to the regions of large bulk motions, and remains close to 0 everywhere else.

another 0.2 Gyr, $\sigma_{RM}$ is almost the same as before the merger

Interestingly, even though the shearing motions are preferentially in the $x$-direction, corresponding to the initial velocity of the two halo centres, the field amplification is nearly isotropic; the RMS values of the $x$, $y$ and $z$ components of the magnetic field all grow by a factor of 1.5-2. This suggests that the Faraday rotation measure (RM) should be relatively insensitive to the viewing direction. Fig. 4.8 shows the RM map for $\beta_i = 100$, $t = 1.80$ Gyr, for three different viewing directions, all consistent with the constraints in Paper I. Even setting $\theta = 30^\circ$ reduces the measured $\sigma_{RM}$ by less than 18 $\%$.

Since RM measurements are done on small scales corresponding to the angular sizes of background radio sources, they should be interpreted with extreme caution around merging cluster cores. Fig. 4.7 also shows, however, that outside the central 100 kpc, the plasma $\beta$ remains similar to its initial value. Anomalously high RM measures are therefore an indicator of strong shearing motion. Conversely, if the goal is to measure the magnetic fields in relaxed clusters, a safe option might be to exclude the central region including any core remnants.

## 4.4 Resolution effects

Fig. 4.9 shows the effect of increasing resolution on the evolution of the merger. All snapshots are at $t = 1.80$ Gyr, when the separations between the shock and cold fronts best match observations, and the initial average $\beta$=100. The top row shows the surface brightness at 0.3-7 keV, the second the Mazzotta-weighted temperature, and the bottom shows $\beta_{proj}$, discussed below. From left to right, the resolution improves from 6.8 to 3.4 to 1.7 kpc. Observationally, we are limited by the *Chandra* PSF of 1", which corresponds to 3.8 kpc at the redshift of Abell 2146. Therefore, the maps are all smoothed by a Gaussian of width 3.8 kpc.

In agreement with earlier studies (e.g., Zuhone et al., 2011; ZuHone et al., 2015b), greater resolution creates more turbulent structure in the temperature as well as surface brightness maps. Perturbations smaller than the simulation resolution get erased, a phenomenon called numerical viscosity; this applies both to seed fluctuations on small scales, and turbulence that cascades from higher to smaller scales. As a result, the KHI more efficiently grows eddies along the bridge between the cool core remnants, where the shear velocity is the highest.

We note, however, that all the features in the higher-resolution runs also exist at lower-resolution, they are simply not as developed. This points further to the fact that the difference stems from reduced numerical viscosity.

The bottom panel of Fig 4.9 shows the projected quantity $\beta_{\rm proj}$, the ratio of the projected thermal and magnetic pressures, each weighted by the square of the density, which decides their emissivity. We see that the new structures visible at higher resolution do not coincide

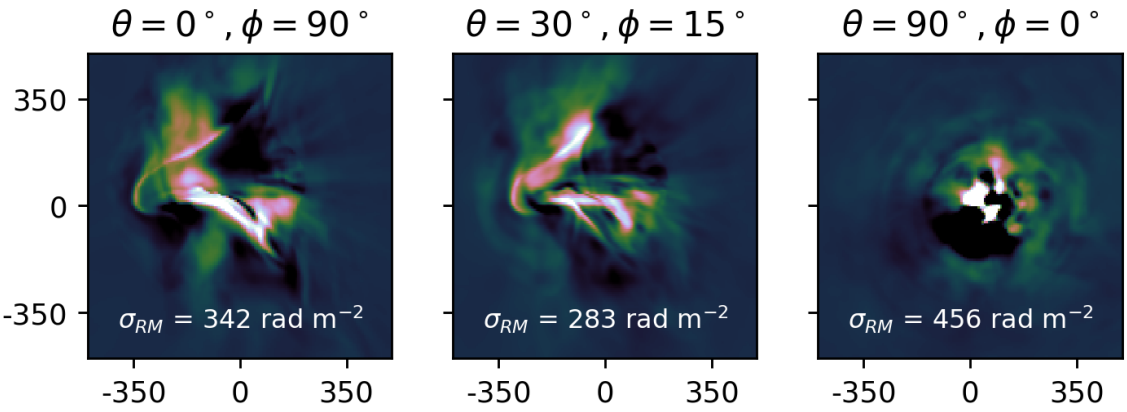


Figure 4.8: The effect of viewing direction $(\theta, \phi)$ on the Faraday rotation measure (RM). The colorbar is identical to Fig 4.7. Following convention, $\theta$ is the angle between the observer and the y-z plane, and $\phi$ between the observer and the x-z plane. These plots are for the same simulation as the top row in Fig. 4.7, at the snapshot in the third column. For $\theta = 0$, changing $\phi$ has no effect on RM. The middle panel shows ($\theta = 30°, \phi = 15°$), the viewing direction most compatible with observations of Abell 2146, the RM varies by less than $18\%$. If you look perfectly down the barrel (right), i.e. along the merger axis, RM is boosted by $33\%$; this is largely due to the greater projected density.

with regions of low $\beta$, i.e. they are not due to the displacement of gas by magnetic pressure. Eddies in $\beta_{\rm proj}$ instead trace regions of the highest shear velocity, which indeed is what amplifies magnetic fields. It also grows KHI. In other words, regions of low $\beta$ also have KHI eddies, but the other way around is not necessarily true. Therefore, dips in the surface brightness and temperature maps are not necessarily evidence for the presence of magnetic fields.

## 4.5 Discussion

Reinterpreting previous studies of KHI in merging clusters Previous studies, such as Vikhlinin et al. (2001), use the absence of KHI ripples at the leading edge of a cold front as evidence for a strong magnetic field. This reasoning was based on theoretical work using uniform magnetic fields (e.g., Dursi & Pfrommer, 2008). Instead, we highlight that magnetic fields are inherently turbulent in nature - they grow by turbulent amplification over the course of a cluster's history, and generate Alfven waves along the way. This point has already been made in both theoretical (e.g., Subramanian et al., 2006; Donnert et al., 2018) and observational studies (e.g., Domínguez-Fernández et al., 2019; Stasyszyn & de los Rios, 2019). In the context of merging clusters, therefore, we should neither treat the magnetic fields as uniform, nor forget that turbulence that amplifies magnetic fields also seeds the instabilities which grow through the KHI. The level of turbulence is determined

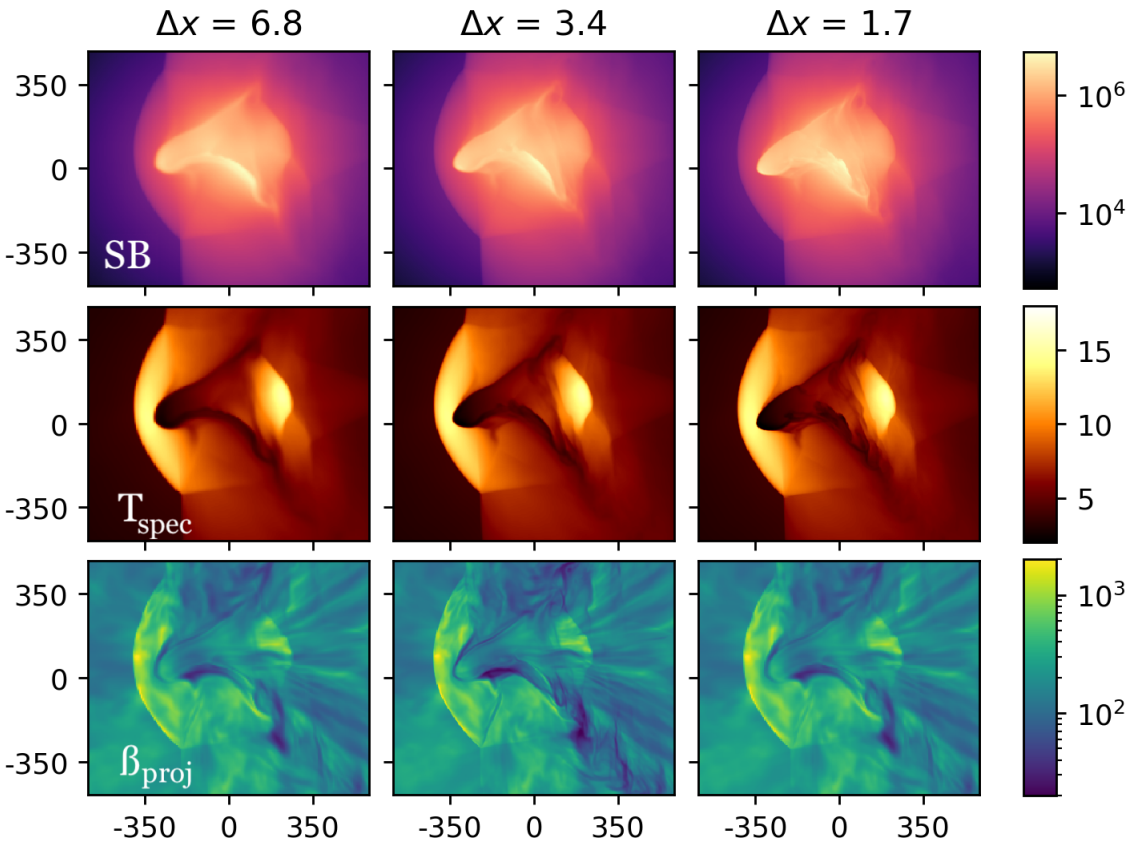


Figure 4.9: The effect of resolution on the surface brightness (top), projected temperature (bottom) and projected $\beta$ (bottom) of the system in the presence of magnetic fields with $\beta_i$=100. $\beta_{\rm proj}$ is the ratio of the projections of the thermal and magnetic pressures, respectively, each weighted by the square of the gas density, which affects their emissivity and therefore visibility. The number of levels of refinement goes from 4 on the left to 6 on the right, resulting in the specified resolutions. The simulations are shown at t = 1.80, where the shock and cold front separations match observations. The higher resolution runs have lower numerical viscosity, and allow smaller-scale fluctuations to grow, resulting in more turbulent structure. Crucially, the additional features seen in temperature and surface brightness at higher resolution are not regions of low$\beta$, suggesting that they are a result of turbulence rather than magnetic fields.

mainly by the recent growth history of a system. The amplitude of the KHI in a merging system might serve as a probe of the level of turbulence, particularly for high $\beta$, when the field has little direct impact on growth of KHI.

Second, relatively strong magnetic field can suppress the growth of KHI in these systems, but the effect is modest for realistic field strengths, which will make it hard to untangle such suppression from the impact of the initial level of turbulence. In our simulations, instabilities do not form at the leading edge of the cold front even when we seed turbulence using $\beta_i = 50$ and then turn magnetic fields off entirely, as seen in the bottom row of Fig. 4.4. Therefore, the absence of KHI at the leading edge of a cold front doesn't seem to require the presence of magnetic fields. Instead, it could be due to the finite thickness of the boundary layer, as described in Churazov & Inogamov (2004).

The discerning power of Faraday Rotation Johnson et al. (2020) shows that the Faraday rotation measure can only constrain the magnetic field strength of a cosmologically simulated cluster to within a factor of 3, due to inhomogeneities in ICM density and the unknown scaling between $\beta$ and $P_{\rm th}$. In our study, for example, we have assumed that the magnetic pressure is a constant fraction of the thermal pressure in the initial conditions, whereas the causal relationship is between magnetic and turbulent pressure; the constant relation between turbulent and thermal pressure is a simplifying assumption on our part, albeit with observational support (Govoni & Feretti, 2004; Govoni et al., 2017). Since the RM is always sampled very locally, in small regions with background radio sources along the line of sight, any spatial variation in this $\beta - P_{\rm th}$ relation would be significant.

Beyond MHD Our MHD simulations of the merger in Abell 2146 were conducted to look for observable impacts of magnetic fields, prior to more physically complete simulations to include key transport processes as well. Both thermal conduction and viscosity may have significant impacts on a dynamical event like a merger (c.f., ZuHone et al., 2013, 2015a). However, recent studies have shown that thermal conduction, both isotropic and anisotropic, is likely very strongly suppressed in weakly magnetised plasmas like the ICM (Roberg-Clark et al., 2016). Anisotropic conduction was originally found to cause instabilities such as the heat-flux driven buoyancy instability in cool cluster cores, but interestingly, this appears to be almost entirely countered by anisotropic viscosity (Kunz, 2011; Kunz et al., 2012; Latter & Kunz, 2012) and turbulence (Ruszkowski & Oh, 2010). Our understanding of instabilities in high-$\beta$, low-density plasmas like the ICM is still evolving, and the interactions between them are not fully understood. However, if their net effect were significant, galaxy clusters would look significantly different from how they are currently observed - for example, the magnetothermal instability (MTI) would require cluster outskirts to be isothermal, which they are not. As we continue to unravel the complex effects of plasma instabilities, MHD continues to provide helpful, first-order insights into the role of magnetic fields in the ICM.

## 4.6 Conclusions

We presented magnetohydrodynamic (MHD) simulations with various strengths of the magnetic field for the best-fit dynamical model for the galaxy cluster Abell 2146 obtained in Paper I. The simulations used a tangled initial magnetic field with a constant ratio of thermal to magnetic pressure $\beta$ as a function of cluster-centric radius. We produced maps of the Faraday rotation measure and X-ray observables to search for detectable consequences of such a magnetic field. We found that:

- The merger strongly amplifies magnetic fields in the central $\sim$200 kpc through shearing motions, though only for a brief period of time $\lesssim$0.3 Gyr. This increases the measured Faraday RM by a factor of 4 if our viewing direction is perpendicular to the merger plane, and more if instead the merging clusters have a relative velocity along our line of sight. For the most likely viewing direction towards Abell 2146, this additional boost is $\sim 18\%$.

- In the "wake" of the subcluster, on the top and bottom edges of the "bridge" connecting the cool core remnants, KHI-like ripples form in the MHD simulations. This is because a tangled magnetic field is a source of perturbations in the ICM, which are amplified in the presence of large shearing motions along the interface. The amplitude of the KHI in a merger is sensitive to the initial level of turbulence in the ICM, which also amplifies seed magnetic fields. As a result, the velocity power spectra have higher magnitudes for stronger magnetic fields. This is at odds with earlier observational studies, which suggest that the primary effect of magnetic fields is to stabilise discontinuities against instabilities.

- Inspired by work on a similar merging cluster, Abell 520, we searched for low surface brightness "channels" that could result from the displacement of gas by high magnetic pressure. Whereas we do find a surface brightness dip at a region of very low $\beta$, this does not correlate with $\beta$, and indeed is also produced in the hydrodynamic simulations. The gas in this region does get displaced in the plane of the merger, but the region of low $\beta$ is confined to a thin sheet, $\sim$1 kpc wide, which is not much denser than the surrounding regions of very high $\beta$, so that the effect is entirely lost in projection.

Our results emphasise the need to model turbulence along with magnetic fields to produce realistic galaxy clusters, and the fleeting but strong amplification of the Faraday rotation measure in the centres of merging clusters, even if viewed perpendicular to the direction of the merger velocity. Modelling the efficiency of transport processes, accounting for anisotropy in the presence of magnetic fields, is a promising next step in constraining the plasma microphysics of systems like Abell 2146.

# Chapter 5

# Conclusions and Future Work

## 5.1 Key results

The work done in this thesis addressed three phenomena - AGN feedback, cluster mergers and magnetic fields - at the frontier of our understanding of the intracluster medium (ICM).

Paper I explored the behaviour of AGN-heated gas in the highest resolution cosmological simulation of a galaxy cluster to date, RomulusC. The unprecedented resolution revealed complex thermodynamic structure in the ICM, whereas the SPH code allowed us to trace individual gas particles after they were heated by the AGN (Fig 2.5). The AGN accretion rate in the RomulusC model reduces the accretion rate onto the black hole if the gas around it has significant bulk motions. In practice, this meant that it was fed preferentially by low-entropy gas. Thanks to a brief cooling shutoff to prevent numerical overcooling, particles heated by the AGN quickly left the cluster core, transporting heat out to intermediate radii. Significant mass of low-entropy gas at all radii was found to be radially infalling, replenishing the reservoir that fuelled AGN as well as star formation in the BCG (Fig 2.7). The ICM found to be remarkably resistant to order-of-magnitude changes in AGN activity, and resembles what observers call a "cool-core" cluster. A 1:8 mass ratio, low angular momentum merger, however, breaks this delicate balance (Fig 2.4). The merger initially heats the entire cluster core through a shock (Fig 2.8), removing the low-entropy phase entirely; we infer that there must be continued heating through, e.g., sloshing motions, because the cluster core does not revert to its pre-merger low-entropy state even 2 Gyr after the merger, even though the central cooling time was $\sim$ 1Gyr. This does show up as an elevated velocity dispersion profile outside the central $\sim$15 kpc, which before the merger showed significant tangential motions due to a rotating gas disk in the BCG (Fig 2.9).

Paper II focused on extracting dark matter and dynamical properties of a merging cluster using X-ray, lensing and spectroscopic observations. The parameter study was tailored to the observed system Abell 2146. Our first result was that the BCGs of the

subclusters producing the X-ray features - the shock and cold fronts - were misidentified in the literature. What was called BCG-A, and considered the BCG of the primary cluster, lies in the bullet-like cold front and therefore must be the BCG of the secondary cluster. What was called BCG-B lies near the reverse, or upstream shock, well over 300 kpc away from the cool remnant of the primary cluster core. This means that was was modelled as a single component in the lensing analyses was actually an active merger, and fitting it with concentrations $3.5 < c < 4.5$ characteristic for relaxed systems overestimated the mass significantly. This resolved the existing tension between the lensing mass measurements on the one hand and X-ray, SZ and dynamical measurements on the other. We also showed how high-resolution X-ray images can break the degeneracy between viewing direction and key properties like impact parameter (or, equivalently, angular momentum), dark matter concentration, and relative velocity of the substructures (or, equivalently, the shock strengths). We conclude with best fit mass, dark matter concentrations, cool core strength, impact parameters, relative velocities and viewing directions for Abell 2146.

Paper III used the best-fit model from Paper II, and added magnetic fields in the magnetohydrodynamic (MHD) approximation, with the goal of finding as many signatures as possible of the magnetic field in a merging cluster. First, we produced maps of the Faraday rotation measure (RM), the most common probe of cluster magnetic fields. We found that this is strongly amplified in the central $\sim$100 kpc for $\lesssim 1$ Gyr, and that this amplification is primarily along the axis of the merger. Since the RM is an integrated quantity along the line-of-sight, this means that the measured value depends strongly on the viewing angle. Since the RM is always measured in small apertures, corresponding to the angular size of background sources, this result means that we must be very careful about interpolating cluster-wide field strengths based on local measurements in merging systems. Next, we found KHI features in the contact discontinuity behind the secondary cluster core, separating the ICMs of the two clusters. The literature so far has focused on the effect of magnetic tension in suppressing the growth of instabilities, in particular because early studies modeled magnetic fields as uniform. Instead, if the magnetic fields are tangled - as is expected from turbulent amplification of primordial seed fields - they themselves are a source of perturbations that grow at shearing interfaces. This emphasises the importance of incorporating turbulence into idealised simulations in order to reproduce realistic clusters, and that magnetic field strength cannot be inferred from the observed shapes of gas features alone. The magnetic fields are also expected to affect transport processes, such as viscosity, thermal conduction, and electron-ion equilibration, although these are not modeled in our code.

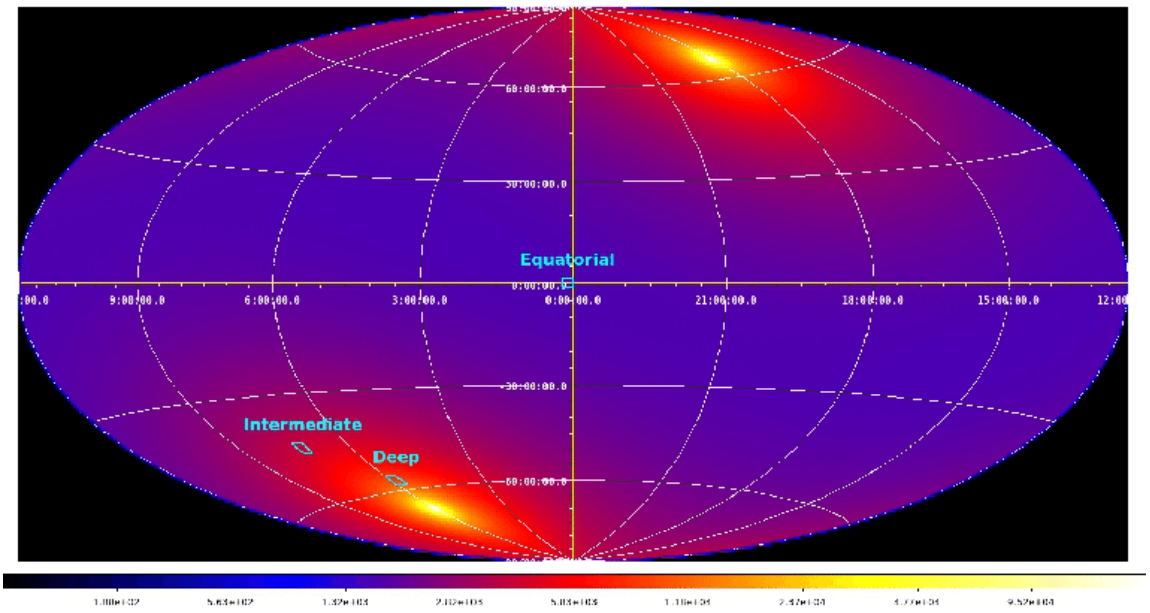


Figure 5.1: The predicted exposure map for eROSITA (Clerc et al., 2018). The poles have the deepest exposures of $\sim 10ks$, the equator the shallowest at $\sim 2ks$, and the intermediate zone will have an average exposure of $\sim 4ks$.

## 5.2 Relevance to Upcoming Telescope Missions

### 5.2.1 Cosmology with eROSITA

Understanding the non-equilibrium behaviour of the ICM is particularly timely as the eROSITA all-sky survey enters its second year, improving on the nearly twenty-year-old data from ROSAT. The survey is well on track to detect 100,000 galaxy groups and clusters out to $z \gtrsim 1$. However, most of these detections will be shallow, since the average depth of the survey is $2.5\ ks$; even the longest observations at the poles will have a depth of $10\ ks$. For comparison, the *Chandra* observations of Abell 2146 used in Paper II were $400\ ks$ long. The effective area of eROSITA, which is proportional to how many photons it gathers per unit time, is $\sim 7$ times larger than that of *Chandra*; even so, the deepest observations will be barely $1/6$ as deep as the ones presented in Paper II. Many of these will be merging systems, and most will not have single-temperature fits, let alone temperature profiles. Lastly, eROSITA has a much lower spatial resolution than telescopes like *Chandra* - 25" averaged over the field of view as opposed to 1". Due to the low spatial resolution and smaller photon counts, converting from X-ray luminosity to total mass will be a very uncertain process. This in turn poses a serious challenge to the way cluster cosmology has been done so far (§1.3).

One promising workaround for this is combining large N-body simulations with vol-

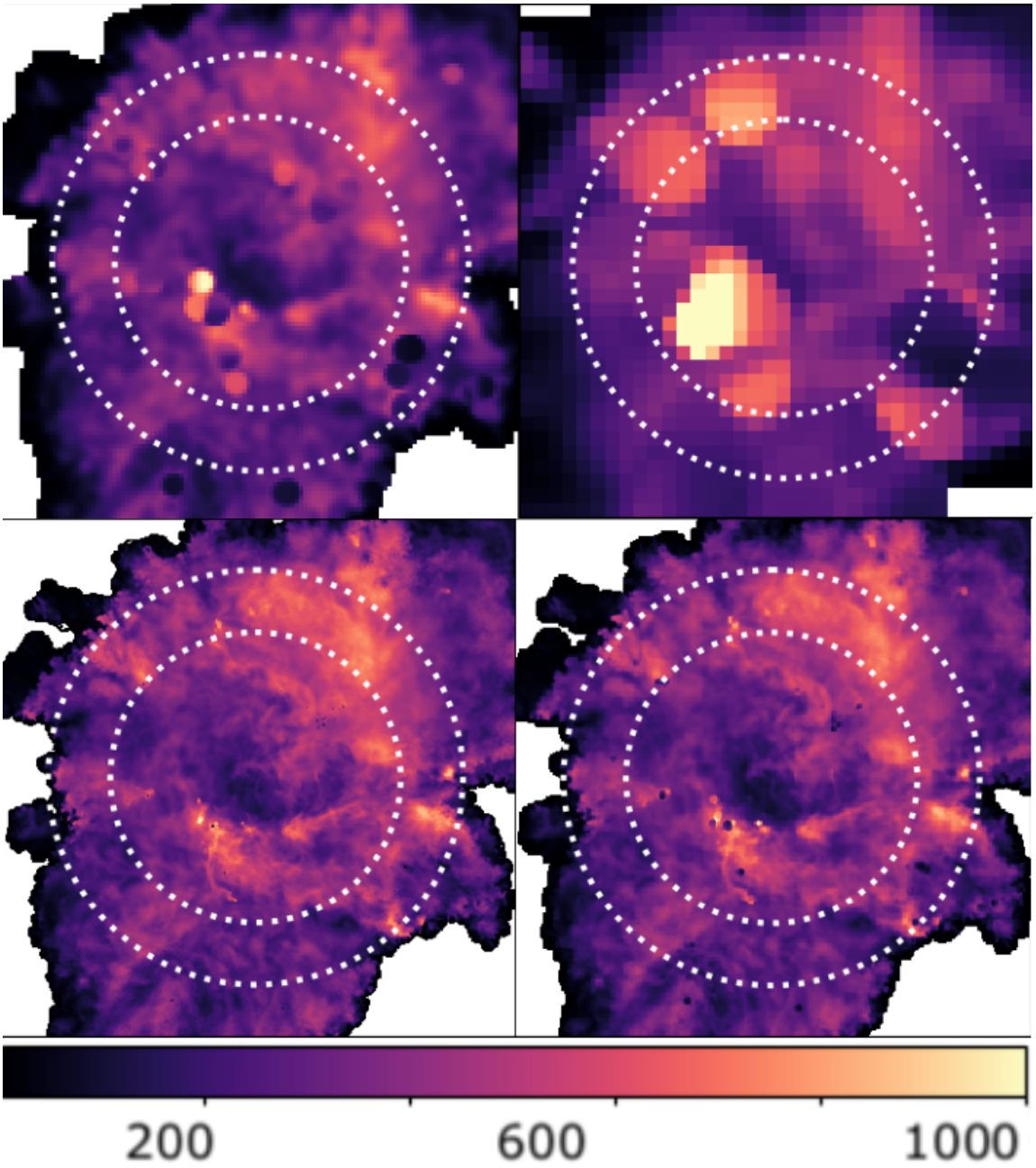


Figure 5.2: Projected maps of the emission-weighted velocity dispersion for a cluster of mass $9 \times 10^{14} M_{\odot}$ extracted from the TNG-300 cosmological simulation, smoothed over the PSFs of XRISM (top) and *Athena* (bottom) (Chadayammuri et al., 2019). The dotted circles show $R_{500}$ and $R_{200}$. Images on the left are placed at z=0.07, while those on the right are at z=0.3, five times further away. Moving the cluster further away means the same physical scale is covered by fewer pixels, limiting the scales down to which we can measure turbulent motions. The colour map shows that turbulent velocities in this region are $\sim 500\ km/s$.

umes comparable to eROSITA survey volume, and idealised or cosmological zoom-in simulations that capture the effect of baryons. It is not currently computationally feasible to run full hydrodynamic simulations in a large enough volume. One alternative has been the Baryon Pasting Project, wherein hydrodynamic cosmological simulations were used to create analytic models, which in turn "pasted" onto N-body simulations (Shaw et al., 2010; Flender et al., 2017); the analytic model for X-ray emission can also be based on observations instead, in what is called the empirical or phenomenological approach (Zandanel et al., 2018; Comparat et al., 2020). A third approach would be to train machine learning algorithms to learn the mapping between dark matter-only simulations and their hydrodynamic counterparts. Neural networks have already been used to successfully recover the dark matter halo properties from X-ray observables (Ntampaka et al., 2019; Green et al., 2019).

### 5.2.2 Measuring Turbulence in Galaxy Clusters

Paper I showed that a distinguishing feature between isolated and merging clusters is the velocity dispersion profile. Paper III highlighted that ignoring turbulence leads to erroneous interpretations of magnetic field strength in merging cluster. Currently, the best X-ray spectrometer is the Reflection Grating Spectrograph (RGS) aboard *XMM-Newton*, which cannot probe energies higher than $\sim 1.5\,keV$, the lower end of the cluster mass scale. This instrumental limit, however, is very soon due to be broken (Bulbul et al., 2019). The Japanese Space agency (JAXA) is expected to launch the X-ray Imaging and Spectroscopy Mission XRISM in 2022, which is optimised to capture one of the brightest and cleanest emission features in galaxy clusters is the Fe K line complex at $6 - 7keV$ (XRISM Science Team, 2020). The European Space Agency (ESA) is due to start constructing the Athena space telescope this year for a planned launch in 2031 (Nandra et al., 2013). Its spectrometer, *X-IFU*, should have 3 times the spectral resolution and 8 times the effective area of XRISM, creating much more detailed maps. Further down the line, NASA may approve the Lynx mission for even higher spatial resolution (The Lynx Team, 2018).

Fig 5.2 shows my synthetic images of a simulated cosmological cluster using these two instruments. These used PyXSim (Zuhone & Roediger, 2016), which convolves the intrinsic 3D properties of the simulated cluster with its redshift and the effective area and spatial and spectral resolutions of the instrument it is observed with, and the duration of the observation. This analysis assumed a highly optimistic observing time of $1\,Ms$. A more thorough study would consider simulated clusters of many different masses, undergoing various levels of merger and AGN activity, viewed from different directions, and observed for different lengths of times. This is perfectly feasible with the toolkit I have already assembled over the course of my PhD.

While we await the launch of the next generation of X-ray spectrometers, the velocity structure of the ICM can be probed in several other ways (c.f. Simionescu et al., 2019,

for a review). The XARITHMETIC algorithm of Churazov et al. (2016) analyses surface brightness fluctuations in X-ray images to infer the velocity power spectrum, which in turn has different signatures for different sources of motions. The kinetic Sunyaev-Zel'dovich effect produces a directional signature in the CMB as photons from the surface of last scattering interact with cluster electrons undergoing bulk motions, creating a Doppler-like signal (Mroczkowski et al., 2019). For each of these methods, mock images from idealised and cosmological simulations allow us to test systematics and convert observables into underlying physics.

### 5.2.3 Transport Processes in the Intracluster Medium

Paper III showed that realistic, turbulent magnetic fields do allow for the growth of instabilities along contact discontinuities in merging clusters. Furthermore, they affect the efficiency of transport processes such as viscosity and thermal conduction in the intracluster medium. Such an analysis is currently being performed for Abell 2146 by Andy Fabian's group at the University of Cambridge using the merger model I built in Paper II. The same process can be applied to similar merging systems, i.e., clusters merging close to the plane of the sky with moderate-mass ($\sim$ a few keV) enabling imaging at high spatial resolution using *Chandra* without worrying about saturation effects. Twenty-nine of these, with excellent spectroscopic and radio data, have been compiled by Golovich et al. (2017) and shown in Fig 5.3. Once the merger parameters for these systems have been inferred using the methodology in Paper II, these can also be used to measure the plasma $\beta$, viscosity, and thermal conduction (see Paper III and references therein). This would open a whole new window into understanding the evolution of the intracluster medium.

In summary, there is plenty of work ahead in the field of using simulations to maximise how much physics we can extract from multi-wavelength observations of galaxy clusters.

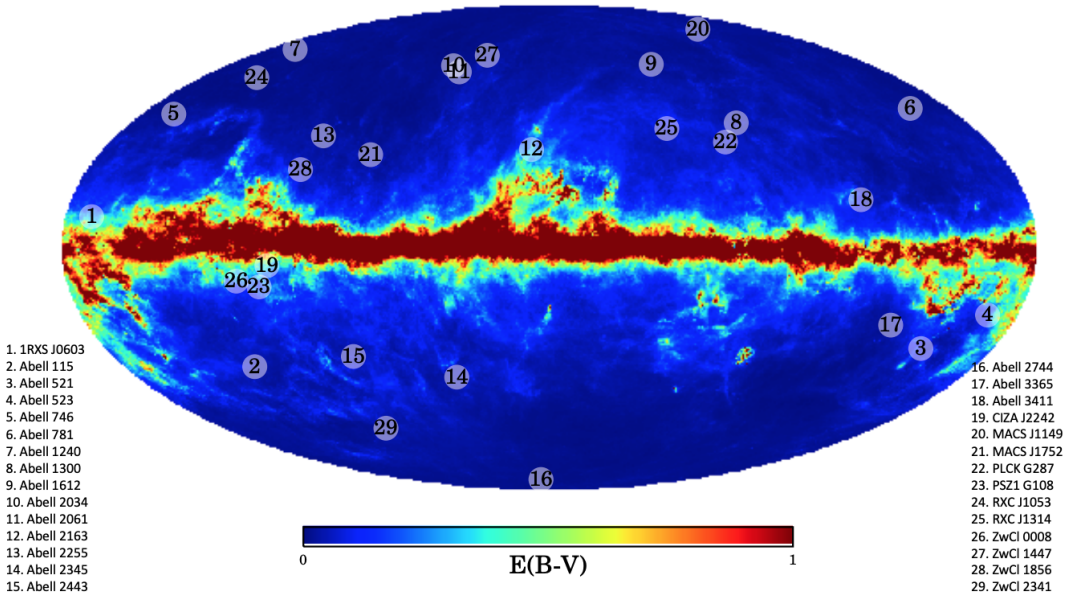


Figure 5.3: The 29 clusters catalogued in Golovich et al. (2017) are marked as points over the Galactic dust extinction map. Most of them are far from the dusty Galactic plane, allowing for clean radio observations, besides X-ray and optical spectrometry. These clusters are ripe of modeling in the style of Paper II, after which further modeling can measure the efficiency of various transport processes in them.

# Bibliography


AMI Consortium et al., 2011, , 414, 3751 19

Abell G. O., 1958, , 3, 211 8

Allen S. W., Schmidt R. W., Fabian A. C., 2002, , 334, L11 8

Allen S. W., Schmidt R. W., Ebeling H., Fabian A. C., van Speybroeck L., 2004, , 353, 457 8

Anderson M. E., Gaspari M., White S. D. M., Wang W., Dai X., 2015, , 449, 3806 16

Angelinelli M., Vazza F., Giocoli C., Ettori S., Jones T. W., Brunetti G., Brüggen M., Eckert D., 2020, , 495, 864 44

Anglés-Alcázar D., Faucher-Giguère C.-A., Quataert E., Hopkins P. F., Feldmann R., Torrey P., Wetzel A., Kereš D., 2017, , 472, L109 28

Arnaud M., Pratt G. W., Piffaretti R., Böhringer H., Croston J. H., Pointecouteau E., 2010, , 517, A92 36, 85

Asai N., Fukuda N., Matsumoto R., 2007, , 663, 816 93

Avestruz C., Nagai D., Lau E. T., Nelson K., 2015, , 808, 176 52

Babyk I. V., McNamara B. R., Nulsen P. E. J., Russell H. R., Vantyghem A. N., Hogan M. T., Pulido F. A., 2018, , 862, 39 45

Bagla J. S., 2002, Journal of Astrophysics and Astronomy, 23, 185 4

Banerjee N., Sharma P., 2014, , 443, 687 46

Barnes D. J., et al., 2017, , 471, 1088 24

Barnes D. J., et al., 2018, , 481, 1809 24, 42, 45

Battaglia N., Bond J. R., Pfrommer C., Sievers J. L., Sijacki D., 2010, The Astrophysical Journal, Volume 725, Issue 1, pp. 91-99 (2010)., 725, 91 16

Battaglia N., Bond J. R., Pfrommer C., Sievers J. L., 2012, , 758, 74 16

Beck R., Frick P., Stepanov R., Sokoloff D., 2012, , 543, A113 20

Becker M. R., Kravtsov A. V., 2011, , 740 15

Biffi V., et al., 2016, , 827, 112 16, 44

Bildfell C., Hoekstra H., Babul A., Mahdavi A., 2008, , 389, 1637 23

Bocquet S. e. a., 2015, , 799, 214 13

Böhringer H., Chon G., Kronberg P. P., 2016, , 596, A22 20, 96

Bonafede A., Feretti L., Murgia M., Govoni F., Giovannini G., Dallacasa D., Dolag K., Taylor G. B., 2010, , 513, A30 84, 96

Bond J. R., Cole S., Efstathiou G., Kaiser N., 1991, , 379, 440 2

Bondi H., 1952, Monthly Notices of the Royal Astronomical Society, 112, 195 29

Booth C. M., Schaye J., 2009, Monthly Notices of the Royal Astronomical Society, Volume 398, Issue 1, pp. 53-74., 398, 53 29

Borgani S., Kravtsov A., 2011, Advanced Science Letters, 4, 204 42

Borgani S., Diaferio A., Dolag K., Schindler S., 2008, , 134, 269 42

Bourne M. A., Sijacki D., 2017, , 472, 4707 44

Bower R. G., Schaye J., Frenk C. S., Theuns T., Schaller M., Crain R. A., McAlpine S., 2017, , 465, 32 28

Braginskii S. I., 1958, Soviet Journal of Experimental and Theoretical Physics, 6, 358 84

Branchesi M., Gioia I. M., Fanti C., Fanti R., 2007, , 472, 727 13

Brighenti F., Mathews W. G., 2006, The Astrophysical Journal, Volume 643, Issue 1, pp. 120-127., 643, 120 42

Brooks A. M., Kuhlen M., Zolotov A., Hooper D., 2013, , 765, 22 6

Brunetti G., Jones T. W., 2014, International Journal of Modern Physics D, 23, 1430007 52

Brunetti G., Cassano R., Dolag K., Setti G., 2009, , 507, 661 20

Bryan G. L., Enzo Collaboration 2014, , 211, 19 5

Brzycki B., ZuHone J., 2019, , 883, 118 20, 87

Bulbul E., et al., 2019, , 51, 210 107

Bullock J. S., Boylan-Kolchin M., 2017, , 55, 343 6

Butsky I. S., Burchett J. N., Nagai D., Tremmel M., Quinn T. R., Werk J. K., 2019, , 490, 4292 25, 45, 49

Canning R. E. A., et al., 2012, , 420, 2956 19, 61

Carilli C. L., Taylor G. B., 2002, , 40, 319 84

Cassano R., et al., 2013, , 777, 141 16

Cavagnolo K. W., Donahue M., Voit G. M., Sun M., 2008, , 683, L107 24

Cavagnolo K. W., Donahue M., Voit G. M., Sun M., 2009, , 182, 12 23

Cavagnolo K. W., McNamara B. R., Nulsen P. E. J., Carilli C. L., Jones C., Birzan L., 2010, The Astrophysical Journal, Volume 720, Issue 2, pp. 1066-1072 (2010)., 720, 1066 23

Chadayammuri U., Nagai D., Bulbul E., Ghirardini V., 2019, in AAS/High Energy Astrophysics Division. p. 107.02 xviii, 106

Chadayammuri U., ZuHone J., Nulsen P., Nagai D., Felix S., Andrade-Santos F., King L., Russell H., 2021, arXiv e-prints, p. arXiv:2108.05296 86

Christensen C. R., Governato F., Quinn T., Brooks A. M., Shen S., McCleary J., Fisher D. B., Wadsley J., 2014, , 440, 2843 27

Churazov E., Inogamov N., 2004, , 350, L52 101

Churazov E., Arevalo P., Forman W., Jones C., Schekochihin A., Vikhlinin A., Zhuravleva I., 2016, , 463, 1057 108

Clarke T. E., 2004, Journal of Korean Astronomical Society, 37, 337 20

Clerc N., et al., 2018, , 617, A92 xviii, 105

Clowe D., Bradač M., Gonzalez A. H., Markevitch M., Randall S. W., Jones C., Zaritsky D., 2006, , 648, L109 52

Coleman J. E., et al., 2017, , 464, 2469 19, 58, 61, 63

Comparat J., et al., 2020, The Open Journal of Astrophysics, 3, 13 107

Crawford C. S., Hatch N. A., Fabian A. C., Sand ers J. S., 2005, , 363, 216 24

Croton D. J., et al., 2006, , 365, 11 6

Dalla Vecchia C., Schaye J., 2012, , 426, 140 27

De Grandi S., Molendi S., 2002, , 567, 163 23, 78

Dekel A., Birnboim Y., 2006, , 368, 2 6

Dolag K., Schindler S., Govoni F., Feretti L., 2001, , 378, 777 85

Dolag K., Bartelmann M., Lesch H., 2002, , 387, 383 84

Dolag K., Vazza F., Brunetti G., Tormen G., 2005, , 364, 753 91

Domínguez-Fernández P., Vazza F., Brüggen M., Brunetti G., 2019, , 486, 623 99

Donnert J., Vazza F., Brüggen M., ZuHone J., 2018, , 214, 122 20, 99

Dubois Y., Devriendt J., Teyssier R., Slyz A., 2011, , 417, 1853 23

Dubois Y., Gavazzi R., Peirani S., Silk J., 2013, Monthly Notices of the Royal Astronomical Society, Volume 433, Issue 4, p.3297-3313, 433, 3297 30

Dubois Y., Volonteri M., Silk J., Devriendt J., Slyz A., Teyssier R., 2015, , 452, 1502 28

Duffy A. R., Schaye J., Kay S. T., Dalla Vecchia C., 2008, , 390, L64 52, 54, 64, 65

Dursi L. J., Pfrommer C., 2008, , 677, 993 85, 93, 99

Dutton A. A., Treu T., 2014, , 438, 3594 6

Eckmiller H. J., Hudson D. S., Reiprich T. H., 2011, , 535, A105 16

Eddington A. S., 1916, , 76, 572 55

Edwards L. O. V., Hudson M. J., Balogh M. L., Smith R. J., 2007, , 379, 100 23, 42

Ensslin T. A., Biermann P. L., Klein U., Kohle S., 1998, , 332, 395 72, 84

Enßlin T., Pfrommer C., Miniati F., Subramanian K., 2011, , 527, A99 49

Ettori S., Donnarumma A., Pointecouteau E., Reiprich T. H., Giodini S., Lovisari L., Schmidt R. W., 2013, , 177, 119 viii, 12

Fabian A. C., 2012, Annual Review of Astronomy and Astrophysics, vol. 50, p.455-489, 50, 455 6, 16

Fabian A. C., et al., 2011, , 418, 2154 40

Fakhouri O., Ma C.-P., Boylan-Kolchin M., 2010, , 406, 2267 52

Feretti L., Giovannini G., Govoni F., Murgia M., 2012, , 20, 54 84

Ferrari C., Govoni F., Schindler S., Bykov A. M., Rephaeli Y., 2008, , 134, 93 84

Flender S., Nagai D., McDonald M., 2017, , 837, 124 107

Fruscione A., et al., 2006, CIAO: Chandra's data analysis system. p. 62701V, doi:10.1117/12.671760 58

Fryxell B., et al., 2000, , 131, 273 5

Gaskin J. A., et al., 2019, Journal of Astronomical Telescopes, Instruments, and Systems, 5, 021001 47

Gaspari M., Sądowski A., 2017, , 837, 149 25

Gaspari M., Brighenti F., Ruszkowski M., 2012, Astronomische Nachrichten, Vol.334, Issue 4-5, p.394, 334, 394 24

Gaspari M., Ruszkowski M., Oh S. P., 2013, , 432, 3401 25, 40, 45, 46

Gaspari M., Temi P., Brighenti F., 2017, , 466, 677 45

Gitti M., McNamara B. R., Nulsen P. E. J., Wise M. W., 2007, , 660, 1118 43

Golovich N., Dawson W. A., Wittman D., Ogrean G., van Weeren R., Bonafede A., 2016, , 831, 110 52

Golovich N., van Weeren R. J., Dawson W. A., Jee M. J., Wittman D., 2017, , 838, 110 xix, 52, 108, 109

Governato F., et al., 2010, Nature, 463, 203 26

Governato F., et al., 2015, , 448, 792 26

Govoni F., Feretti L., 2004, International Journal of Modern Physics D, 13, 1549 101

Govoni F., et al., 2017, , 603, A122 101

Green S. B., Ntampaka M., Nagai D., Lovisari L., Dolag K., Eckert D., ZuHone J. A., 2019, , 884, 33 107

Grier C. J., et al., 2012, The Astrophysical Journal, Volume 764, Issue 1, article id. 47, 15 pp. (2013)., 764 24

Guo F., Mathews W. G., 2010, , 717, 937 23

Habouzit M., Volonteri M., Dubois Y., 2017, , 468, 3935 28

Hahn O., Abel T., 2011, , 415, 2101 4

Hahn O., Martizzi D., Wu H.-Y., Evrard A. E., Teyssier R., Wechsler R. H., 2017, , 470, 166 24, 42, 45

Hamer S. L., et al., 2014, , 437, 862 47

Hamer S. L., et al., 2016, , 460, 1758 47

Harvey D., Massey R., Kitching T., Taylor A., Tittley E., 2015, Science, 347, 1462 52

Hitomi Collaboration, PASJ 44, 46

Hlavacek-Larrondo J., Fabian A. C., Edge A. C., Ebeling H., Sanders J. S., Hogan M. T., Taylor G. B., 2012, , 421, 1360 24, 42

Hlavacek-Larrondo J., et al., 2018, , 475, 2743 19

Hoekstra H., 2003, , 339, 1155 15

Hoekstra H., Herbonnet R., Muzzin A., Babul A., Mahdavi A., Viola M., Cacciato M., 2015, , 449, 685 44

Hogan M. T., et al., 2017, , 851, 66 40, 45, 79

Hopkins P. F., 2015, , 450, 53 5

Iapichino L., Brüggen M., 2012, , 423, 2781 20

Jing Y. P., Suto Y., 2002, , 574, 538 15

Johnson A. R., Rudnick L., Jones T. W., Mendygral P. J., Dolag K., 2020, , 888, 101 101

Kahlhoefer F., Schmidt-Hoberg K., Frandsen M. T., Sarkar S., 2014, , 437, 2865 52

Kaiser N., 1986, , 222, 323 34

Kannan R., Springel V., Pakmor R., Marinacci F., Vogelsberger M., 2016, , 458, 410 5, 49

Katz N., White S. D. M., 1993, , 412, 455 26

Kazantzidis S., Magorrian J., Moore B., 2004, , 601, 37 55

Kim S. Y., Peter A. H. G., Wittman D., 2017, , 469, 1414 52

King L. J., et al., 2016, , 459, 517 19, 53, 56, 60, 61, 63, 64, 65

Kneib J.-P., Natarajan P., 2011, , 19, 47 13

Kormendy J., Ho L. C., 2013, Annual Review of Astronomy and Astrophysics, 51, 511–653 6

Kravtsov A. V., Klypin A. A., Khokhlov A. M., 1997, The Astrophysical Journal Supplement Series, 111, 73–94 5

Kravtsov A. V., Gnedin O. Y., Klypin A. A., 2004, , 609, 482 6

Kravtsov A. V., Vikhlinin A., Nagai D., 2006, , 650, 128 36

Kroupa P., 2001, , 322, 231 26

Kunz M. W., 2011, , 417, 602 85, 101

Kunz M. W., Schekochihin A. A., Cowley S. C., Binney J. J., Sanders J. S., 2011, , 410, 2446 5, 84, 85

Kunz M. W., Bogdanović T., Reynolds C. S., Stone J. M., 2012, , 754, 122 84, 85, 101

Lacey C., Cole S., 1993, , 262, 627 2, 52

Lage C., Farrar G. R., 2015, , 2015, 038 56

Lakhchaura K., et al., 2018, , 481, 4472 25

Latter H. N., Kunz M. W., 2012, , 423, 1964 101

Lau E. T., Kravtsov A. V., Nagai D., 2009, , 705, 1129 25, 44

Lau E. T., Gaspari M., Nagai D., Coppi P., 2017, , 849, 54 36, 44

Lewis G. F., Babul A., Katz N., Quinn T., Hernquist L., Weinberg D. H., 2000, , 536, 623 23, 42

Li Y., Bryan G. L., Ruszkowski M., Voit G. M., O'Shea B. W., Donahue M., 2015, The Astrophysical Journal, Volume 811, Issue 2, article id. 73, 15 pp. (2015)., 811 25, 40, 46

Li Y., Ruszkowski M., Bryan G. L., 2017, , 847, 106 46

Lilley E. J., Evans N. W., Sanders J. L., 2018, , 476, 2086 54, 86

Lin Y.-T., Mohr J. J., 2004, , 617, 879 72

Łokas E. L., Mamon G. A., 2001, , 321, 155 64

Lopes P. A. A., Trevisan M., Laganá T. F., Durret F., Ribeiro A. L. B., Rembold S. B., 2018, , 478, 5473 15

Lyutikov M., 2006, , 373, 73 85

Mahdavi A., Hoekstra H., Babul A., Henry J. P., 2008, , 384, 1567 44

Mahdavi A., Hoekstra H., Babul A., Bildfell C., Jeltema T., Henry J. P., 2013, , 767, 116 16, 24, 44

Mann A. W., Ebeling H., 2012, , 420, 2120 15

Mantz A. B., et al., 2015, , 446, 2205 vii, 3, 6, 15

Marinoni C., Hudson M. J., 2002, , 569, 101 6

Markevitch M., Vikhlinin A., 2007, , 443, 1 viii, 9, 52, 59, 60

Markevitch M., Gonzalez A. H., David L., Vikhlinin A., Murray S., Forman W., Jones C., Tucker W., 2002, , 567, L27 53, 61

Markevitch M., et al., 2003, , 586, L19 52

Markevitch M., Gonzalez A. H., Clowe D., Vikhlinin A., Forman W., Jones C., Murray S., Tucker W., 2004, , 606, 819 52

Massey R., et al., 2015, , 449, 3393 52

Massey R., et al., 2018, , 477, 669 52

Mazzotta P., Rasia E., Moscardini L., Tormen G., 2004, , 354, 10 69, 90

McCarthy I. G., Balogh M. L., Babul A., Poole G. B., Horner D. J., 2004, , 613, 811 23, 34

McCarthy I. G., et al., 2007, , 376, 497 46

McCarthy I. G., Babul A., Bower R. G., Balogh M. L., 2008, , 386, 1309 x, 23, 34, 35

McCourt M., Sharma P., Quataert E., Parrish I. J., 2012, , 419, 3319 24, 25, 34, 40

McDonald M., Veilleux S., Rupke D. S. N., Mushotzky R., 2010, , 721, 1262 40

McDonald M., et al., 2017, , 843, 28 23

McDonald M., Gaspari M., McNamara B. R., Tremblay G. R., 2018, , 858, 45 23

McDonald M., et al., 2019, , 885, 63 23

Mcnamara B., Nulsen P., 2007, Annual Review of Astronomy and Astrophysics, 45, 117–175 49

Medezinski E., et al.,, PASJ 13

Medvedev M. V., Silva L. O., Kamionkowski M., 2006, , 642, L1 84

Menon H., Wesolowski L., Zheng G., Jetley P., Kale L., Quinn T., Governato F., 2015, Computational Astrophysics and Cosmology, 2, 1 5, 26, 27

Miniati F., 2014, , 782, 21 46

Mitchell N. L., McCarthy I. G., Bower R. G., Theuns T., Crain R. A., 2009, , 395, 180 27

Mittal R., Hudson D. S., Reiprich T. H., Clarke T., 2009, , 501, 835 24, 42

Mo H. J., White S. D. M., 1996, , 282, 347 2

Mroczkowski T., et al., 2019, , 215, 17 108

Nagai D., 2006, , 650, 538 36

Nagai D., Lau E. T., 2011, , 731, L10 36

Nagai D., Vikhlinin A., Kravtsov A. V., 2007a, , 655, 98 16, 44

Nagai D., Kravtsov A. V., Vikhlinin A., 2007b, , 668, 1 vii, 4, 16, 36, 42, 85

Nagai D., Lau E. T., Avestruz C., Nelson K., Rudd D. H., 2013, , 777, 137 25, 36, 44

Nagai H., et al., 2019, , 883, 193 47

Nandra K., et al., 2013, arXiv e-prints, p. arXiv:1306.2307 107

Natarajan P., et al., 2017, , 468, 1962 viii, 7, 16

Navarro J. F., Frenk C. S., White S. D. M., 1996, , 462, 563 15, 64

Nelson K., Rudd D. H., Shaw L., Nagai D., 2012, , 751, 121 16

Nelson K., Lau E. T., Nagai D., 2014, , 792 ix, xii, 18, 25, 43, 44

Nelson D., et al., 2019, , p. 2010 25, 45

Neto A. F., et al., 2007, , 381, 1450 52

Ntampaka M., et al., 2019, , 876, 82 107

Nulsen P. E. J., 1982, , 198, 1007 20, 49

Oppenheimer B. D., Segers M., Schaye J., Richings A. J., Crain R. A., 2018, , 474, 4740 30

Parrish I. J., Quataert E., Sharma P., 2009, , 703, 96 49

Parrish I. J., McCourt M., Quataert E., Sharma P., 2012, , 422, 704 49

Pearce F. A., Kay S. T., Barnes D. J., Bower R. G., Schaller M., 2020, , 491, 1622 44

Penna-Lima M., Bartlett J. G., Rozo E., Melin J. B., Merten J., Evrard A. E., Postman M., Rykoff E., 2017, , 604, A89 13

Peterson B., 2006, in , Physics of Active Galactic Nuclei at all Scales. Springer Berlin Heidelberg, pp 77–100, doi:10.1007/3-540-34621-$X_3$, http://link.springer.com/10.1007/3-540-34621-X{_}3 24

Piffaretti R., Jetzer P., Schindler S., 2003, , 398, 41 12

Pillepich A., et al., 2018, , 475, 648 25

Planck Collaboration 2015, , 580, A22 26

Planck Collaboration e. a., 2020, , 641, A6 17

Planck Collaboration et al., 2016, , 594, A13 53

Planelles S., Borgani S., Fabjan D., Killedar M., Murante G., Granato G. L., Ragone-Figueroa C., Dolag K., 2014, , 438, 195 23

Pontzen A., Tremmel M., Roth N., Peiris H. V., Saintonge A., Volonteri M., Quinn T., Governato F., 2017, , 465, 547 27, 30

Poole G. B., Fardal M. A., Babul A., McCarthy I. G., Quinn T., Wadsley J., 2006, , 373, 881 24, 34, 40, 43, 46, 52, 60, 61

Poole G. B., Babul A., McCarthy I. G., Fardal M. A., Bildfell C. J., Quinn T., Mahdavi A., 2007, , 380, 437 16, 36

Poole G. B., Babul A., McCarthy I. G., Sanderson A. J. R., Fardal M. A., 2008, , 391, 1163 34, 40, 43, 46

Prasad D., Sharma P., Babul A., 2015, , 811, 108 25, 40

Prasad D., Sharma P., Babul A., 2017, , 471, 1531 25, 36, 40, 45, 46

Prasad D., Sharma P., Babul A., 2018, , 863, 62 25, 36, 40, 45, 46

Prasad D., Voit G. M., O'Shea B. W., Glines F., 2020, , 905, 50 36

Pratt G. W., et al., 2009, Astronomy and Astrophysics, Volume 511, id.A85, 14 pp., 511 23

Press W. H., Schechter P., 1974, , 187, 425 2

Pulido F. A., et al., 2018, , 853, 177 40, 45

Randall S. W., Markevitch M., Clowe D., Gonzalez A. H., Bradač M., 2008, , 679, 1173 52

Rasia E., et al., 2015, The Astrophysical Journal Letters, Volume 813, Issue 1, article id. L17, 6 pp. (2015)., 813 24, 42, 45

Rennehan D., Babul A., Hopkins P. F., Davé R., Moa B., 2019, , 483, 3810 27

Ricarte A., Tremmel M., Natarajan P., Quinn T., 2019, , 489, 802 28

Ricarte A., Tremmel M., Natarajan P., Quinn T., 2020, , 895, L8 29

Richard J., et al., 2014, , 444, 268 viii, 7

Ricker P. M., 1998, , 496, 670 72

Ricker P. M., Sarazin C. L., 2001, , 561, 621 52

Risaliti G., Nardini E., Salvati M., Elvis M., Fabbiano G., Maiolino R., Pietrini P., Torricelli-Ciamponi G., 2010, Monthly Notices of the Royal Astronomical Society, Volume 410, Issue 2, pp. 1027-1035., 410, 1027 24

Ritchie B. W., Thomas P. A., 2001, , 323, 743 26

Ritchie B. W., Thomas P. A., 2002, , 329, 675 52

Roberg-Clark G. T., Drake J. F., Reynolds C. S., Swisdak M., 2016, , 830, L9 5, 84, 85, 101

Robertson A., Massey R., Eke V., 2017, , 465, 569 52

Roediger E., Zuhone J. A., 2012, , 419, 1338 64, 65

Roediger E., Kraft R. P., Forman W. R., Nulsen P. E. J., Churazov E., 2013, , 764, 60 52, 86

Roettiger K., Burns J. O., Loken C., 1996, , 473, 651 60

Roettiger K., Loken C., Burns J. O., 1997, , 109, 307 60

Roth N., Pontzen A., Peiris H. V., 2016, , 455, 974 50

Rudd D. H., Nagai D., 2009, The Astrophysical Journal, 701 52

Russell H. R., Sanders J. S., Fabian A. C., Baum S. A., Donahue M., Edge A. C., Mcnamara B. R., Odea C. P., 2010, Monthly Notices of the Royal Astronomical Society 19, 53, 56, 69, 86

Russell H. R., et al., 2012, , 423, 236 xiv, 19, 53, 56, 58, 60, 70, 73

Russell H. R., et al., 2019, , 490, 3025 47

Ruszkowski M., Oh S. P., 2010, , 713, 1332 49, 85, 101

Ruszkowski M., Oh S. P., 2011, , 414, 1493 44

Ruszkowski M., Enßlin T. A., Brüggen M., Heinz S., Pfrommer C., 2007, , 378, 662 49

Ruzmaikin A., Sokolov D., Shukurov A., 1989, , 241, 1 84

Salomé P., et al., 2006, , 454, 437 24

Sanders J. S., Fabian A. C., Allen S. W., Morris R. G., Graham J., Johnstone R. M., 2008, , 385, 1186 40

Sanders J. S., Fabian A. C., Russell H. R., Walker S. A., 2018, , 474, 1065 23

Sanderson A. J. R., O'Sullivan E., Ponman T. J., 2009, , 395, 764 23

Santos J. S., Tozzi P., Rosati P., Böhringer H., 2010, , 521, A64 23

Sarazin C. L., 1986, Reviews of Modern Physics, 58, 1 20

Sarazin C. L., 1988, X-ray emission from clusters of galaxies 84

Sarazin C. L., 2002, in Feretti L., Gioia I. M., Giovannini G., eds, Astrophysics and Space Science Library Vol. 272, Merging Processes in Galaxy Clusters. pp 1–38 (arXiv:astro-ph/0105418), doi:10.1007/0-306-48096-4$_1$ 56

Sarazin C. L., 2004, Journal of Korean Astronomical Society, 37, 433 49

Schaye J., et al., 2015, , 446, 521 27

Schekochihin A. A., Cowley S. C., Kulsrud R. M., Rosin M. S., Heinemann T., 2008, , 100, 081301 84, 85

Schive H.-Y., ZuHone J. A., Goldbaum N. J., Turk M. J., Gaspari M., Cheng C.-Y., 2017, preprint, (arXiv:1712.07070) 5, 86

Schive H.-Y., ZuHone J. A., Goldbaum N. J., Turk M. J., Gaspari M., Cheng C.-Y., 2018, , 481, 4815 53, 54

Schmidt W., Byrohl C., Engels J. F., Behrens C., Niemeyer J. C., 2017, , 470, 142 52

Schneider A., Smith R. E., Reed D., 2013, , 433, 1573 2

Sharma P., Chandran B. D. G., Quataert E., Parrish I. J., 2009, , 699, 348 49

Sharma P., McCourt M., Quataert E., Parrish I. J., 2012, , 420, 3174 25, 40, 45

Sharma R., Brooks A., Somerville R. S., Tremmel M., Bellovary J., Wright A., Quinn T., 2019, arXiv e-prints, p. arXiv:1912.06646 29

Shaw L. D., Nagai D., Bhattacharya S., Lau E. T., 2010, , 725, 1452 107

Shen S., Wadsley J., Stinson G., 2010, , 407, 1581 27

Shen S., Madau P., Aguirre A., Guedes J., Mayer L., Wadsley J., 2012, , 760, 50 27

Shi X., Komatsu E., Nelson K., Nagai D., 2015, , 448, 1020 44

Shi X., Komatsu E., Nagai D., Lau E. T., 2016, , 455, 2936 44

Sijacki D., Springel V., 2005, Monthly Notices of the Royal Astronomical Society, Volume 366, Issue 2, pp. 397-416., 366, 397 28, 30

Sijacki D., Springel V., Di Matteo T., Hernquist L., 2007, Monthly Notices of the Royal Astronomical Society, Volume 380, Issue 3, pp. 877-900., 380, 877 23, 42

Sijacki D., Vogelsberger M., Genel S., Springel V., Torrey P., Snyder G. F., Nelson D., Hernquist L., 2015, , 452, 575 30

Silk J., Mamon G. A., 2012, Research in Astronomy and Astrophysics, 12, 917 vii, 6

Simionescu A., et al., 2019, , 215, 24 viii, 17, 107

Smith M. C., Sijacki D., Shen S., 2018, , 478, 302 30, 45

Sokołowska A., Mayer L., Babul A., Madau P., Shen S., 2016, , 819, 21 27

Sokołowska A., Babul A., Mayer L., Shen S., Madau P., 2018, , 867, 73 27

Spitzer Lyman J., 1952, , 116, 299 20, 84

Springel V., 2010, , 401, 791 5

Springel V., Farrar G. R., 2007, , 380, 911 56

Springel V., Di Matteo T., Hernquist L., 2005, , 620, L79 5

Stasyszyn F. A., de los Rios M., 2019, , 487, 4768 20, 99

Steinborn L. K., Dolag K., Hirschmann M., Prieto M. A., Remus R.-S., 2014, Monthly Notices of the Royal Astronomical Society, Volume 448, Issue 2, p.1504-1525, 448, 1504 24, 28

Stevens A. R. H., Lagos C. d. P., Contreras S., Croton D. J., Padilla N. D., Schaller M., Schaye J., Theuns T., 2017, , 467, 2066 28

Stinson G., Seth A., Katz N., Wadsley J., Governato F., Quinn T., 2006, , 373, 1074 26, 30

Subramanian K., Shukurov A., Haugen N. E. L., 2006, , 366, 1437 20, 84, 99

Sun M., 2009, The Astrophysical Journal, Volume 704, Issue 2, pp. 1586-1604 (2009)., 704, 1586 16, 23, 42

Takizawa M., 2005, , 629, 791 60

Takizawa M., 2008, , 687, 951 93

Teyssier R., 2002, Astronomy and Astrophysics, 385, 337–364 5

The Lynx Team 2018, arXiv e-prints, p. arXiv:1809.09642 107

Tremblay G. R., et al., 2016, Nature, Volume 534, Issue 7606, pp. 218-221 (2016)., 534, 218 24, 40

Tremmel M., Karcher M., Governato F., Volonteri M., Quinn T. R., Pontzen A., Anderson L., Bellovary J., 2017, , 470, 1121 26, 27, 29, 30, 48

Tremmel M., et al., 2019, , 483, 3336 xii, 25, 26, 27, 30, 31, 34, 36, 39, 42, 45, 48, 49

Treu T., Koopmans L. V. E., 2004, , 611, 739 6

Tulin S., Yu H.-B., 2018, , 730, 1 52

Vale A., Ostriker J. P., 2006, , 371, 1173 6

Vazza F., 2011, , 410, 461 42

Vazza F., Brunetti G., Kritsuk A., Wagner R., Gheller C., Norman M., 2009, , 504, 33 91

Vazza F., Brunetti G., Gheller C., Brunino R., Brüggen M., 2011, , 529, A17 25, 91

Vazza F., Brüggen M., Gheller C., 2013, , 428, 2366 42

Vazza F., Brüggen M., Gheller C., Wang P., 2014, , 445, 3706 20, 84

Vikhlinin A., Markevitch M., Murray S. S., 2001, , 549, L47 85, 99

Vikhlinin A., Markevitch M., Murray S. S., Jones C., Forman W., Van Speybroeck L., 2005, , 628, 655 58, 79

Vikhlinin A., Kravtsov A., Forman W., Jones C., Markevitch M., Murray S. S., Van Speybroeck L., 2006, , 640, 691 54, 55, 78, 87

Vikhlinin A., et al., 2009a, , 692, 1033 6

Vikhlinin A., et al., 2009b, , 692, 1060 vii, 3, 6

Voit G. M., 2018, , 868, 102 34, 36

Voit G. M., Donahue M., 2005, , 634, 955 23

Voit G. M., Donahue M., 2014, The Astrophysical Journal Letters, Volume 799, Issue 1, article id. L1, 5 pp. (2015)., 799 23

Voit G. M., Bryan G. L., Balogh M. L., Bower R. G., 2002, , 576, 601 23

Voit G. M., Bryan G. L., O'Shea B. W., Donahue M., 2015, , 808, L30 24, 25, 40, 45

Voit G. M., Meece G., Li Y., O'Shea B. W., Bryan G. L., Donahue M., 2017, , 845, 80 25

Voit G. M., Ma C. P., Greene J., Goulding A., Pandya V., Donahue M., Sun M., 2018, , 853, 78 45

Wadsley J. W., Stadel J., Quinn T., 2004, New Astrophysics, 9, 137 5

Wadsley J. W., Veeravalli G., Couchman H. M. P., 2008, , 387, 427 27

Wadsley J. W., Keller B. W., Quinn T. R., 2017, , 471, 2357 26, 27

Walker S. A., Sanders J. S., Fabian A. C., 2016, , 461, 684 94

Wang Q. H. S., Markevitch M., Giacintucci S., 2016, , 833, 99 96

Wang Q. H. S., Giacintucci S., Markevitch M., 2018, , 856, 162 52

Weinberger Rainer e. a., 2016, Monthly Notices of the Royal Astronomical Society, 465, 3291 28

Weinberger R., et al., 2017, , 465, 3291 30, 42, 48

Werner N., et al., 2016, , 455, 846 94

Wetzel A. R., Hopkins P. F., Kim J.-h., Faucher-Giguère C.-A., Kereš D., Quataert E., 2016, , 827, L23 6

White J. A., et al., 2015, , 453, 2718 19, 53, 56, 60, 61, 72

Wittman D., Cornell B. H., Nguyen J., 2018, , 862, 160 52

Wittor D., Jones T., Vazza F., Brüggen M., 2017, , 471, 3212 46

XRISM Science Team 2020, arXiv e-prints, p. arXiv:2003.04962 107

Yang H.-Y. K., Reynolds C. S., 2016, The Astrophysical Journal, 818, 181 49

Zandanel F., Fornasa M., Prada F., Reiprich T. H., Pacaud F., Klypin A., 2018, , 480, 987 107

Zhang Y.-Y., et al., 2010, , 711, 1033 13

Zhang C., Churazov E., Forman W. R., Jones C., 2019, , 482, 20 53, 59

Zhang C., Churazov E., Dolag K., Forman W. R., Zhuravleva I., 2020, , 494, 4539 53

Zhuravleva I., Churazov E., Kravtsov A., Lau E. T., Nagai D., Sunyaev R., 2013, , 428, 3274 36

Zinger E., Dekel A., Birnboim Y., Kravtsov A., Nagai D., 2016, , 461, 412 25, 36

Zitrin A., Bartelmann M., Umetsu K., Oguri M., Broadhurst T., 2012, , 426, 2944 72

ZuHone J. A., 2011, , 728, 54 52

ZuHone J. A., Markevitch M., Johnson R. E., 2010, , 717, 908 43, 46

ZuHone J. A., Markevitch M., Ruszkowski M., Lee D., 2013, , 762, 69 5, 49, 52, 101

ZuHone J. A., Kunz M. W., Markevitch M., Stone J. M., Biffi V., 2015a, , 798, 90 52, 101

ZuHone J. A., Brunetti G., Giacintucci S., Markevitch M., 2015b, , 801, 146 98

ZuHone J. A., Kowalik K., Öhman E., Lau E., Nagai D., 2018, , 234, 4 67

Zuhone J. A., Roediger E., 2016, Journal of Plasma Physics, 82, 535820301 52, 107

Zuhone J. A., Markevitch M., Lee D., 2011, The Astrophysical Journal, 743, 16 43, 46, 69, 85, 93, 98

van de Voort F., Schaye J., Booth C. M., Haas M. R., Dalla Vecchia C., 2011a, , 414, 2458 27, 48

van de Voort F., Schaye J., Booth C. M., Dalla Vecchia C., 2011b, , 415, 2782 48